Effect of environment on the fidelity of control and measurements of solid-state quantum devices

by

Amrit Poudel

A dissertation submitted in partial fulfillment of

the requirements for the degree of

Doctor of Philosophy

(Physics)

at the

University of Wisconsin – Madison

2013

Defended on 22 July, 2013

Dissertation approved by the following members of the Final Oral Committee:

Maxim G. Vavilov · Associate Professor of Physics

Robert J. Joynt · Professor of Physics

Robert F. McDermott · Associate Professor of Physics

Mark A. Friesen · Senior Scientist of Physics

Mark Rzchowski · Professor of Physics

Abstract

This thesis addresses the origin and effect of noise and fluctuations in quantum devices that find applications in quantum information processing. In the first half of the thesis, we consider a phenomenological model of the noise and study its effect on the fidelity of quantum measurements and operations that are essential for quantum computing. We focus primarily on quantum gate operations in phase qubits, detection of microwave photons and the measurement of the Berry curvature. Specifically, we examine the effect of the Ohmic noise on optimally controlled flux-biased phase qubits for one- and two-quadrature microwave pulses and demonstrate that two-quadrature pulses with fixed driving frequency are as robust as variable driving frequency, in the presence of environment. Next, we present a model to analyze the quantum efficiency of a microwave photon detector based on a current-biased Josephson junction and study the effect of decoherence on the detection efficiency of the detector. We also present alternative set-ups for microwave photon detection and provide a systematic method to compute the power absorbed by the detector. We then consider the effect of decoherence on the Berry curvature measurement, which employs a novel non-adiabatic protocol, and show that the curvature is immune to decoherence.

In the second half of the thesis, we go beyond the phenomenological models of the noises and perform a detailed study of the microscopic description of the Johnson noise. Here we focus primarily on quantum dot devices. We present a formalism to compute relaxation rates in charge and spin qubits due to evanescent wave Johnson noise (EWJN) from the metallic gates that are in proximity to quantum dots. The EWJN is analyzed for the metallic gates that are characterized by both local and nonlocal dielectric response functions. Additionally, we extend our treatment beyond the dipole approximation by taking into account the finite size of the quantum dots. We also derive an enhancement of the electric EWJN that occurs outside a thin metallic film, relative to the electric field surrounding a conducting half-space.

Acknowledgements

This work would not have been possible without the help and support of countless individuals, both during and before my time at UW-Madison. First and foremost, I would like to express my sincere gratitude for the support and guidance of my advisor, Prof. Maxim G. Vavilov. I am very grateful for the time and effort he has put into helping me understand the area of research reported in this thesis and also for the financial support that he arranged for me to carry out this work. Maxim has spent many hours patiently explaining the intricacies of research problems in physics, carefully scrutinizing my work and making me think more critically. I am especially grateful to him for being always available to answer my questions and for providing lightening fast feedbacks to my numerous queries. I would not have completed my work in a timely manner if it were not for his swift responses to my questions and proper guidance during the critical phase of my graduate studies. I am equally indebted to Prof. Robert Joynt for letting me join his research group to work on a project, which forms a significant component of this thesis. I hope that I will continue to collaborate frequently with both of them in the future.

I offer my sincere thanks to Prof. Robert McDermott, who generously offered me to work in his laboratory much of my first year in the graduate school. This was a tremendous learning experience for me which helped me realize what my strengths were and what I should be focusing on going forward.

I also extend my thanks to my other collaborators for their efforts and assistance. I greatly appreciate collaborations with Dr. Luke Langsjoen, and Canran Xu. I have truly enjoyed our countless discussions about physics problems in general with Dushko Kuzmanoviski.

I would also like to express my appreciation to my thesis committee, Prof. Maxim Vavilov, Prof. Robert Joynt, Prof. Robert McDermott, Dr. Mark Friesen, and Prof. Mark Rzchowski, for their time and consideration.

I have had the great fortune of benefiting from the wisdom, encouragement, and friendship of many mentors. One person who has significantly helped me on the path towards

this dissertation is my undergraduate advisor, Prof. Leonidas Pantelidis, who has been my instructor, mentor and personal friend. I am grateful, as always, for his unwavering confidence in me and, especially, for his extraordinary personal support ever since I have known him. I would not have made it this far if it were not for Leo's constant guidance and support from the onset of my journey into the world of physics.

Finally, I would also like to thank my parents, who have always steered me right, and my friends, who showed interest in my research just to cheer me up. My parents and my sister have been my emotional anchors through not only the highs and lows of graduate school, but my entire life.

The work presented in this dissertation was supported by the NSF Grant No. DMR 0955500, as well as by the Army Research Office (ARO) and Laboratory of Physical Sciences (LPS) Grant No. W911NF-11-1-0030.

I dedicate this thesis to my parents and my sister who have always been a constant source of support and encouragement throughout my life.

Contents

Abstract i

Acknowledgements ii

Contents **v**

List of Figures **viii**

1 Introduction **1**

1.1 Thesis outline 5

1.2 Publications 7

2 Qubit devices and decoherence **9**

2.1 Introduction 9

2.2 Decoherence in superconducting qubits 9

2.3 Decoherence in semiconducting qubits 10

2.4 Modeling the dynamics of open quantum systems 12

Lindblad master equation 12

Caldeira-Leggett master equation 17

2.5 Discussion 20

3 Effect of the Ohmic environment on optimally controlled flux-biased phase qubit **22**

3.1 Introduction 22

3.2 Model 24

3.3 Gate error and DRAG method 26
3.4 Results 29
3.5 Discussion 35

4 Microwave photon detector based on a current-biased Josephson junction 37
4.1 Introduction 37
4.2 Josephson-junction based photon detector 39
4.3 Quantum efficiency 40
4.4 Result 41
4.5 Input-output theory and reflection coefficient 46
4.6 Power absorbed by the detector 48
Formalism 48
Waiting time distribution 51
4.7 Discussion 55

5 Effect of decoherence on the Berry curvature 56
5.1 Introduction 56
5.2 Berry phase and curvature 57
5.3 Berry curvature in a two-level system 58
Results 59
5.4 Berry curvature in superconducting qubits 66
Results 68
5.5 Discussion 69

6 Qubit relaxation from evanescent-wave Johnson noise: Dipole approximation 70
6.1 Introduction 70
6.2 Formalism 73
6.3 Results 77
6.4 Discussion 82

7 Qubit relaxation due to evanescent-wave Johnson noise: Beyond dipole approximation **84**

7.1 Introduction 84

7.2 Charge qubit 86

7.3 Spin qubit 93

7.4 Thin metallic gates 96

7.5 Discussion 98

8 Conclusions **100**

Appendix A Supplemental information for chapter 3 **102**

A.1 Hamiltonian of a flux-biased phase qubit 102

A.2 Numerical solution of the Schrodinger's equation 104

Appendix B Supplemental information for chapter 6 **105**

B.1 Derivation of Green's tensor for half space 105

Appendix C Supplemental information for chapter 7 **109**

C.1 Derivation of generalized Fermi's golden rule 109

C.2 Derivation of Green's tensor for a thin film 111

Bibliography **113**

List of Figures

3.1 Schematic of a flux-biased phase qubit and RCSJ model 25
3.2 Gate error *vs.* gate time for single and double quadrature pulses 29
3.3 (a) Gate error *vs.* parameter α, and (b) Probability *vs.* time 31
3.4 Gate error *vs.* gate time for variable frequency drive 32
3.5 Gate error *vs.* gate time for fixed frequency drive 33
3.6 Normalized gate error *vs.* temperature 34

4.1 Schematic circuit diagram of a JJ-based detector and potential energy landscape 38
4.2 Switching probability *vs.* photon detection time 41
4.3 Quantum efficiency η_1 *vs.* detuning Δ/Ω 43
4.4 Quantum efficiency η_1 *vs.* photon detection time 44
4.5 Efficiency η_n to detect a photon *vs.* detection time 45
4.6 Schematic circuit diagrams of JJ-based detectors 49
4.7 Waiting time distribution of a microwave driven JJ without dissipation 51
4.8 Waiting time distribution of a microwave driven JJ with dissipation 52
4.9 Waiting time distribution of a microwave driven resonator and JJ 53
4.10 Average switching rates for two detection schemes 54

5.1 Magnetization σ_z *vs.* the ramp velocity without decoherence 61
5.2 Magnetization σ_y *vs.* drive time in the presence of decoherence 63
5.3 Magnetization σ_y *vs.* the angular velocity in the presence of decoherence 64
5.4 Magnetization σ_y *vs.* the ramp velocity in the presence of decoherence 66

5.5 Berry curvature in the presence of the third level 68

6.1 Schematic of the cross-section of a device 72
6.2 Illustration of evanescent waves outside the metal 73
6.3 T_1 time of a charge qubit *vs.* distance z from the metallic gate 78
6.4 T_1 time *vs.* charge qubit frequency ω 79
6.5 T_1 time of a spin qubit *vs.* distance z from the metallic gate 80
6.6 T_1 time *vs.* spin qubit frequency ω 81

7.1 Schematic of the cross-section and a picture of an actual device 85
7.2 Energy relaxation time in a charge qubit in 1D 90
7.3 Ratio of relaxation times as a function of a bias parameter 91
7.4 Energy relaxation time in a charge qubit in 2D 92
7.5 Spin-flip time in a single quantum dot 94
7.6 Ratio of relaxation times as a function of film thickness 97

Chapter 1

Introduction

Physicists have long envisioned the idea of harnessing the power of quantum mechanics to perform computational tasks [1, 2]. However, the actual work toward practical implementation of such a ground-breaking idea has only begun recently. The concept of quantum computation has gained considerable momentum in recent years due to a discovery that certain computational tasks, such as number factorization, period finding [3], and database search [4], could be speeded up if these problems were encoded in the states of quantum systems called quantum bits (or qubits) and computed employing operations described by quantum mechanics [5]. Due to its quantum nature, a quantum bit can be in a superposition of both its logical states "0" and "1". Hence, while a classical memory consisting of n bits allows to store one out of 2^n numbers, n quantum bits can store all 2^n numbers simultaneously. Logical operations on a quantum memory work in parallel to all these numbers, whereas a classical computer would need to repeat the calculation 2^n times. This "built-in" parallelism facilitates a quantum computer to work exponentially faster allowing to solve computationally intensive problems in seconds which would otherwise take years on today's fastest supercomputers. Furthermore, in a quantum processor, qubit states can be superposed and entangled by sequences of externally controlled manipulations that result in unitary transformations, also known as quantum gates. Such quantum operations allow quantum computers to push boundaries of parallel computations, unconditionally secure

communications, etc.

Numerous systems have now been proposed as promising candidates for quantum information processing. Among these are trapped ions [6, 7], optical lattices [8, 9], photons [10], nuclear spins of molecules (nuclear magnetic resonance, Nitrogen-vacancy centers in diamond, etc.) [11, 12], quantum dots [13] and superconducting circuits [14]. While there exists different platforms on which to build the hardware of a quantum computer, semiconducting and superconducting qubits based on solid-state technologies are the most promising candidates that hold unique prospects of scalability and manageability owing to their ease of integration with highly developed semiconductor technology and classical electronics.

For practical realization of a quantum computer, advances must be made to preserve the quantum coherence much longer than gate operation times. The loss of the quantum coherence of a qubit stems from the interaction of the qubit with its local environment. This phenomenon is often known as decoherence in the literatures. In the past decade, tremendous progress has been made in identifying various sources of decoherence that plague practical implementation of solid-state qubits [15]. In a semiconducting qubit, some sources of decoherence are intrinsic in nature, such as charge coupling to phonons, while others are extrinsic, such as Johnson noise due to fluctuating electromagnetic fields arising from the metallic gates or transmission lines used to control the qubit. Similarly, in superconducting qubits, the most notorious of all sources of decoherence is the presence of defects in dielectric materials [16] used to construct Josephson junctions, which are building blocks of superconducting qubits. Indeed, decoherence has been a constant worry since the beginning of the field of quantum computing, which has led to emergence of new ideas like decoherence free subspace [17], topological quantum computing [18, 19], error-correction codes [20], dynamical decoupling [21], which have all galvanized the quest for harnessing the power of quantum mechanics to perform complex computational tasks.

Since it is not practically possible to completely isolate a qubit from its environment, controlling the qubit in the presence of environment is another equally important aspect of quantum computation. Furthermore, qubits are often approximated by a two-level sys-

tem, which is not necessarily accurate particularly in case of solid-state qubits based on macroscopic degrees of freedom like charge or current as in charge or phase qubit in superconducting qubits. This poses another hindrance to accurate control of qubits during gate operations. Inaccurate control often leads to additional error, which can surpass the threshold of a fault-tolerant quantum computation [22, 23], rendering the output from quantum operations unreliable. One way to overcome this problem is by engineering shaped pulses that are optimized for particular gate operations and are easy to implement in the laboratory. Therefore, it is vitally important to perform a detailed study of the performance of the optimally shaped pulses in the presence of environment that qubits are most likely to encounter.

While decoherence is the most pressing issue and deserves undivided attention of the scientific community, researchers have also managed to explore several other avenues within mesoscopic physics which will ultimately benefit the field of quantum computing. One of such avenues is circuit quantum electrodynamics (cQED), which also finds applications in quantum information processing. Indeed, with the generation of non-classical propagating fields [24, 25], and the demonstrated potential for microwave radiation to mediate coupling between solid-state qubits [26], the field of cQED has become a rapidly evolving test-bed for mesoscopic physics and a promising paradigm for quantum computation. However, the lack of a microwave photon detector is one major deficiency within this field. High efficiency microwave photon detection is an interesting problem for many areas of physics, including low temperature measurement, quantum information science, particle physics and astrophysics. For optical photons, there are many examples of devices capable of detecting single photons with high efficiency [27]. However, reliable single photon detection of microwaves is very difficult, principally due to their low energy. It is therefore imperative to explore different models of on-chip microwave photon detector and analyze their efficiency in the presence of coupling to the environment.

Aware of the difficulty in overcoming decoherence in a practical quantum computer architecture, researchers have also started exploring alternative proposals for qubit imple-

mentation that are fundamentally different from the previous proposals. In these proposals, information is encoded in those degrees of freedom that are insensitive to local perturbations and hence are protected against errors caused by interaction with the local environment. This novel computing paradigm, known as topological quantum computing, has gained considerable attention in recent years due to its intrinsic fault-tolerant nature. It has been shown that universal quantum computation can be performed using only geometric effects appearing in quantum phases [28]. The Berry phase is one of such geometric phases that can be used to implement elementary quantum gates. Although geometric evolutions are easy to control and resistant to error, it is not quite straightforward to measure the Berry phase in practice. Traditional experiments for the Berry phase measurement require strict adiabatic conditions and rely on interference effects [29]. The measurement process would be greatly simplified if such stringent conditions could be avoided altogether. A more recent proposal [30] that does not require strict adiabatic condition is a promising step in that direction. Although non-adiabatic measurement protocols are very attractive, they may not be immune to noises from the environment. It is, therefore, important to understand how the coupling of a qubit to its environment affects the Berry curvature, and in turn the Berry phase, in non-adiabatic measurement protocols.

To that end, this thesis consists of two major parts. The first part, comprising of the first four chapters, discusses issues related to superconducting qubits. In particular, we examine the optimally controlled phase qubit in the presence of the Ohmic environment and propose alternative pulse sequences that are robust against the presence of the third level in the qubit and easier to implement in the laboratory. We also analyze the efficiency of a microwave photon detector based on a current-biased Josephson junction. Next, we consider the effect of environment on the Berry curvature and discuss the prospects of measurement of the Berry curvature in superconducting qubits. The second part, consisting of the next two chapters, discusses issues related to semiconducting qubits. Here we perform a detailed study of the physics of Johnson noise and provide formula for relaxation rates in charge and spin qubits for various cases. The majority of the work done in this part has an emphasis on

quantum dot devices, but it applies to other qubit architectures that incorporate metallic gates, traps or electrodes in the vicinity of the qubit.

1.1 Thesis outline

This thesis describes several aspects of the theoretical issues related to semiconducting and superconducting qubits. A common thread that ties together different chapters in this thesis is the study of the effect of decoherence on measurements and operations in quantum devices that find applications in quantum information processing.

In chapter 2, we provide a brief overview of different noise sources that are responsible for dissipation and dephasing in superconducting and semiconducting qubits. Some of these noise sources are due to external circuitry that is used to control and manipulate qubits, while the other sources are intrinsic to qubit devices. We then proceed to discuss different methods that can be used to study the coupling of a qubit to its environment. Here we derive the master equation of an open quantum system using a phenomenological model of the environment.

In chapter 3, we study the effect of environment on the gate operation of flux-biased phase qubits. We employ the master equation for a reduced density matrix of the qubit system coupled to the Ohmic environment, described by the Caldeira-Leggett model. Numerically solving this equation, we evaluate the gate error as a function of gate time, temperature, and environmental coupling strength for experimentally determined qubit parameters. The analysis is presented for single-quadrature microwave (control) pulses as well as for two-quadrature pulses, which lower the gate error significantly for idealized systems in the absence of environment. Our results indicate that two-quadrature pulses with fixed and variable driving frequency have similar performance, which outweighs the performance of single-quadrature pulses, in the presence of environment.

In chapter 4, we analyze the quantum efficiency of a microwave photon detector based on a current-biased Josephson junction. We consider the Jaynes-Cummings Hamiltonian to describe coupling between the photon field and the junction. We then take into ac-

count the coupling of the junction and the resonator to the environment. We solve the equation of motion of the density matrix of the resonator-junction system to compute the quantum efficiency of the detector as a function of detection time, bias current, and energy relaxation time. Our results indicate that junctions with modest coherence properties can provide efficient detection of single microwave photons, with quantum efficiency in excess of 80%. Furthermore, we discuss other alternative set-ups for microwave photon detection and provide a systematic way of calculating the power absorbed by the detector in those set-ups.

Next, we discuss the effect of decoherence on geometric phases in quantum mechanics. In chapter 5, we perform a detailed analysis of the effect of relaxation and pure dephasing on the Berry curvature, which is computed by employing a novel non-adiabatic protocol. We then provide an experimentally convenient method to measure the Berry curvature. Our results indicate that the Berry curvature is immune to decoherence in non-adiabatic measurement protocols. In addition, we also consider the effect of the third level on the measurement of the Berry curvature in superconducting qubits.

In the remaining chapters, we turn our attention to microscopic models of decoherence in qubits, focusing primarily on semiconducting qubit architectures. In chapter 6, we focus on the origin and effect of evanescent-wave Johnson noise in semiconducting qubits. In many quantum computer architectures, the qubits are in close proximity to metallic device elements. Metals have a high density of photon modes, and the fields spill out of the bulk metal because of the evanescent-wave component. Thus thermal and quantum electromagnetic Johnson-type noise from metallic device elements can decohere nearby qubits. Here we use quantum electrodynamics to compute the strength of this evanescent-wave Johnson noise as a function of distance from a metallic half space. Previous treatments have shown unphysical divergences on the surface of metallic gate. We remedy this by using a proper nonlocal dielectric function. Decoherence rates of local qubits are proportional to the magnitude of electric or magnetic correlation functions evaluated at the qubit position. These rates serve as an important constraint on future device architectures. Compari-

son with single-electron spin relaxation measurements shows that evanescent-wave Johnson noise may constitute the dominant relaxation mechanism in experiments performed at low magnetic field.

In chapter 7, we continue our study of decoherence in charge (spin) qubits due to evanescent-wave Johnson noise (EWJN) in a laterally coupled double quantum dot (single quantum dot). We derive expressions for the energy relaxation rates of charge and spin qubits in a variety of dot geometries, and EWJN is shown to be a dominant source of decoherence for spin qubits held at low magnetic fields. Previous studies in this field approximated the charge or spin qubit as a point dipole. Ignoring the finite size of the quantum dot in this way leads to a spurious divergence in the relaxation rate as the qubit approaches the metal. Our approach goes beyond the dipole approximation and remedies this unphysical divergence by taking into account the finite size of the quantum dot. Additionally, we derive an enhancement of EWJN that occurs outside a thin metallic film, relative to the field surrounding a conducting half-space.

Finally, in chapter 8 we offer concluding remarks.

1.2 Publications

Some of the main chapters in this thesis are based on published results, each of which represents the work of many individuals. Here, I document my contribution to each work, as well as my collaborators.

Chapter 3 is based on Ref. [31], titled *Effect of the Ohmic environment on an optimally controlled flux-biased phase qubit*, which I completed with Prof. Maxim G. Vavilov. I carried out the analytical and numerical calculations, under the supervision of Prof. Vavilov.

Chapter 4 is based on Ref. [32], titled *Quantum efficiency of a microwave photon detector based on a current-biased Josephson junction*, which I completed with Prof. Robert McDermott, and Prof. Maxim G. Vavilov. I carried out the main numerical calculation based on a theoretical model suggested by Prof. Vavilov, which was based on an experimental device first proposed and developed by Prof. McDermott.

Chapter 6 is based on Ref. [33], titled *Qubit relaxation from evanescent-wave Johnson noise*, which I completed with Dr. Luke Langsjoen, Prof. Maxim G. Vavilov, and Prof. Robert Joynt. I principally carried out the numerical work with assistance from Dr. Langsjoen, based on theoretical work laid out by Prof. Vavilov, and Prof. Joynt.

Chapter 7 is based on Ref. [34], titled *Relaxation in quantum dots due to evanescent-wave Johnson noise*, which I completed with Dr. Luke Langsjoen, Prof. Maxim G. Vavilov, and Prof. Robert Joynt. I carried out the analytical and numerical work with assistance from Dr. Langsjoen, Prof. Vavilov, and Prof. Joynt.

Chapter 2

Qubit devices and decoherence

2.1 Introduction

Most proposals for implementing a quantum computer are based on qubits constructed from microscopic degrees of freedom. They consider spin of either electrons or nuclei, or transition dipoles of either atoms or ions in vacuum. These degrees of freedom are naturally very well isolated from their environment, and hence decohere slowly. However, in other solid-state qubit architectures like integrated superconducting circuits or semiconducting heterostructures, quantum coherence inevitably suffers from fluctuations due to their environment. In this chapter, we first briefly discuss different sources of noises that plague semiconducting and superconducting qubit architectures. We then discuss theoretical methods or models that are used in this thesis to study coupling of the qubit devices to environment, within the framework of open quantum systems.

2.2 Decoherence in superconducting qubits

Superconducting qubits are solid-state electrical circuits based on the Josephson junction (JJ), which is non-dissipative and strongly non-linear circuit element [35]. In contrast to microscopic entities such as spins or atoms, they tend to be well coupled to other circuits, which make them very attractive candidates for readouts and gate implementations. How-

ever, the same biasing wires that make superconducting circuits easy to manipulate and measure also couple the qubit to the electromagnetic environment which is responsible for dissipation and dephasing of the qubit. Any external circuit that is connected to the JJ provides complex impedance $Z(\omega)$ to the Josephson junction. This external impedance is defined as the ratio of the complex amplitudes of the voltage response of the environment to the the oscillating current at frequency ω. The real part of this complex impedance characterizes the dissipative contribution of the external electromagnetic environment. In this and subsequent chapters, we primarily focus on the noise due to external circuits.

In addition to the noise due to external circuits, various other mechanisms are responsible for noises in superconducting qubits. Most of these mechanisms are intrinsic in nature. For instance, the motion of charges in the defects in the oxide tunnel barrier and amorphous dielectric of the circuit have been proposed to be the source of critical current noise [36, 37] and charge noise [38, 39], respectively. The $1/f$ spectrum (where f is the frequency) of the materials noises suggests that they all originate from two-level fluctuators in the amorphous tunnel layer of the junction [40]. Similarly, the relaxation of paramagnetic spins located at the superconductor-insulator interfaces can be the source of low frequency $1/f$ flux noise [41, 42], although the exact mechanism responsible for the origin of such spins is not quite clear and is an area of active research.

2.3 Decoherence in semiconducting qubits

The building block of a semiconducting qubit is a quantum dot, which can be thought of as a quantum box that can be filled with electrons (or holes) which occupy the available discretized states of the system. The electrons can tunnel on and off the dot, which is coupled to a large reservoir via tunnel barriers. The gate electrodes are used to control the height of the barriers and consequently the rates for tunneling through the barriers on and off the dots [43]. Although many kinds of quantum dots have been realized so far, in this thesis we focus exclusively on GaAs or Si based quantum dots.

An important class of proposals consists of using the charge degree of freedom in semi-

conducting double quantum dots to realize a charge qubit [44, 45]. A significant advantage of the charge qubit is that it can be controlled directly via external voltage sources. While charge qubits are easy to control and manipulate, they also couple easily to the outside environment. It is widely believed that the main contribution to decoherence in a charge qubit comes from its coupling to fluctuating background charges (FBC) that create dynamical electric field, which affects the charge qubit state [46, 47, 48]. The sources of FBCs are electrons trapped in the insulating layer close to the surface of metallic gates/electrodes. These electrons can also interact with the conduction electrons in the gates leading to significant decoherence of charge qubits [49]. Other probable alternative microscopic mechanisms of decoherence in charge qubits are via electron coupling to the phonon bath [50] and due to gate voltage fluctuations [51].

Other proposals utilize the electron spin in semiconductor quantum dots, which can be isolated and controlled with a high accuracy, to realize a spin qubit [52, 53]. However, like a charge qubit, spin qubit also suffers from decoherence due to its coupling with the surrounding environment. Two kinds of environment have been identified as the main source of decoherence of an electron spin in a quantum dot. They are the phonons in the lattice [54, 55] and the spins of atomic nuclei in the quantum dot [56]. In GaAs based quantum dots, strong spin-orbit interaction is present even in the absence of external electric fields. This interaction couples spin with the orbital degrees of freedom, which is then coupled to phonons. Consequently, it leads to indirect coupling between the electron spin and phonons [57]. The phonons constitute a large dissipative bosonic reservoir and provide a source of dephasing and relaxation. Short time correlations in the phonon bath induce a Markovian dynamics of the electron spin.

The electron spin and nuclear spins in a quantum dot couple via the hyperfine interaction, which creates entanglement between them and strongly affects the electron spin dynamics [58, 59]. It turns out that long time correlations in the nuclear spin system induce a non-Markovian dynamics of the electron spin, with non-exponential decay in time of the expectation values of the electron spin components.

In addition to the sources mentioned above, semiconducting qubits can also decohere due to Johnson noise from the metallic gates that are in the vicinity of quantum dots. The high density of evanescent modes (both electric and magnetic) nearby the metallic gates easily couple to quantum dots causing the loss of their phase coherence and consequently affecting both charge and spin qubits.

2.4 Modeling the dynamics of open quantum systems

Historically, description of open system dynamics has largely been based on the reduced density matrix formalism within which both intrinsic quantum mechanical fluctuations of the system and external noise of its environment can be conveniently incorporated in a unified manner. During the past few decades, efforts have been made to devise various phenomenological models and more recently, microscopic Hamiltonians have been used to describe an open quantum system. In this section, we outline two theoretical models/methods that are used to study the dynamics of a qubit device coupled to its environment in this thesis.

Lindblad master equation

In may cases, it is useful to model the dynamics of an open quantum system by means of an appropriate equation of motion for its density matrix, which is known as the quantum master equation. Here we consider the evolution of the density matrix of an open quantum system, without providing any connections to underlying microscopic physical model of the environment with which the system is coupled. This leads to a phenomenological description of dephasing and relaxation in the open quantum system, often known as Lindblad dissipator.

Consider a system-reservoir coupling which is uncorrelated at $t = 0$, namely:

$$\hat{W}(0) = \hat{\rho}(0) \otimes \hat{W}_R(0)\,, \tag{2.1}$$

where $\hat{W}, \hat{\rho}$, and $\hat{W}_R$ are density matrices of the entire system (qubit and its environment), a qubit device and a reservoir, respectively. Next, define a dynamical map $\mathcal{M}(t)$ describing

a transformation of the reduced system at $t = 0$ to some time $t > 0$ as:

$$\hat{\rho}(t) = \mathcal{M}(t)\hat{\rho}(0) = \mathrm{Tr}_R \left[\hat{U}(t,0)\hat{W}(0)\hat{U}^{\dagger}(t,0) \right], \tag{2.2}$$

where $\hat{U}(t,0)$ is a unitary operator that defines the evolution of the qubit and its environment combined. The map $\mathcal{M}$ represents a completely positive and trace preserving quantum operation. If t is allowed to vary in $\mathcal{M}(t)$, then it leads to a family of one parameter dynamical maps with $\mathcal{M}(0)$ being the identity map. If the characteristic time scales over which the reservoir correlation function decays are much smaller than the characteristic time scales of the qubit device, memory effects in the dynamics of the reduced density matrix equation can be neglected. This leads to a Markovian type behavior and may be formalized with the help of a semigroup property:

$$\mathcal{M}(t_1)\,\mathcal{M}(t_2) = \mathcal{M}(t_1 + t_2)\,, t_1\,, t_2 \geq 0\,. \tag{2.3}$$

Thus a quantum dynamical semigroup is a continuous, one-parameter family of dynamical maps satisfying the semigroup property (Markovian). If the quantum dynamical semigroup $\mathcal{M}(t)$ is contracting, then there exists a linear map $\mathcal{L}$ called a generator of the semigroup [60]:

$$\begin{aligned} \mathcal{M}(t) &= exp(\mathcal{L}t)\,, \quad \text{which leads to} \\ \frac{d\hat{\rho}}{dt} &= \mathcal{L}\,\hat{\rho}(t)\,. \end{aligned} \tag{2.4}$$

The construction of the most general form of the generator $\mathcal{L}$ leads to the Lindblad master equation. In the following, we present a derivation of the Lindblad form of equation of motion for the reduced density matrix of the qubit system, following Ref. [60].

The Hamiltonian of a global system is given by:

$$\hat{H} = \hat{H}_q + \hat{H}_R + \hat{V}\,, \tag{2.5}$$

where $\hat{H}_q$ and $\hat{H}_R$ are the qubit and reservoir Hamiltonians, respectively and $\hat{V}$ is the interaction Hamiltonian between the qubit and the reservoir. In the interaction picture, equation of motion of a full density matrix of the entire system $\hat{W}$ is given by the Von-Neumann equation:

$$\frac{d\hat{W}_I(t)}{dt} = \frac{1}{i\hbar}\left[\hat{V}_I(t), \hat{W}_I(t)\right]\,, \tag{2.6}$$

where the subscript I denotes the interaction picture. The formal solution of the above equation is given by:

$$\hat{W}_I(t) = \hat{W}_I(0) + \frac{1}{i\hbar}\int_0^t ds\,[\hat{V}_I(s), \hat{W}_I(s)]\,. \tag{2.7}$$

Inserting the integral equation into the Von-Neumann equation and tracing the bath variables out we obtain:

$$\frac{d\hat{\rho}_I}{dt} = -\frac{1}{\hbar^2}\int_0^t \mathrm{Tr}_R\left[\hat{V}_I(t), \left[\hat{V}_I(s), \hat{W}_I(s)\right]\right]\, ds\,, \tag{2.8}$$

where we assumed $\mathrm{Tr}_R\left[V_I(t), \hat{W}_I(0)\right] = 0$. The right hand side of the above equation still depends on the full density matrix, and this is where we make the first approximation. Within the *Born approximation*, it is assumed that the coupling between the system and the reservoir is negligibly weak so that the reservoir density matrix is negligibly affected by the interaction, and the total system after some time t is $\hat{W}_I(t) = \hat{\rho}_I(t) \otimes \hat{W}_I^R$, where $\hat{W}^R$ is the density matrix of the reservoir. This gives:

$$\frac{d\hat{\rho}_I}{dt} = -\frac{1}{\hbar^2}\int_0^t \mathrm{Tr}_R\left[\hat{V}_I(t), \left[\hat{V}_I(s), \hat{\rho}_I(s) \otimes \hat{W}_I^R\right]\right]\, ds\,. \tag{2.9}$$

A further simplification, $\hat{\rho}_I(s) \to \hat{\rho}_I(t)$, leads to the evolution of the qubit density matrix at time t dependent only on the present state. This assumption leads to the *Redfield* equation, which is local in time, but depends on the choice of the initial preparation at $t = 0$. Next, time-scale is coarse grained under an assumption that environmental excitations decay over times which are not resolved. In other words, the reservoir correlation is much smaller than the time scale over which the qubit state varies appreciably. This allows us to replace s by $t - s$ and send the upper limit of integration to ∞ in the above equation. Such an approximation is often known as the *Markovian approximation* and it leads to the following master equation:

$$\frac{d\hat{\rho}_I}{dt} = -\frac{1}{\hbar^2}\int_0^\infty \mathrm{Tr}_R\left[\hat{V}_I(t), \left[\hat{V}_I(t-s), \hat{\rho}_I(t) \otimes \hat{W}_I^R\right]\right]\, ds\,. \tag{2.10}$$

So far we have performed the Born-Markov approximation. However, these approximations do not guarantee a quantum dynamical semigroup evolution. A further approximation

involving the averaging over the rapidly oscillating terms in the master equation must be performed. Such an approximation is often known as the *rotating wave or secular approximation.* In order to demonstrate this, we first decompose the interaction Hamiltonian into eigenoperators of the system Hamiltonian:

$$\begin{aligned}
\hat{V}_I(t) &= \sum_{\alpha,\omega} e^{-i\omega t}\hat{A}_\alpha(\omega)\otimes\hat{B}_\alpha(t)\,, \quad \text{where} \\
\hat{A}_\alpha(\omega) &= \sum_{\epsilon'-\epsilon=\omega} \hat{\Pi}(\epsilon)\,\hat{A}_\alpha\,\hat{\Pi}(\epsilon') \quad \text{and} \\
\hat{B}_\alpha(t) &= e^{i\hat{H}_R t/\hbar}\,\hat{B}_\alpha\,e^{-i\hat{H}_R t/\hbar}\,.
\end{aligned} \tag{2.11}$$

Here $\hat{A}_\alpha, \hat{B}_\alpha$ denote operators belonging to the system and reservoir in the Schrodinger picture. $\hat{\Pi}(\epsilon)$ is the projection operator to the energy eigenstate of the system with energy ϵ. Here we assumed discrete energy spectrum of the system Hamiltonian. An immediate consequence of the above definition is that the following relation is satisfied: $[\hat{H}_q, \hat{A}_\alpha(\omega)] = -\omega\hat{A}_\alpha(\omega)$, that is, $\hat{A}_\alpha(\omega)$ lowers the qubit energy by ω while $\hat{A}^\dagger(\omega)$ raises it by ω. Inserting this form of interaction Hamiltonian into the Born-Markov master equation, Eq.[2.10], we obtain:

$$\frac{d\hat{\rho}_I}{dt} = -\frac{1}{\hbar^2}\sum_{\omega,\omega'}\sum_{\alpha,\beta} e^{i(\omega-\omega')t}\,\chi_{\alpha,\beta}(\omega')\left[\hat{A}_\beta(\omega)\hat{\rho}_I(t)\,\hat{A}^\dagger_\alpha(\omega') - \hat{A}^\dagger_\alpha(\omega')\,\hat{A}_\beta(\omega)\,\hat{\rho}_I(t)\right] + \text{h. c}\,, \tag{2.12}$$

where $\chi_{\alpha,\beta}(\omega')$ is the one-sided Fourier transform of the reservoir correlation functions given by:

$$\begin{aligned}
\chi_{\alpha,\beta}(\omega') &\equiv \int_0^\infty ds\, e^{i\omega' s}\,\langle\hat{B}^\dagger_\alpha(t)\,\hat{B}_\beta(t-s)\rangle\,, \quad \text{where} \\
\langle\hat{B}^\dagger_\alpha(t)\,\hat{B}_\beta(t-s)\rangle &\equiv \text{Tr}_R[\hat{B}^\dagger_\alpha(t)\,\hat{B}_\beta(t-s)\,\hat{W}^R_I]\,.
\end{aligned} \tag{2.13}$$

If $\hat{W}^R_I$ is a stationary state of the reservoir, $[\hat{V}_I, \hat{W}^R_I] = 0$, then the reservoir correlation functions are homogeneous in time

$$\langle\hat{B}^\dagger_\alpha(t)\,\hat{B}_\beta(t-s)\rangle = \langle\hat{B}^\dagger_\alpha(s)\,\hat{B}_\beta(0)\rangle\,. \tag{2.14}$$

In the above equation, $|\omega - \omega'|^{-1}$, where $\omega \neq \omega'$, defines the typical time scale associated with the intrinsic evolution of the qubit device. If the characteristic time scale is short compared to the relaxation time of the qubit device, the non-secular terms, that is, those for which $\omega \neq \omega'$ may be neglected since they oscillate very rapidly during the relaxation time when the qubit state varies appreciably. This is called the *rotating wave approximation*. With this, the evolution equation becomes:

$$\frac{d\hat{\rho}_I}{dt} = -\frac{1}{\hbar^2} \sum_{\omega} \sum_{\alpha,\beta} \chi_{\alpha,\beta}(\omega) \left[\hat{A}_\beta(\omega) \hat{\rho}_I(t)\, \hat{A}^\dagger_\alpha(\omega) - \hat{A}^\dagger_\alpha(\omega)\, \hat{A}_\beta(\omega)\, \hat{\rho}_I(t) \right] + \text{h. c}\,, \tag{2.15}$$

In the above equation, the term $\chi_{\alpha,\beta}$ can be rearranged as:

$$\begin{aligned}
&\chi_{\alpha,\beta}(\omega) = \frac{1}{2}\gamma_{\alpha,\beta} + iS_{\alpha,\beta}(\omega)\,, \quad \text{where} \\
&\gamma_{\alpha,\beta} = \chi_{\alpha,\beta}(\omega) + \chi^*_{\beta,\alpha}(\omega) = \int_{-\infty}^{\infty} ds\, e^{i\omega\, s}\, \langle \hat{B}^\dagger_\alpha(s)\, \hat{B}_\beta(0) \rangle\,, \quad \text{and} \\
&S_{\alpha,\beta}(\omega) = \frac{1}{2i} \left(\chi_{\alpha,\beta}(\omega) - \chi^*_{\beta,\alpha}(\omega) \right).
\end{aligned} \tag{2.16}$$

With these rearrangements, the equation of motion of the density matrix of the qubit can be written as:

$$\begin{aligned}
&\frac{d\hat{\rho}_I}{dt} = \frac{1}{i\hbar} \left[\hat{H}_{LS}\,, \hat{\rho}_I(t) \right] + \mathcal{D}[\hat{\rho}_I(t)]\,, \quad \text{where} \\
&\hat{H}_{LS} = \sum_{\omega} \sum_{\alpha,\beta} S_{\alpha,\beta}\, \hat{A}^\dagger_\alpha(\omega)\, \hat{A}_\beta(\omega)\,,
\end{aligned} \tag{2.17}$$

is called the Lamb shift since it leads to the Lamb type renormalization of the unperturbed energy levels of the qubit device due to coupling of the qubit to its environment. The term $\mathcal{D}[\hat{\rho}_I(t)]$ is called the dissipator and takes the following form:

$$\mathcal{D}[\hat{\rho}_I(t)] = \sum_{\omega} \sum_{\alpha,\beta} \gamma_{\alpha,\beta} \left(\hat{A}_\beta(\omega)\, \hat{\rho}_I(t)\, \hat{A}^\dagger_\alpha(\omega) - \frac{1}{2} \left\{ \hat{A}^\dagger_\alpha(\omega)\, \hat{A}_\beta(\omega)\,, \hat{\rho}_I(t) \right\} \right). \tag{2.18}$$

Since the term $\gamma_{\alpha,\beta}$ in the dissipator is the Fourier transform of the the homogeneous reservoir correlations functions, it is always positive and can be diagonalized. With that the evolution equations take the form of the standard Lindblad equation. We emphasize that the physical assumptions underlying the Lindblad form of the master equation are the

Born (weak coupling), Markov (memoryless) and rotating wave approximation (fast system dynamics compared to the relaxation time). Lindblad equation is suitable for problems where the above approximations are valid. In the next section, we relax the Markovian assumption and derive a new master equation.

Caldeira-Leggett master equation

In this section, we consider a "microscopic" model of the environment, which is modeled by a set of harmonic oscillators. Modeling environment by a bath of harmonic excitations above a stable ground state was first proposed by Caldeira and Leggett [61]. We derive the equation of motion of the reduced density matrix of the qubit, following Ref. [62]. In contrast to the Lindblad equation, here we do not make any Markovian approximation. We assume that system-reservoir coupling is a linear function of the system and bath coordinates. We also assume that the qubit is weakly coupled to each bath mode. The weak perturbation of any individual bath modes does not necessarily imply that the dissipative influence of the environment on the system is weak as well. This is because the coupling of bath modes add up and the number of modes can be very large, too. Here we treat bath modes as mechanical oscillators. For electrical environment, the complex impedance can be modeled by simply replacing mechanical oscillators by the LC-circuits [63].

The Hamiltonian of the global system is given by

$$\begin{aligned}
\hat{H} &= \hat{H}_q + \hat{H}_R + \hat{V}\,, \quad \text{where} \\
\hat{H}_q &= \hat{p}^2/2M + \hat{U}(\hat{q})\,, \\
\hat{H}_R &= \sum_{\alpha=1}^{N} \left(\frac{\hat{p}_\alpha^2}{2\,m_\alpha} + \frac{1}{2}\,m_\alpha\,\omega_\alpha^2\,\hat{x}_\alpha^2 \right), \\
\hat{V} &= \sum_{\alpha=1}^{N} \gamma_\alpha\,\hat{q}\,\hat{x}_\alpha\,.
\end{aligned} \tag{2.19}$$

Here $\hat{H}_q$ and $\hat{H}_R$ are the qubit system and reservoir Hamiltonians, respectively, and $\hat{V}$ is the interaction Hamiltonian between the qubit and its environment. It is also necessary to include a counter term in the form $\hat{H}_c = \hat{q}^2 \sum_{\alpha=1}^{N} \gamma_\alpha^2/2m_\alpha\omega_\alpha^2$ in the bare potential $\hat{U}(\hat{q})$ to

avoid a constant shift in the energy due to coupling of a qubit device to the bath of harmonic oscillators. However, this term by itself does not contribute to the dynamics of the system, hence we ignore this term in the following discussion. Assuming a weak coupling between the system and its environment, we can treat the system-reservoir interaction perturbatively. This allows us to solve the Von-Neumann equation 2.6 for the total density matrix of the entire system iteratively in powers of the coupling parameter. The solution can be written in the following form:

$$\hat{W}_I(t) - \hat{W}_I(0) = \frac{1}{i\hbar}\int_0^t \left[\hat{V}_I(t'), \hat{W}_I(0)\right]\, dt' + \frac{1}{(i\hbar)^2}\int_0^t \int_0^{t'} \left[\hat{V}_I(t'), \left[\hat{V}_I(t''), \hat{W}_I(t'')\right]\right]\, dt'\, dt'' \,. \tag{2.20}$$

Finally, expanding it to all orders of the coupling parameter, we obtain

$$\hat{W}_I(t) - \hat{W}_I(0) = \sum_{n\geq 1}^{\infty} \mathcal{T} \int_0^t dt' ..... \int_0^{t^{n-1}} dt^n \frac{1}{(i\hbar)^n} \left[\hat{V}_I(t'), ..., \left[\hat{V}_I(t^n), \hat{W}_I(0)\right] .....\right] \,, \tag{2.21}$$

where $\mathcal{T}$ is a time ordering operator. Considering only first two terms in the above expansion, we have

$$\hat{W}_I(t) = \hat{W}_I(0) + \frac{1}{i\hbar}\int_0^t \left[\hat{V}_I(t'), \hat{W}_I(0)\right]\, dt' - \frac{1}{\hbar^2}\int_0^t \int_0^{t'} \left[\hat{V}_I(t'), \left[\hat{V}_I(t''), \hat{W}_I(0)\right]\right]\, dt'\, dt'' \,. \tag{2.22}$$

In order to obtain the equation of motion of the reduced density matrix of the qubit, we trace the environment out followed by differentiation with respect to time. This leads to

$$\frac{d\hat{\rho}_I}{dt} = \frac{1}{i\hbar}\,\mathrm{Tr}_R\left[\hat{V}_I(t), \hat{W}_I(0)\right] - \frac{1}{\hbar^2}\int_0^t Tr_R\left[\hat{V}_I(t), \left[\hat{V}_I(t'), \hat{W}_I(0)\right]\right]\, dt' \,. \tag{2.23}$$

It is reasonable to approximate that the initial state of the qubit is decoupled from that of the reservoir. Therefore, the density matrix of the entire system at $t = 0$ can be factored into:

$$\hat{W}_I(0) = \hat{W}_I^R(0) \otimes \hat{\rho}_I(0) \,. \tag{2.24}$$

Tracing the reservoir out and rearranging terms in 2.22, one can immediately obtain an expression for $\rho_I(0)$. Using this expression for $\rho_I(0)$ along with 2.24 and keeping terms only

up to second order in the coupling parameter, Eq. 2.23 reduces to the following form:

$$\frac{d\hat{\rho}_I}{dt} = \frac{1}{i\hbar}\,\mathrm{Tr}_R\left[\hat{V}_I(t), \hat{W}_I^R(0)\otimes\hat{\rho}_I(t)\right] - \frac{1}{\hbar^2}\int_0^t \mathrm{Tr}_R\left[\hat{V}_I(t), \left[\hat{V}_I(t'), \hat{W}_I^R(0)\otimes\rho_I(t)\right]\right]\,dt' + \frac{1}{\hbar^2}\int_0^t \mathrm{Tr}_R\left[\hat{V}_I(t), \hat{W}_I^R(0)\otimes \mathrm{Tr}_R\left[\hat{V}_I(t'), \hat{\rho}_I(t)\right]\right]\,dt'\,. \tag{2.25}$$

Eq. 2.25 is the master equation written in the interaction picture. We can transform this back into the Schrodinger picture by

$$\frac{d\hat{\rho}}{dt} = \frac{1}{i\hbar}\left[\hat{H}_q(t), \hat{\rho}(t)\right] + \exp\left(\frac{-i\hat{H}_q t}{\hbar}\right)\frac{d\hat{\rho}_I}{dt}\exp\left(\frac{i\hat{H}_q t}{\hbar}\right)\,. \tag{2.26}$$

Assuming an initial state of the reservoir to be in equilibrium, that is, $\left[\hat{W}^R(0), \hat{H}_B\right] = 0$ and $\langle\hat{x}_\alpha(0)\rangle = 0$, which implies $\mathrm{Tr}_R\left[\hat{V}\,\hat{W}^R(0)\right] = 0$, the master equation in the Schrodinger picture can be simplified to the following form:

$$\begin{aligned}
\frac{d\hat{\rho}}{dt} &= \frac{1}{i\hbar}\left[\hat{H}_q(t), \hat{\rho}(t)\right] + \hat{\mathcal{L}}[\hat{\rho}(t)]\,, \quad \text{where} \\
\hat{\mathcal{L}}[\hat{\rho}(t)] &\equiv -\frac{1}{\hbar}\int_0^t K(t,t')\,\hat{q}\,\hat{q}(t'-t)\,\hat{\rho}(t)\,dt' + \frac{1}{\hbar}\int_0^t K(t',t)\,\hat{q}\,\hat{\rho}(t)\,\hat{q}(t'-t)\,dt' \\
&\quad + \frac{1}{\hbar}\int_0^t K(t,t')\,\hat{q}(t'-t)\,\hat{\rho}(t)\,\hat{q}\,dt' - \frac{1}{\hbar}\int_0^t K(t',t)\,\hat{\rho}(t)\,\hat{q}(t'-t)\,\hat{q}\,dt'
\end{aligned} \tag{2.27}$$

This can also be written in a more compact form as

$$\hat{\mathcal{L}}[\hat{\rho}(t)] \equiv -\frac{1}{\hbar}\int_0^t dt'\,\eta_1(t-t')\Big[\hat{q}\,,\Big[\hat{q}(t'-t),\,\hat{\rho}(t)\Big]\Big] + \frac{i}{\hbar}\int_0^t dt'\,\eta_2(t-t')\Big[\hat{q}\,,\Big\{\hat{q}(t'-t),\,\hat{\rho}(t)\Big\}\Big]\,. \tag{2.28}$$

Here the position operator $\hat{q}(t)$ is the Heisenberg operator. In Eq. 2.28, the time-dependent kernel $K(t,t')$ that appeared in 2.27 has been split into two parts η_1 and η_2, which are often referred to as quantum noise and dissipation kernel, respectively [63]. These quantities can be calculated analytically for the harmonic heat bath:

$$\begin{aligned}
K^\dagger(t',t) &= K(t,t') = K(t-t') \equiv \eta_1(t-t') - i\eta_2(t-t') \\
\eta_1(t-t') &= \frac{1}{2\hbar}\sum_{\alpha=1}^{N}\gamma_\alpha^2\left\langle\left\{\hat{x}_\alpha(t)\,,\hat{x}_\alpha(t')\right\}\right\rangle = \int_0^\infty J(\omega)\,[1+2\,N(\omega)]\cos(\omega(t-t'))\,d\omega\,, \\
\eta_2(t-t') &= \frac{i}{2\hbar}\sum_{\alpha=1}^{N}\gamma_\alpha^2\left\langle\left[\hat{x}_\alpha(t)\,,\hat{x}_\alpha(t')\right]\right\rangle = \int_0^\infty J(\omega)\sin(\omega(t-t'))\,d\omega\,.
\end{aligned} \tag{2.29}$$

Here the position operator of the bath mode $\hat{x}_\alpha(t)$ is the Heisenberg operator. The Planck's function $N(\omega) = 1/[\exp(\hbar\omega\beta) - 1]$ defines an average excitation number of environment modes with frequency ω and $\beta = \frac{1}{k_B T}$, where k_B is the Boltzmann's constant and T is the temperature of the heath bath. Here $J(\omega)$ is the spectral density of the reservoir, which is given by

$$J(\omega) = \sum_{\alpha=1}^{N} \frac{\gamma_\alpha^2 \delta(\omega - \omega_\alpha)}{2 m_\alpha \omega_\alpha} \tag{2.30}$$

It may also be useful to write the time dependent kernel $K(t, t')$ in the following form:

$$K(t, t') = K(t - t') = \int_0^\infty J(\omega) \Big[N(\omega) e^{i\omega(t-t')} + \{1 + N(\omega)\} e^{-i\omega(t-t')} \Big] d\omega \tag{2.31}$$

From this wee see that the kernel $K(t - t')$ is simply a Fourier transform of the spectral density $J(\omega)$ weighted by an average number of bath excitations for emission and absorption.

For Ohmic heat bath, the spectral density is given by

$$J(\omega) = 2\, M\, \gamma\, \omega\, exp(-\omega/\omega_s)\,, \tag{2.32}$$

where γ is frequency-independent damping rate and ω_s is the cut-off frequency. In order to obtain a memoryless heat bath, that is, $K(t-t') \to \delta(t-t')$ (approximately), the time-scale at which the bath changes appreciably $|t - t'|$ must be much shorter than the time-scale at which the qubit system changes appreciably. In other words, $|t - t'|\gamma << 1$. Since the maximum frequency contribution of the Ohmic bath is ω_s, we obtain a memoryless bath if $\omega_s >> \gamma$.

We also note that for the Ohmic heat bath and in the limit of high temperature $k_B T >> \hbar\omega_0$, Caldiera-Leggett master equation for the quantum Brownian motion (of a particle in a harmonic potential) reduces to that of Lindblad form, with Lindblad operator given by:

$$\hat{A} \equiv \frac{\sqrt{4 M k_B T}}{\hbar}\, \hat{q} + i \sqrt{\frac{1}{4 M k_B T}}\, \hat{p} \tag{2.33}$$

2.5 Discussion

In this chapter, we considered different sources of decoherence that affect superconducting and semiconducting qubits. Some of the mechanisms for decoherence in superconducting

circuits and quantum dots are external in nature, while the others are purely intrinsic and specific to the qubit device in question. We also discussed theoretical methods used to study the dynamics of an open quantum system. In the following chapters, we use methods discussed in this chapter to study the dynamics of a qubit coupled to its environment.

Chapter 3

Effect of the Ohmic environment on optimally controlled flux-biased phase qubit

3.1 Introduction

Superconducting circuits containing Josephson junctions are promising candidates for scalable quantum information processing [64]. However, small separations between successive quantum energy states in these circuits [65, 66] do not permit selective manipulation of a qubit in a two dimensional subspace and results in a dynamical leakage of the quantum state to a broader Hilbert space of the circuit. To reduce this leakage, Motzoi *et al.* [67] proposed Derivative Removal by Adiabatic Gate (DRAG) method, which reduces the gate error to 10^{-5} for an experimentally optimal gate time of 6 ns. This error is well below the required error threshold of 10^{-3} for fault tolerant quantum computation [68].

In addition to the dynamic leakage, any realistic model of a qubit must also address coupling of the qubit to its environment, which leads to further destruction of qubit states. Several efforts have already been made towards the study of accurate control of a qubit system [69, 70, 71]. However, the effect of environment on optimally controlled qubit has

only been studied in a phenomenological model [67], which leads to the evolution of density matrix of the qubit in the Lindblad form [72].

In this chapter, we resort to a microscopic approach to the modeling of the environment. We employ the Caldeira-Leggett model of the system-environment coupling, introduced in chapter 2, to describe the coupling of a flux-biased phase qubit, which is driven by the DRAG pulses, to the electromagnetic environment. Numerically solving equation of motion for the qubit density matrix, we study the dependence of the gate error on temperature, gate time and environmental coupling strength. Although numerous potential sources of decoherence in phase qubits have been identified experimentally [73, 74, 75], in this chapter, we focus on decoherence due to the Gaussian noise from the surrounding circuitry, which is introduced to the qubit system within the Caldeira-Leggett model. The study of the effect of ubiquitous low frequency $1/f$ noise on the gate error is out of the scope of this chapter.

We specifically study the role of dissipation in the gate error during the NOT gate operation. We find that for phase qubits with relaxation time $T_1 \approx 700$ ns [76], two-quadrature DRAG pulses proposed in Ref. [67] result in the gate error exceeding 7×10^{-3}, which is too high for fault tolerant quantum computation. We then address the limitation posed by the environmental coupling on two-quadrature pulses. Here we find that for optimal DRAG pulses [67], the coupling to environment must be reduced nearly by a factor of 6 to suppress the gate error below the required threshold. We also investigate the gate error for simple pulse shaping where the pulse amplitude of the first quadrature vary smoothly according to a Gaussian-shaped function while the amplitude of the second quadrature is proportional to the derivative of the first. In this case, however, the microwave drive frequency is held constant. For this pulse shape, we find that the gate error reduces to 10^{-3} for a gate time ≈ 7 ns when the coupling to environment is reduced by an approximate factor of 10 from the coupling in currently used phase qubits.

3.2 Model

A flux-biased phase qubit consists of a Josephson junction (JJ) embedded in a superconducting loop. The schematic of a flux-biased phase qubit is show in Fig. 3.1. Finite resistance of the JJ (see Fig. 3.1 (b)) results in dissipation processes in the qubit and can be accounted for by the Caldeira-Leggett model, discussed in the previous chapter. The full Hamiltonian of the qubit and the environment is

$$\hat{H} = \hat{H}_q + \hat{P}(t) + \hat{H}_R + \hat{V}. \tag{3.1}$$

The Hamiltonian of a flux-biased phase qubit $\hat{H}_q$ is written in terms of operators $\hat{Q}$ and $\hat{\delta}$, the charge and phase difference of the JJ respectively:

$$\hat{H}_q = \frac{\hat{Q}^2}{2C} + \frac{1}{2L}\left(\Phi_b - \frac{\Phi_0}{2\pi}\,\hat{\delta}\right)^2 - \frac{I_0\Phi_0}{2\pi}\,\cos\hat{\delta}\,, \tag{3.2}$$

where L (C) is the loop inductance (junction capacitance), Φ_b is the external magnetic flux applied to the phase qubit, I_0 is the critical current of the JJ, and $\Phi_0 = h/2e$ is the flux quantum. The qubit is capacitively coupled to a microwave current source, which is used to induce coherent transitions between the qubit states. This coupling introduces a time-dependent part in the Hamiltonian:

$$\hat{P}(t) = \frac{\Phi_0 I(t)}{2\pi}\hat{\delta}\,. \tag{3.3}$$

Here $I(t) = I_x(t)\cos\omega_d t + I_y(t)\sin\omega_d t$ is the microwave current with frequency ω_d. The coupling between the qubit system and the reservoir is bilinear in the JJ phase $\hat{\delta}$ and oscillator displacements $\hat{x}_\alpha$:

$$\hat{V} = \sum_{\alpha=1}^{N} \gamma_\alpha \hat{x}_\alpha \hat{q}\,, \quad \hat{q} \equiv \hat{\delta} - \frac{2\pi\Phi_b}{\Phi_0}\,, \tag{3.4}$$

where parameters γ_α determine the coupling strength between the qubit and reservoir mode α. Our goal is to describe the time evolution of the qubit density matrix $\hat{\rho}(t)$. The qubit is initially prepared in a pure state, corresponding to the density matrix $\hat{\rho}(0)$. Assuming that the environment is in a thermal equilibrium at temperature T, the master equation for $\hat{\rho}(t)$

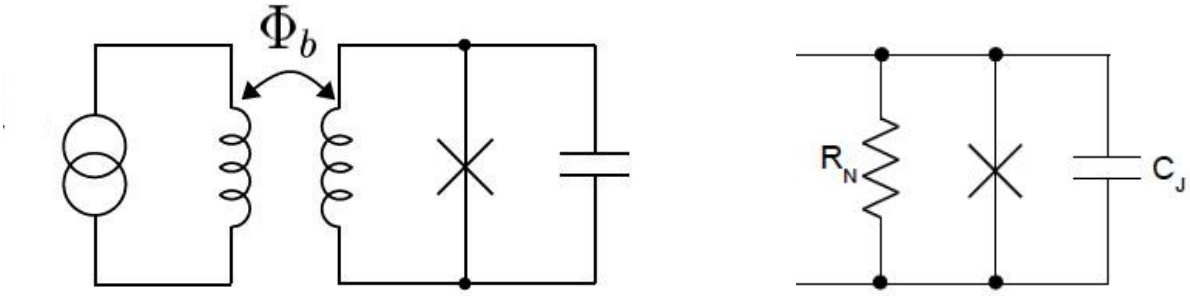

Figure 3.1: (a) Schematic of a flux-biased phase qubit, and (b) Resistively and capacitively shunted junction model (RCSJ)

takes the following form:

$$\frac{d\hat{\rho}(t)}{dt} = \frac{1}{i\hbar}\Big[\hat{H}_q(t),\, \hat{\rho}(t)\Big] + \hat{\mathcal{L}}[\hat{\rho}(t)]\ , \tag{3.5}$$

where the Caldeira-Leggett (CL) dissipative term $\hat{\mathcal{L}}[\hat{\rho}(t)]$ was derived in the previous chapter. Although the CL master equation 2.27, is local in time, it contains time-dependent coefficients, which capture memory effects of the noise due to the heat bath. Here we consider the spectral density for the Ohmic environment, which is given by

$$J(\omega) = \xi \frac{C}{4e^2}\hbar^2\omega_0\,\omega\, exp(-\omega/\omega_s)\ , \tag{3.6}$$

where ξ is a dimensionless coupling parameter, $\hbar\omega_0$ is the energy difference between the qubit states and ω_s is a cut-off frequency that exceeds all other frequency scales of the qubit system.

In typical experiments with phase qubits [76, 77], the "potential" part of $\hat{H}_q$ in 3.2 has one deep minimum and another very shallow minimum that disappears at the critical flux Φ_c. External flux Φ_b is chosen in such a way that only a few levels are localized in the shallow well, but these levels are still separated from levels localized in the deep well by impenetrable barrier [1]. As a result, we truncate the qubit Hamiltonian, Eqs. 3.2 and 3.3,

[1] The levels in the deep well can also be accounted in the present model, however, our numerical results indicate that the gate error does not change significantly if those levels are also included in the calculation for chosen values of parameters.

to three localized levels and obtain the following Hamiltonian:

$$\hat{H}_q(t) = \hbar \sum_{j=1}^{2} \left[\omega_{j-1} \hat{\Pi}_j + a \lambda_j \hat{\sigma}_j^+ + a^* \lambda_j \hat{\sigma}_j^- \right] + \hat{H}_{nr} \ , \tag{3.7}$$

where $\hat{\Pi}_j = |j\rangle\langle j|$ is the projector for the j^{th} level, $\hat{\sigma}_j^+ = |j\rangle\langle j-1|$ is the raising operator, $a = (I_x - iI_y)e^{i\omega_d t}/2$ is the amplitude of microwave drive, $\lambda_j = \Phi_0 \langle j|\hat{\delta}|j-1\rangle/2\pi\hbar$ is the matrix element of the phase operator, $\omega_j = (\varepsilon_{j+1} - \varepsilon_0)/\hbar$, ε_j is an energy eigenvalue of time-independent Hamiltonian H_q and $\hat{H}_{nr}$ contains non-resonant terms. In this three-level model, the lower two energy levels comprise qubit states while the third level accounts for a leakage level.

3.3 Gate error and DRAG method

In order to quantify the error during gate operation, we use gate fidelity averaged over two initial input states in a two dimensional Hilbert space, similar to one defined in Ref. [78]:

$$F_g = \frac{1}{2} \sum_{j=1}^{2} \mathrm{Tr} \left[\hat{U}_{ideal} \hat{\rho}_j^{(0)} \hat{U}_{ideal}^\dagger \hat{\rho}_j(t_g) \right] \ . \tag{3.8}$$

Here $\hat{U}_{ideal}$ represents an ideal evolution, $\hat{\rho}_j(t)$ is an actual density matrix of the qubit system with $\hat{\rho}_j(0) = \hat{\rho}_j^{(0)}$, and $\hat{\rho}_j^{(0)}$ represents two initial axial states in a Bloch sphere. The gate error E is defined as $E = 1 - F_g$.

A simple approach to minimize leakage of quantum information from the qubit subspace is to use a single-quadrature Gaussian envelope pulse given by

$$I_x(t) = I_\pi(t) = A\, e^{-(t-t_g/2)^2/2\sigma^2} - B, \ I_y(t) = 0 \ , \tag{3.9}$$

where t_g is a gate time and $\sigma = t_g/2$. For a NOT gate operation, which we choose to focus on without any loss of generality, constant B is chosen so that the Gaussian pulse starts and finishes off at zero and A is defined by

$$\int_0^{t_g} I_\pi(t)\, dt = \pi. \tag{3.10}$$

This pulse shape results in a large gate error, due to population of the third level, even for reasonably short pulses.

The DRAG method reduces the gate error to order of 10^{-5} for a gate time of 6 ns [67] by using two quadratures and time-dependent detuning $\Delta_1(t) = \omega_0 - \omega_d = (\lambda^2 - 4)I_\pi^2(t)/4\delta_{an}$, where the anharmonicity parameter $\delta_{an} \equiv \omega_1 - 2\,\omega_0$, and λ measures relative strength of $0 \to 1$ and $1 \to 2$ transitions, that is, $\lambda \equiv \lambda_2/\lambda_1$. The DRAG protocol uses second quadrature pulse to suppress the population of the third level generated by single quadrature drive. This is evident from the Hamiltonian written in the adiabatic frame (see below). We note that the laboratory frame is more suitable for the solution of the reduced density matrix of the qubit coupled to its environment. Therefore, we preserve the form of the quadrature amplitudes as in Ref. [67]

$$I_x = I_\pi + \frac{(\lambda^2 - 4)I_\pi^3}{8\delta_{an}^2}\ , \quad I_y = \frac{-\dot{I}_\pi}{\delta_{an}}\ , \tag{3.11}$$

and obtain the following equation for the microwave driving frequency for the Hamiltonian Eq. 3.7 in the laboratory frame

$$t\dot{\omega}_d(t) + \omega_d(t) = \omega_0 - \Delta_1(t)\ , \quad \omega_d(0) = \omega_0\ . \tag{3.12}$$

Although the DRAG correction is successful in reducing the gate error below the required threshold, practical implementation may not be feasible due to stringent requirement to vary microwave frequency. For this reason, we also consider two-quadrature pulses with fixed driving frequency $\omega_d = \omega_0$ [2]. We transform the Hamiltonian Eq. 3.7 to a frame rotating with frequency ω_d with respect to the laboratory frame and obtain:

$$\hat{H}^R = \hbar \sum_{j=1}^{2} \left[\Delta_j \hat{\Pi}_j + \frac{I_x(t)}{2} \lambda_j \hat{\sigma}_{j-1,j}^x + \frac{I_y(t)}{2} \lambda_j \hat{\sigma}_{j-1,j}^y \right]\ , \tag{3.13}$$

where $\Delta_2 = \delta_{an} + 2\,\Delta_1$, and for $\omega_d = \omega_0$, the detuning $\Delta_1 = 0$. We introduce operators $\hat{\sigma}_{j,k}^x = |k\rangle\langle j| + |j\rangle\langle k|$ and $\hat{\sigma}_{j,k}^y = i|k\rangle\langle j| - i|j\rangle\langle k|$.

To analyze the dynamics of rotating frame Hamiltonian H^R, it is convenient to perform an adiabatic transformation [67] $\hat{D}(t) = \exp\left[-iI_x(t)\left(\alpha\,\hat{\sigma}_{0,1}^y + \lambda\,\hat{\sigma}_{1,2}^y\right)/2\delta_{an}\right]$, which preserves the form of the gate, if $I_x(t)$ starts and finishes off at zero. This condition is satisfied

[2] We also made constant detuning of the driving frequency from ω_0, but did not see any improvement compared to $\omega_d = \omega_0$ case.

by our choice of $I_x(t)$ (see Eq. 3.9). The parameter α appearing in $\hat{D}$ is a dimensionless scaling parameter. After performing the transformation, the Hamiltonian, to first order in I_x/δ_{an}, takes the following form:

$$\begin{aligned}\frac{H^D}{\hbar} \approx \frac{I_x}{2}\,\hat{\sigma}^x_{0,1} + \frac{(4\alpha-\lambda^2)I_x^2}{4\delta_{an}}\,\hat{\Pi}_1 + \Big[\frac{\alpha\,\dot{I}_x}{2\delta_{an}} + \frac{I_y}{2}\Big]\,\hat{\sigma}^y_{0,1} \\ +\{\delta_{an} + \frac{(\lambda^2+2\,\alpha)\,I_x^2}{4\delta_{an}}\}\,\hat{\Pi}_2 + \Big[\frac{\dot{I}_x}{2\delta_{an}} + \frac{I_y}{2}\Big]\,\lambda\,\hat{\sigma}^y_{1,2} \\ + \frac{(2-\alpha)\,\lambda\,I_x^2}{8\delta_{an}}\,\hat{\sigma}^x_{0,2} + \frac{\lambda(\alpha-1)I_x\,I_y}{4\delta_{an}}\,\hat{\sigma}^y_{0,2}\,.\end{aligned} \tag{3.14}$$

We then require resonant condition for the microwave $\pi-$pulse in the qubit subspace and also eliminate the imaginary inertial term from the subspace, that is, require $\hat{\Pi}_1$ and $\hat{\sigma}^y_{0,1}$ terms in Eq. 3.14 to vanish, to obtain:

$$\alpha = \frac{\lambda^2}{4}\,, \quad I_x(t) = I_\pi(t)\,, \quad I_y(t) = \frac{-\alpha\dot{I}_\pi(t)}{\delta_{an}}\,, \tag{3.15}$$

where $I_\pi(t)$ is defined by Eqs. 3.9. The contributions to the gate error due to transitions to the third level come from the second and third lines of Eq. 3.14 except for $\hat{\Pi}_2$ term, which is not directly responsible for the gate error. Using the above expression for $I_y(t)$ and Eq. 3.10, we estimate the magnitude of these terms as

$$\begin{aligned}\hat{\sigma}^y_{1,2}: &\quad \Big[\frac{\dot{I}_x}{2\delta_{an}} + \frac{I_y}{2}\Big] \sim \frac{1}{\delta_{an}t_g^2}\,; \\ \hat{\sigma}^x_{0,2}: &\quad \frac{(2-\alpha)\,\lambda\,I_x^2}{8\delta_{an}} \sim \frac{1}{\delta_{an}t_g^2}\,; \\ \hat{\sigma}^y_{0,2}: &\quad \frac{\lambda(\alpha-1)I_x\,I_y}{4\delta_{an}} \sim \frac{1}{\delta_{an}^2 t_g^3}\,.\end{aligned}$$

These estimates show that the error due to $\hat{\sigma}^y_{1,2}$ and $\hat{\sigma}^x_{0,2}$ terms are comparable and results in the leading contribution to the gate error. In the case of a time-dependent detuning, the choice of pulses is such that it eliminates the error associated with $\hat{\sigma}^y_{1,2}$ term, and rescaling of the pulse intensity (I_π^3 term in Eq. 3.11) removes the contribution to the gate error due to $\hat{\sigma}^x_{0,2}$ term. This elimination of $\sim 1/(\delta_{an}t_g^2)$ explains high effectiveness of variable driving frequency DRAG pulses. For fixed frequency pulses, the pulse rescaling only marginally reduces the gate error.

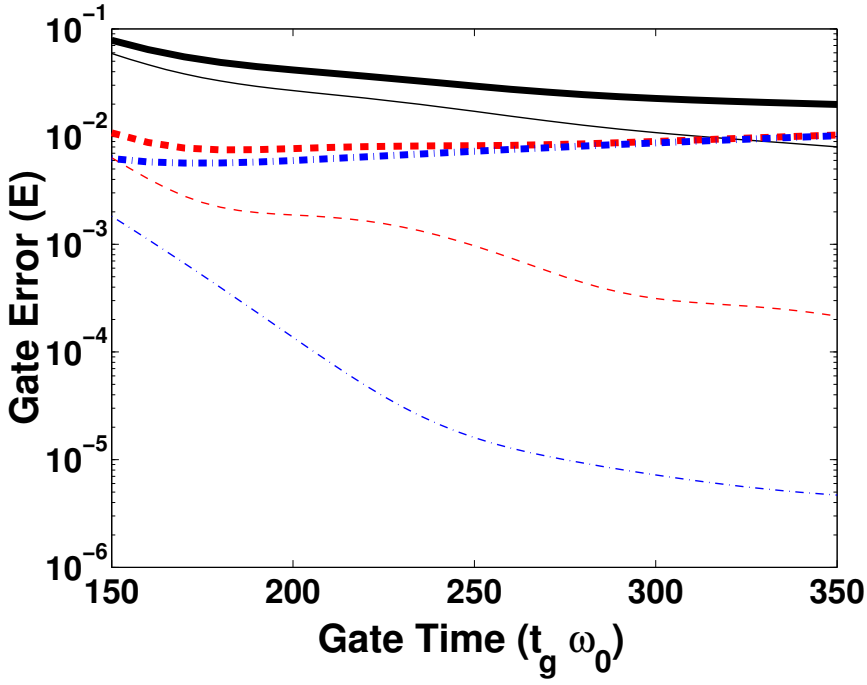

Figure 3.2: Gate error *vs.* gate time in log-normal scale with (thick lines) and without (thin lines) dissipation for a single quadrature Gaussian ($\sigma = 0.5\, t_g$) pulse (solid black), the Gaussian ($\sigma = 0.5\, t_g$) pulse with first order DRAG correction and dynamical detuning (dashed-dot blue), and the Gaussian ($\sigma = 0.5\, t_g$) pulse with fixed driving frequency $\omega_d = \omega_0$ and $\alpha = 0.5$ (dashed red), all in the laboratory frame. For the dissipative case, temperature $T = 0.1\, \hbar\omega_0$, the cutoff frequency $\omega_s = 10\, \omega_0$ and the coupling parameter $\xi = 2$.

3.4 Results

Qubit parameters used below in our simulation are typical of phase qubits: $C = 1$ pF, $I_0 = 1.5\, \mu$ A, $\beta_L = 2\pi I_0 L/\phi_0 = 3.2$ and $\Phi_b = 0.955\, \Phi_c$, where Φ_c is a critical flux. Numerical simulation indicates that small variations of qubit parameters do not incur any noticeable change in the gate error as long as there are at least three energy levels in the shallow well of the potential. For these experimental parameters, we numerically solve the time-independent Schrodinger's equation with the Hamiltonian given by Eq. 3.2. From this simulation, we obtain the following numerical values (rounded up to two decimal places): $\omega_0/2\pi = 6.2$ GHz, $\lambda = 1.42$ and $\delta_{an}/2\pi = -380$ MHz.

In Fig. 3.2, we plot the gate error for the DRAG pulses with and without time-dependent

detuning for an ideal phase qubit without environment. We find that pulses with two quadratures and fixed driving frequency (thin dashed red) perform much better than single quadrature Gaussian pulses (thin solid black), but are not as effective as pulses with double quadratures and time-dependent driving frequency (thin dashed-dot blue).

We verify numerically that the fixed frequency DRAG pulses give the minimal gate error for the choice of parameter α according to Eq. 3.15. As shown in Fig. 3.3(a), minimum value of the error occurs at around $\alpha = 0.5$ for different gate times, cf. dashed blue curve for $t_g\omega_0 = 250$ and solid black curve for $t_g\omega_0 = 350$. This result is consistent with Eq. 3.15, since for the phase qubit $\lambda = 1.42$, which implies $\alpha = 0.5$. For transmon qubits, discussed in Ref. [79], $\alpha = 0.4$ owing to different value of λ.

In order to study the effect of dissipation on the DRAG pulses, we integrate the master equation 4.4 numerically using the fourth and fifth order Runge-Kutta method. First, we consider relaxation of the qubit from the first excited state to the ground state in the absence of a microwave drive, shown in Fig. 3.3(b). For this simulation, we choose the cut-off frequency $\omega_s = 10\,\omega_0$ (throughout this paper), temperature $T = 0.1\,\hbar\omega_0$, and the coupling parameter $\xi = 2$ so that the relaxation time corresponds to experimentally observed decay time of $T_1 \approx 700$ ns for phase qubits [76]. We note that the spontaneous relaxation rate of the first excited state can also be evaluated from the master equation 4.4 as

$$\Gamma = \frac{1}{T_1} = 2\pi\hbar\omega_0^2 \frac{\xi C}{4e^2}|q_{01}|^2, \quad q_{01} = \langle 0|\hat{q}|1\rangle. \tag{3.16}$$

For the above choice of dimensionless coupling parameter ξ, temperature T and the cut-off frequency ω_s, we study the effect of dissipation on two-quadrature pulses.

In Fig. 3.2, we observe a non-monotonic behavior of the gate error with gate time for pulses with the DRAG corrections. We find that for shorter gate times, two-quadrature pulses with time-dependent driving frequency are weakly affected by dissipation (thick dashed-dot blue). However, for longer gate times, dissipation has a substantial effect on two-quadrature pulses. For instance, for a gate time of $\omega_0 t_g = 250$ ($t_g \approx 6$ ns), the gate error increases from 10^{-5} to higher order of 10^{-3} for two-quadrature pulses with dynamical detuning, when dissipation is taken into account. This increase in the gate error is due to

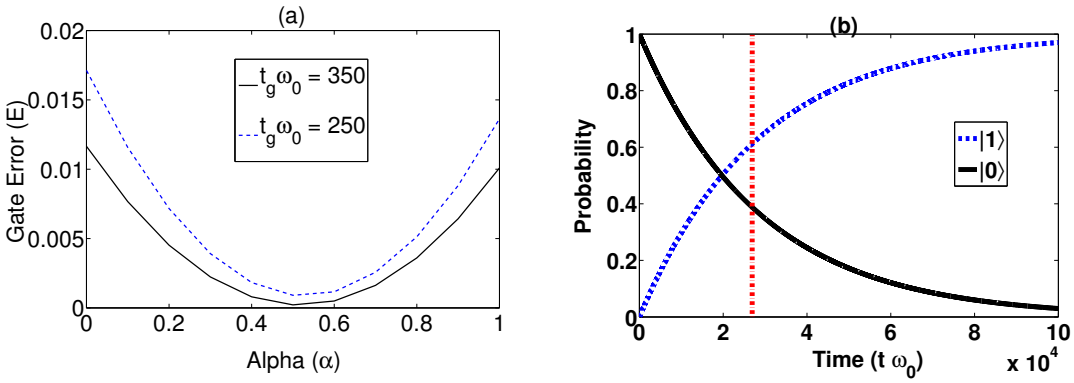

Figure 3.3: (a) Gate error *vs.* alpha for gate times $\omega_0 t_g = 250$ (dashed blue) and $\omega_0 t_g = 350$ (solid black). The phase qubit is driven by two-quadrature pulses with driving frequency $\omega_d = \omega_0$ in the absence of environment. (b) Probability *vs.* time for temperature $T = 0.1\,\hbar\omega_0$, coupling parameter $\xi = 2$ and cut-off frequency $\omega_s = 10\,\omega_0$. The microwave pulse is turned off and the qubit is initially prepared in $|1\rangle$ state (solid black), which relaxes to $|0\rangle$ state (dashed blue) due to dissipation.

relaxation of the qubit from the excited state to the ground state, which becomes prominent for longer gate times. For comparison, we plot the gate error for three different types of pulses: single-quadrature Gaussian pulse (thick solid black), the Gaussian pulse with first order DRAG correction and time-dependent driving frequency (thick dashed-dot blue) and the Gaussian pulse with two quadratures and fixed driving frequency (thick dashed red). One can conclude from these plots that the performance of two-quadrature pulses without detuning is comparable to the DRAG pulses with dynamical detuning when dissipation is included.

Next, we study the effect of environmental coupling strength on the gate error. In Fig. 3.4, we plot the gate error for different coupling parameters ξ for the phase qubit driven by two-quadrature pulses with dynamical detuning. In this simulation, we consider the temperature $T = 0.1\,\hbar\omega_0$, and coupling parameters: $\xi = 0$ (thin dashed-dot blue), $\xi = 0.1$ (thick solid green with circles), $\xi = 0.3$ (thick solid red) and $\xi = 2$ (thick dashed-dot blue). At $\xi = 0$ the gate error originates entirely due to microwave-induced leakage of the qubit state from the lowest two level subspace. The environment-induced transition rates increase with increase in the environmental coupling strength ξ (see Eq. 3.16). As

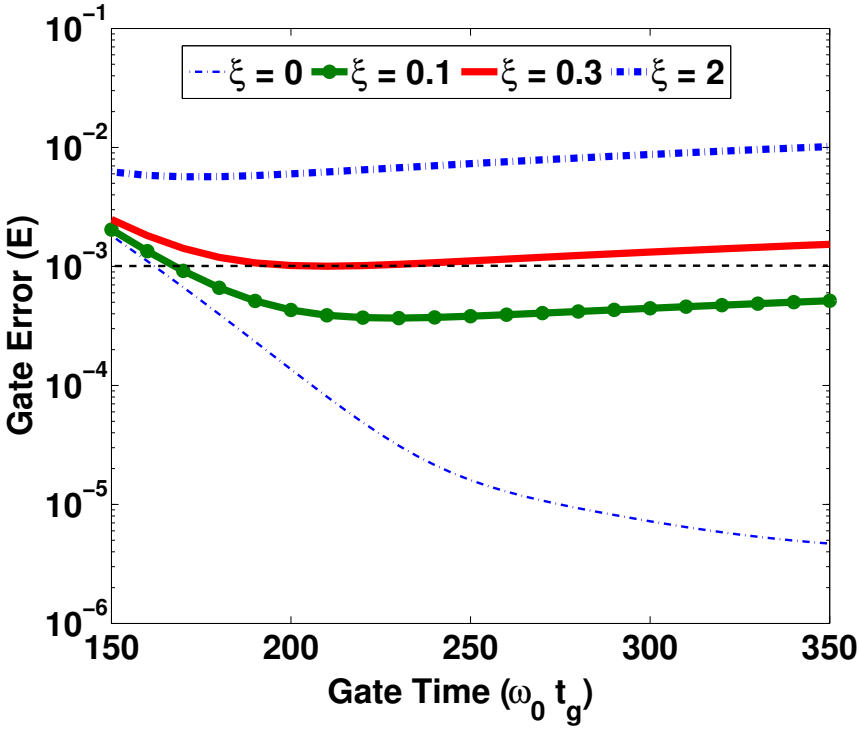

Figure 3.4: Gate error *vs.* gate time in log-normal scale for the Gaussian ($\sigma = 0.5\,t_g$) pulse with variable frequency DRAG correction for temperature $T = 0.1\,\hbar\omega_0$ and cut-off frequency $\omega_s = 10\,\omega_0$. The environmental coupling parameters: $\xi = 0$ (thin dashed-dot blue), $\xi = 0.1$ (thick solid green with circles), $\xi = 0.3$ (thick solid red) and $\xi = 2$ (thick dashed-dot blue).

a result, the gate error also increases, which is corroborated by Fig. 3.4. One can infer from the plot that two-quadrature pulses with time-dependent driving frequency suppress the gate error to 10^{-3} for $\xi = 0.3$ and gate time $\omega_0 t_g \approx 200$ ($t_g \approx 5.5$ ns). This indicates that an increase in the relaxation time nearly by a factor of 6 from the currently observed value is necessary to suppress the error below the threshold for fault tolerant computation. We further analyze the effect of environmental coupling on fixed frequency two-quadrature pulses for a range of gate times. For this case, gate errors for different values of ξ are plotted in Fig. 3.5, where the temperature is the same as above and coupling parameters are: $\xi = 0$ (thin dashed red), $\xi = 0.1$ (thick solid green with circles), $\xi = 0.2$ (thick solid blue), $\xi = 0.5$ (thick solid black with triangles) and $\xi = 2$ (thick dashed red). These plots indicate that the DRAG pulses with fixed driving frequency can effectively suppress the gate error if the

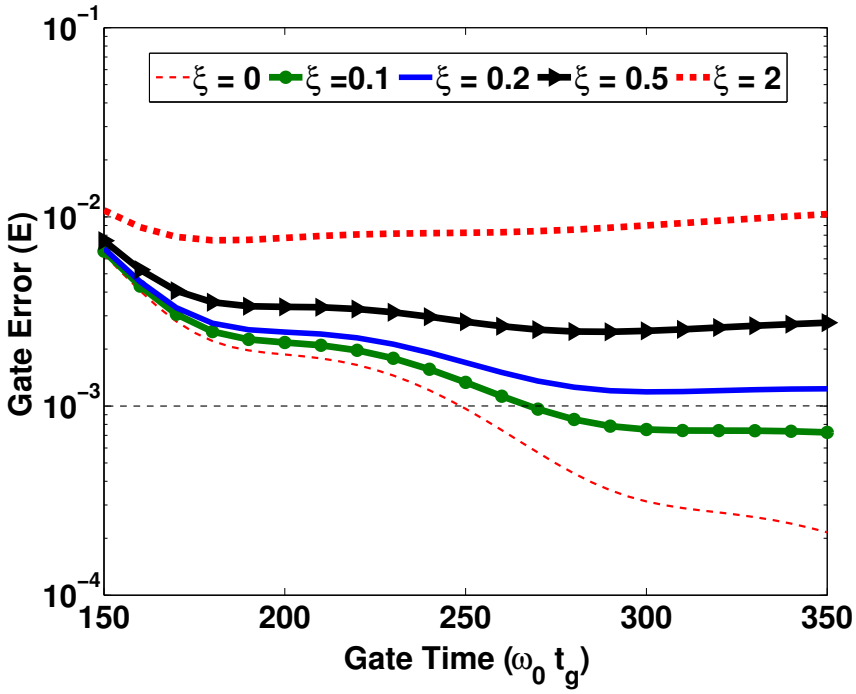

Figure 3.5: Gate error *vs.* gate time in log-normal scale for the Gaussian ($\sigma = 0.5\,t_g$) pulse with fixed frequency DRAG correction for temperature $T = 0.1\,\hbar\omega_0$ and cut-off frequency $\omega_s = 10\,\omega_0$. The environmental coupling parameters: $\xi = 0$ (thin dashed red), $\xi = 0.1$ (thick solid green with circles), $\xi = 0.2$ (thick solid blue), $\xi = 0.5$ (thick solid black with triangles) and $\xi = 2$ (thick dashed red).

environmental coupling strength is weakened and gate times are slightly longer than $6\,ns$. More specifically, for $\xi = 0.2$ and a gate time of $\omega_0 t_g \approx 300$ ($t_g \approx 7$ ns), the gate error is close to 10^{-3}. Therefore, we conclude that the relaxation time must be nearly a factor of 10 longer than the currently observed value to attain the threshold of the gate error for fixed frequency DRAG pulses. This is a much better improvement compared to single-quadrature pulses for which the gate error never reduces to the threshold for a reasonable choice of gate times even in an ideal case, that is, $\xi = 0$, as shown in Fig. 3.2. Finally, we investigate the effect of the temperature on the gate error. In Fig. 3.6, we plot the gate error normalized to the error at zero temperature for two different gate times: $\omega_0 t_g = 150$ (dashed-dot blue) and $\omega_0 t_g = 350$ (dashed black). The plot shows a monotonic growth of the gate error as the temperature increases due to enhancement in the relaxation rate. We compare results

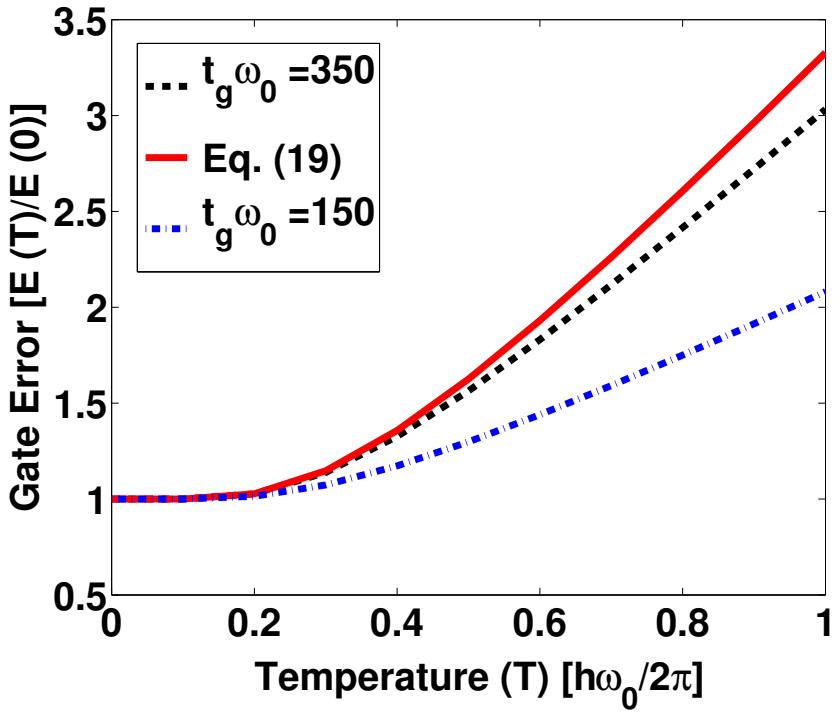

Figure 3.6: Normalized gate error *vs.* temperature for the Gaussian ($\sigma = 0.5\,t_g$) pulse with varying frequency DRAG correction. In numerical simulation, environmental coupling parameter $\xi = 2$ and cut-off frequency $\omega_s = 10\,\omega_0$ are used for gate times $\omega_0 t_g = 150$ (dashed-dot blue) and $\omega_0 t_g = 350$ (dashed black). Analytical rate equation estimation of the normalized gate error (solid red).

of the numerical solution of the master equation 4.4, and a simple picture of the error due to coupling to the environment in terms of the "Fermi-Golden rule" transition rates. Considering the environment at zero temperature and assuming that the contribution to the error E from the environment is small, $E \ll 1$, we can evaluate the error as the probability of an excitation of a reservoir mode during the qubit operation, which happens with rate Γ: $E(T=0) = \Gamma t_g \overline{\rho_{11}(t)}$, where $\overline{\rho_{11}(t)} = \int_0^{t_g} \rho_{11}(t)dt/t_g$ is the time-average of the probability of the qubit being in the first excited state. At finite temperature, processes with excitation of environment happen with rate $\Gamma(T) = \Gamma[1 + N(\omega)]$. In addition, the qubit can absorb an excitation from the environment with rate $\Gamma N(\omega)$. We combine the qubit excitations from the ground to first excited state and the first to second excited state with the relaxation from the first to ground state and obtain the following estimate for the gate error due to

coupling to the environment:

$$\frac{E(T)}{\Gamma t_g} = \left[\{1 + N(\omega_0)\} + \lambda^2 N(\omega_1 - \omega_0)\right] \overline{\rho_{11}(t)} + N(\omega_0)\overline{\rho_{00}(t)}\,. \tag{3.17}$$

Assuming the average occupation of the ground and first excited states to be $\approx 1/2$, and for a weak anharmonicity of the qubit system $|\delta_{an}| \ll \omega_0$, the gate error reduces to

$$\frac{E(T)}{E(0)} \approx 1 + 4N(\omega_0)\,. \tag{3.18}$$

The estimated normalized gate error (solid red) is plotted in Fig. 3.6 together with the gate error obtained from the numerical simulation. The rate equation estimate of the error is fairly close to the error obtained from direct numerical simulation for a longer gate time (dashed black). However, for a shorter gate time (dashed-dot blue), the estimated error deviates from the exact numerical simulation considerably suggesting that the rate equation description may not be valid for shorter gate times, as well as for higher temperatures.

3.5 Discussion

In this chapter we compared possible choices of microwave pulses for the NOT gate operation in fluxed-biased qubits. Particularly, we considered three options: single-quadrature pulses and two-quadrature microwave (control) pulses with both variable and fixed frequencies. Two-quadrature pulses led to significant suppression of the gate error compared to single-quadrature pulses. However, the presence of dissipative environment increased the gate error even for two-quadrature pulses significantly above the required threshold for fault tolerant quantum computation in currently available phase qubits. We further investigated how the environmental coupling strength affects the gate error and found that an improvement of the qubit relaxation time is crucial for effectiveness of the DRAG pulses. We determined that two-quadrature pulses with fixed driving frequency suppressed the gate error below the required threshold for a reasonable gate time of 7 ns, but for qubits with the relaxation time ten times longer than the currently observed relaxation times. Similarly, our analysis indicated that two-quadrature pulses with dynamical detuning can also

effectively reduce the gate error below the required threshold if the relaxation time is longer by at least a factor of 6. In comparison to fixed frequency DRAG pulses, this is a moderate improvement over the longer relaxation time requirement, yet not impressive enough to overcome the difficulty associated with implementing control pulses with variable driving frequency. We expect that in a trade-off between complicated driving frequency and longer relaxation times, the DRAG pulses with fixed frequency are viable alternatives for reducing the gate error. We emphasize that for single-quadrature pulses, reduction of the gate error below the error threshold of 10^{-3} is not possible for reasonable gate times, even in an ideal case without any dissipation.

In addition, we observed a monotonic increase in the gate error with the temperature, which is due to increase in the relaxation rate with the temperature. We found that the temperature dependence of the gate error for longer pulses can be captured by a simple error estimation based on the rate equations. Nonetheless, these estimates of the error for shorter pulses differs from the gate error obtained from direct numerical solution of the reduced density matrix. Therefore, full density matrix solution is necessary to calculate the error for shorter gate times.

Chapter 4

Microwave photon detector based on a current-biased Josephson junction

4.1 Introduction

Quantum optical photodetectors have contributed significantly to the development of quantum optics and atomic physics [80] and now play an essential role in optical quantum information applications such as quantum computing and quantum key distribution [81, 82]. Recently, circuit quantum electrodynamics (cQED) has emerged as a novel paradigm for the study of radiation-matter interaction in mesoscopic systems [83, 84, 85]. Moreover, cQED is an attractive candidate for scalable quantum computing and transmission of quantum information [86, 87]. Following the original proposal, a variety of cQED architectures demonstrating strong coupling between single photons and superconducting integrated circuits have been realized experimentally [88, 89]. This work has paved the way for the development of a superconducting microwave photon detector [90, 91] with possible applications to quantum information processing and communication [92].

The microwave photon detector is based on the current-biased Josephson junction (JJ):

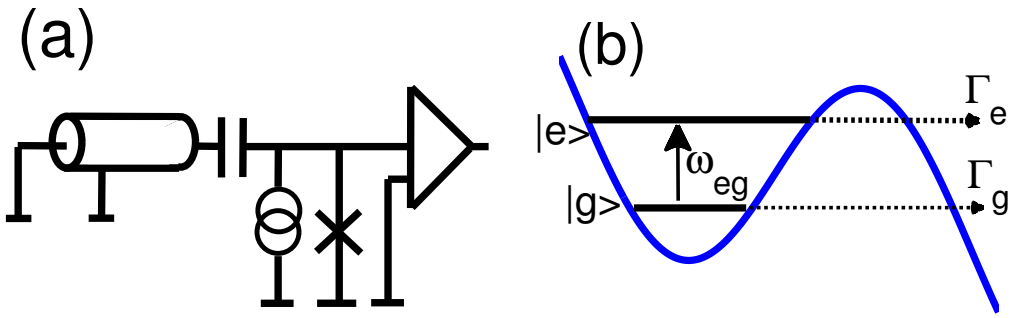

Figure 4.1: (a) Schematic circuit diagram of JJ-based microwave photon detector coupled to a resonator. (b) Potential energy landscape of the detector when bias current is close to the critical current of the JJ . The junction is initialized in the $|g\rangle$ state and upon absorbing an incident photon transitions to the $|e\rangle$ state, which rapidly tunnels to the continuum.

the JJ is biased so that absorption of a single microwave photon induces a transition to the voltage state, producing a large and easily detected classical signal. While these detectors are straightforward to operate and show potential for scalability, performance is degraded by spurious dark counts due to quantum tunneling events in the absence of an absorbed photon; moreover, energy relaxation within the detector results in photon loss and leads to a reduction in measurement efficiency.

In this work, we theoretically determine the quantum efficiency of a microwave photon detector based on a current-biased JJ. Previous analysis [93, 94] of this system was focused on a wave-packet formulation of the photon field in a transmission line coupled to the detector. Here we study the probability of photon detection by a JJ coupled to a microwave cavity mode that is loaded with a fixed number of photons [95]. We solve the equation of motion for the density matrix of the cavity-JJ system to obtain detector efficiency for different values of operation time, current bias, and relaxation time of the junction. Our results indicate that a JJ with decay time around 10 ns can detect a single microwave photon in the cavity with an efficiency greater than 80%, for readily achievable circuit parameters. We also find that the detector efficiency increases significantly with increasing energy relaxation time T_1 of the junction, suggesting that a highly efficient single microwave photon detector is attainable for moderate improvements in junction quality.

4.2 Josephson-junction based photon detector

The circuit diagram of the JJ-cavity system is shown in Fig. 4.1(a). The JJ is biased with a current I close to the critical current I_0. The junction Hamiltonian can be written in terms of the charge operator $\hat{Q}$ and the operator $\hat{\delta}$ of the phase difference across the JJ [96]:

$$\hat{H}_{JJ} = \frac{\hat{Q}^2}{2C} + U(\hat{\delta}), \quad U(\hat{\delta}) = -\frac{I_0\Phi_0}{2\pi}\left(\cos\hat{\delta} - \frac{I}{I_0}\hat{\delta}\right). \tag{4.1}$$

Here C is the junction capacitance and $\Phi_0 = h/2e$ is the magnetic flux quantum. For $I \lesssim I_0$, the potential energy landscape $U(\delta)$ takes on a "tilted washboard" shape, with a few discrete energy levels in shallow minima separated from the continuum by a barrier, see Fig. 4.1(b). We truncate the junction Hamiltonian to the ground $|g\rangle$ and first excited states $|e\rangle$ and obtain the following Hamiltonian for the JJ:

$$\hat{H}_{JJ} = \hbar\omega_{eg}\hat{\Pi}_e\,, \tag{4.2}$$

where $\hat{\Pi}_e = |e\rangle\langle e|$ is the projection operator to the excited state and $\omega_{eg} = (\varepsilon_e - \varepsilon_g)/\hbar$.

The coupling of the cavity with the JJ is modeled by the Jaynes-Cummings (JC) Hamiltonian [97]:

$$\hat{H}_{JC} = \hbar\omega_r\left(\hat{a}^\dagger\hat{a} + \frac{1}{2}\right) + \hbar\omega_{eg}\hat{\Pi}_e + \frac{\hbar\Omega}{2}(\hat{a}^\dagger\hat{\sigma}_- + \hat{a}\hat{\sigma}_+)\,, \tag{4.3}$$

where ω_r is the cavity resonance frequency, Ω is the vacuum Rabi frequency, and $\hat{a}^\dagger(\hat{a})$, $\hat{\sigma}_+(\hat{\sigma}_-)$ are the creation (annihilation) operators of the cavity and the junction, respectively.

The time evolution of the density matrix $\hat{\rho}(t)$ of the cavity-JJ system coupled to its environment is governed by the following equation:

$$\frac{d\hat{\rho}(t)}{dt} = \frac{1}{i\hbar}\Big[\hat{H}_{JC},\,\hat{\rho}(t)\Big] + \hat{\mathcal{L}}_\gamma[\hat{\rho}(t)] + \hat{\mathcal{L}}_\kappa[\hat{\rho}(t)] + \hat{\mathcal{L}}_T[\hat{\rho}(t)]\,, \tag{4.4}$$

where $\hat{\mathcal{L}}_\gamma[\hat{\rho}(t)]$ and $\hat{\mathcal{L}}_\kappa[\hat{\rho}(t)]$ are superoperators that capture damping in the JJ and the cavity at low temperatures $T \ll \hbar\omega_{eg}$, $\hbar\omega_r$ [98]:

$$\hat{\mathcal{L}}_\kappa[\hat{\rho}(t)] = \kappa\left(\hat{a}\hat{\rho}\hat{a}^\dagger - \frac{1}{2}\{\hat{a}^\dagger\hat{a}, \hat{\rho}\}\right), \tag{4.5a}$$

$$\hat{\mathcal{L}}_\gamma[\hat{\rho}(t)] = \gamma\left(\hat{\sigma}_-\hat{\rho}\hat{\sigma}_+ - \frac{1}{2}\{\hat{\sigma}_+\hat{\sigma}_-, \hat{\rho}\}\right). \tag{4.5b}$$

To account for switching of the ground and the first excited states of the JJ to the voltage state, we introduce the tunneling superoperator $\mathcal{L}_T[\hat{\rho}(t)]$ [99, 100, 101, 102]:

$$\hat{\mathcal{L}}_T[\hat{\rho}(t)] = -\begin{pmatrix} \Gamma_e\rho_{ee}^{nn} + \frac{\sqrt{\Gamma_e\Gamma_g}}{2}(\rho_{eg}^{nm} + \rho_{ge}^{nm}) & \frac{\Gamma_e+\Gamma_g}{2}\rho_{eg}^{nm} + \frac{\sqrt{\Gamma_e\Gamma_g}}{2}(\rho_{ee}^{nm} + \rho_{gg}^{nm}) \\ \frac{\Gamma_e+\Gamma_g}{2}\rho_{ge}^{nm} + \frac{\sqrt{\Gamma_e\Gamma_g}}{2}(\rho_{ee}^{nm} + \rho_{gg}^{nm}) & \Gamma_g\rho_{gg}^{nn} + \frac{\sqrt{\Gamma_e\Gamma_g}}{2}(\rho_{eg}^{nm} + \rho_{ge}^{nm}) \end{pmatrix}, \tag{4.6}$$

where $\Gamma_{e,g}$ are the tunneling rates from the ground ($|g\rangle$) and first excited ($|e\rangle$) states of the junction. If we approximate the potential in Eq. 4.1 by a cubic potential, then the tunneling rate of the ground and the first excited states of the cubic potential can be computed by WKB approximation:

$$\Gamma_j = \omega_p/2\pi[432\Delta U/\hbar\omega_p]^{j+1/2}/\pi^{j/2}\exp[-36\Delta U/5\hbar\omega_p]\,,$$

where $\Gamma_{j=0} \equiv \Gamma_g$ and $\Gamma_{j=1} \equiv \Gamma_e$ represent the tunneling rates from the $|g\rangle$ and $|e\rangle$ states of the JJ, respectively. The ratio $\Gamma_e/\Gamma_g \approx 250\Delta U/\hbar\omega_p$. Here $\Delta U = 4I_0\Phi_0/3\sqrt{2}\pi(1-I/I_0)^{3/2}$ is the barrier height and $\omega_p = 2^{1/4}\sqrt{2\pi I_0/C\Phi_0}(1-I/I_0)^{1/4}$ is the plasma frequency of the cubic potential. The junction frequency ω_{eg} is related to the plasma frequency by $\omega_{eg} \simeq \omega_p(1-5\hbar\omega_p/36\Delta U)$. The tunneling rate of the first excited state of the junction is then given by $\Gamma_e \approx 500\,\Gamma_g = 7.3\times10^7\,\mathrm{s}^{-1}$ for $\Delta U/\hbar\omega_p \approx 2$.

4.3 Quantum efficiency

The system is originally prepared in a pure state $\hat{\rho}_n(0) = |n,g\rangle\langle n,g|$ with n photons in the cavity and the junction in the ground state $|g\rangle$. We assume n photons are loaded into the cavity in a manner similar to that described by Hofheinz *et al.* [25], with loading rate faster than the interaction rate between the JJ and the cavity. With this assumption, the detector efficiency is unaffected by how photons are loaded into the cavity. We numerically solve the above equation for the time evolution of the density matrix to compute the occupation probabilities of the cavity and junction states. The probability that the JJ has switched to

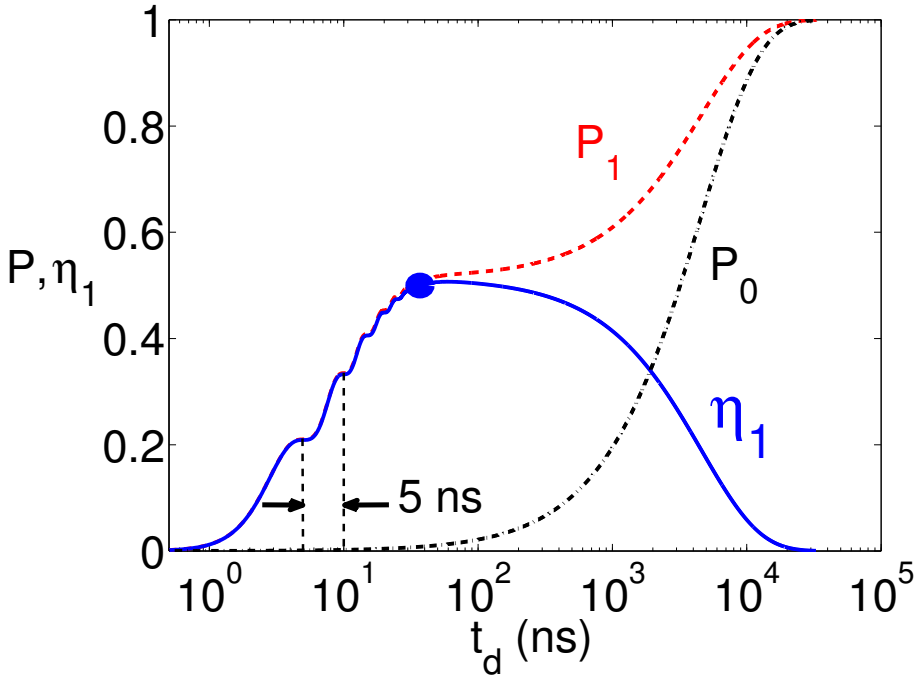

Figure 4.2: Switching probability P_1 (P_0) *vs.* photon detection time for initial states $|1, g\rangle$ ($|0, g\rangle$). Parameters used in this plot are: junction $T_1 = 10\,\text{ns}$, barrier height $\Delta U/\hbar\omega_p = 2$, vacuum Rabi frequency $\Omega/2\pi = 200\,\text{MHz}$, and cavity decay time $1/\kappa = 1\,\mu\text{s}$. Here the detuning between the cavity and the junction $\Delta = 0$. The solid blue curve is the quantum efficiency $\eta_1 \equiv P_1 - P_0$ (see text). The maximum quantum efficiency of the detector is 50% for an optimal detection time of 45 ns (the optimal point is marked by the filled blue circle).

the voltage state at time t is given by

$$P_n(t) = 1 - \text{Tr}\,[\hat{\rho}_n(t)]. \tag{4.7}$$

4.4 Result

We consider the following set of parameters for the JJ-cavity system, typical of those realized in experiments [91]: JJ frequency $\omega_{eg}/2\pi = 4.8\,\text{GHz}$, junction decay rate $\gamma = 10^8\,\text{s}^{-1}$, cavity decay rate $\kappa = 10^6\,\text{s}^{-1}$, and vacuum Rabi frequency $\Omega/2\pi = 200\,\text{MHz}$. In Fig. 4.2, we plot switching probabilities $P_1(t), P_0(t)$ of the junction for initial states $|1, g\rangle$ (solid red) and $|0, g\rangle$ (solid black), respectively. In this simulation, the parameters we consider are $\Delta U/\hbar\omega_p = 2$ and we set the detuning between the cavity and the JJ to zero, i.e.,

$\Delta \equiv \omega_r - \omega_{eg} = 0$. The switching probability P_1 in Fig. 4.2 features steps whose periodic occurrence is a manifestation of Rabi oscillations of the JJ with period $2\pi/\Omega = 5\,\mathrm{ns}$. This result is consistent with the picture that switching of the JJ halts momentarily when the junction returns to the ground state in course of the Rabi oscillations.

Next, we discuss the presence of the wide plateau of P_1 in Fig. 4.2. The occurrence of this plateau can be understood from the fact that switching of the junction is briefly frozen when the junction relaxes to the ground state due to dissipation. The JJ then switches to the voltage state after time $\sim 1/\Gamma_g$, the characteristic time scale for switching of the junction in the case of zero photons. The height of this plateau can be estimated as $\Gamma_e/\big(\Gamma_e + \gamma\big) \approx 0.5$, which agrees with the numerical result in Fig. 4.2.

In order to determine the quantum efficiency of the detector, we must properly treat dark counts due to quantum tunneling from the $|0, g\rangle$ state in the absence of photon absorption. The quantum efficiency η_1 of the detector is defined as the difference between the switching probabilities for an initial state with one photon $P_1(t)$, and for an initial state with no photons $P_0(t)$: $\eta_1 \equiv P_1(t) - P_0(t)$. The quantum efficiency is shown in Fig. 4.2 by the solid blue curve. For our choice of parameters $\Gamma_e \simeq \gamma$, the detector has maximum efficiency of about 50% for the optimal detection time t_d around 45 ns. Next, we demonstrate that the bandwidth of the Josephson microwave photon detector is broadened due to the finite lifetime of the junction excited state. Here, we vary the frequency ω_r of the cavity and compute the quantum efficiency of the detector for the optimal detection time t_d obtained at zero detuning $\Delta = 0$. The detector bandwidth is then given by the detuning at which the quantum efficiency of the detector is reduced to half the efficiency obtained at zero detuning. For a dissipation–free junction, the detector bandwidth is approximately given by the vacuum Rabi frequency. However, in the presence of dissipation and tunneling, the first excited state of the junction is broadened by $\sim \gamma + \Gamma_e$. This broadening of the energy level roughly accounts for the increased bandwidth of the detector. We find that bandwidths are factors of 1.6, 2 and 2.3 larger than the vacuum Rabi frequency for bias points $\Delta U/\hbar\omega_p = 2, 1.9$ and 1.8, respectively, as shown in Fig. 4.3. As we lower the

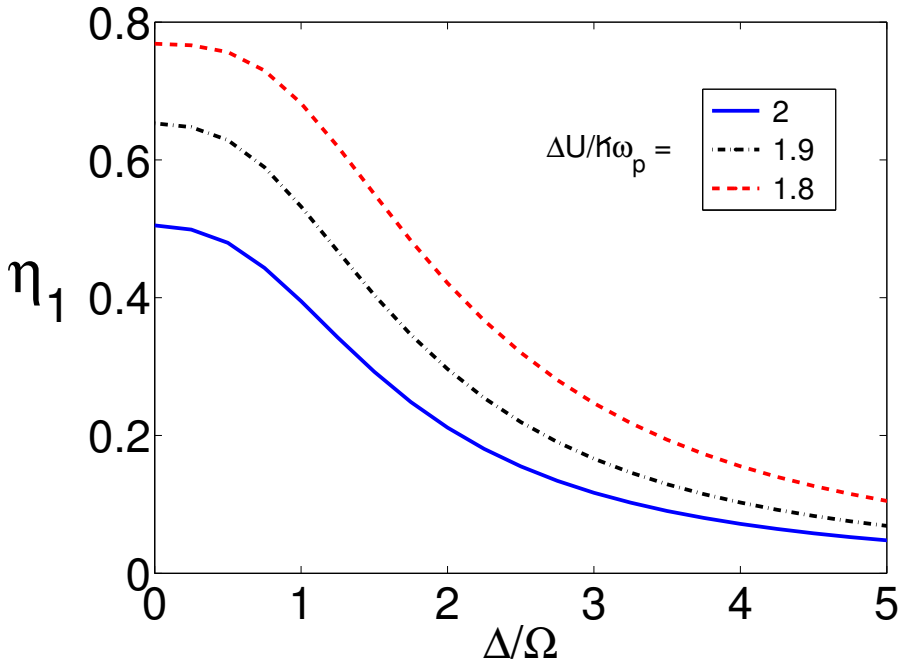

Figure 4.3: Quantum efficiency η_1 *vs.* detuning Δ/Ω for optimal detection time obtained at $\Delta = 0$ for various bias points: $\Delta U/\hbar\omega_p = 2$ (solid blue), 1.9 (dashed-dot black), and 1.8 (dashed red). The bandwidths of the detector are 1.6Ω (solid blue), 2Ω (solid black) and 2.3Ω (solid red), respectively. The remaining parameters are as in Fig. 4.2.

ratio $\Delta U/\hbar\omega_p$, the tunneling rate Γ_e of the first excited state of the junction increases. This in turn causes further broadening of the junction excited state thereby increasing the bandwidth of the detector. Next, we analyze the effect of dissipation and bias point on the efficiency of the detector. In Fig. 4.4(a), we plot the quantum efficiency of the detector for different values of the junction relaxation time T_1 from 10 ns to 500 ns, keeping all other parameters the same as in Fig. 4.2. We find that the quantum efficiency increases with increasing junction relaxation time T_1 and reaches 94% for $T_1 = 500\,\text{ns}$ and for a detection time around 95 ns.

The change in bias current I of the junction modifies the ratio of barrier height ΔU to the junction plasma frequency ω_p. Taking different values of this ratio, we compute the efficiency of the detector at fixed relaxation time $T_1 = 10$ ns; the results are shown in Fig. 4.4 (b). Upon decreasing the ratio $\Delta U/\hbar\omega_p$, the potential well becomes shallower,

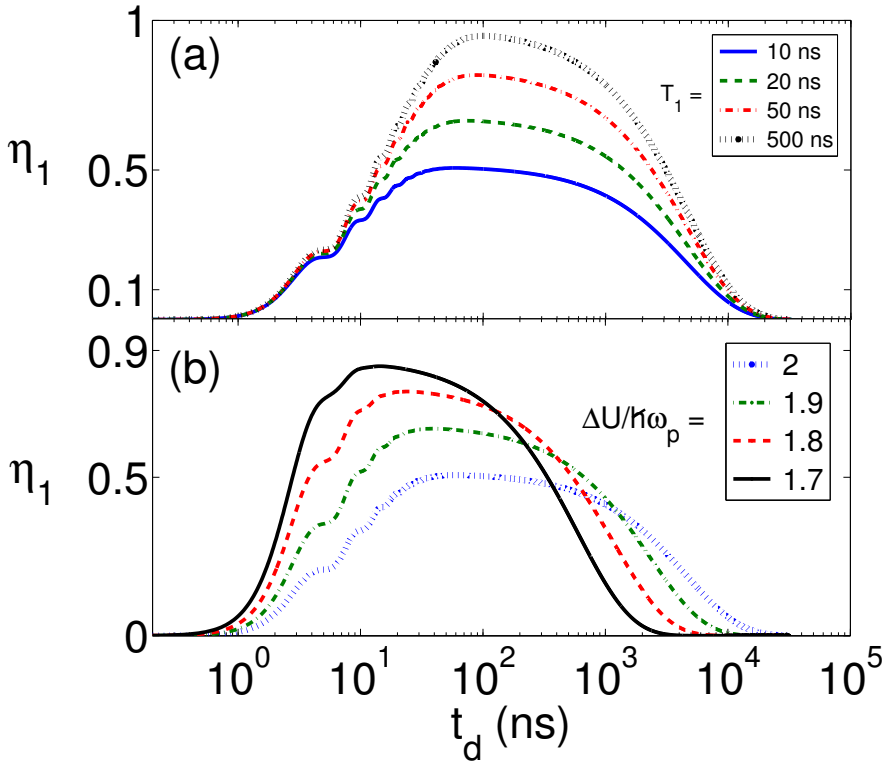

Figure 4.4: (a) Quantum efficiency η_1 *vs.* photon detection time for $\Delta U/\hbar\omega_p = 2$ and for various decay times of the junction: $T_1 = 10\,\text{ns}$ (solid blue), $T_1 = 20\,\text{ns}$ (dashed green), $T_1 = 50\,\text{ns}$ (dash-dotted red), and $T_1 = 500\,\text{ns}$ (dotted black). For $T_1 = 500$ ns, the maximum quantum efficiency is 94%. (b) Quantum efficiency η_1 *vs.* photon detection time for junction $T_1 = 10\,\text{ns}$ for various bias points of the junction: $\Delta U/\hbar\omega_p = 2$ (dotted blue), 1.9 (dash-dotted green), 1.8 (dashed red) and 1.7 (solid black). The maximum quantum efficiency is 84% for $\Delta U/\hbar\omega_p = 1.7$. The remaining parameters are as in Fig. 4.2.

leading to enhanced tunneling out of the first excited state and increased efficiency of the detector. Our simulation results indicate that a significant improvement in detector efficiency is achieved when the tunneling rate exceeds the dissipation rate of the junction. We find that for the bias point $\Delta U/\hbar\omega_p = 1.7$, the efficiency of the detector is about 84% for a detection time around 9 ns. Finally, we analyze the efficiency of the detector to detect single photons when the cavity is loaded with $n > 1$ photons. Generalizing the previous case of a single photon in the cavity, the efficiency to detect a single microwave photon in a cavity loaded with n photons is given by $\eta_n = P_n(t) - P_0(t)$. In Fig. 4.5, we plot the efficiency at fixed bias point $\Delta U/\hbar\omega_p = 2$ and $T_1 = 10$ ns for different numbers of

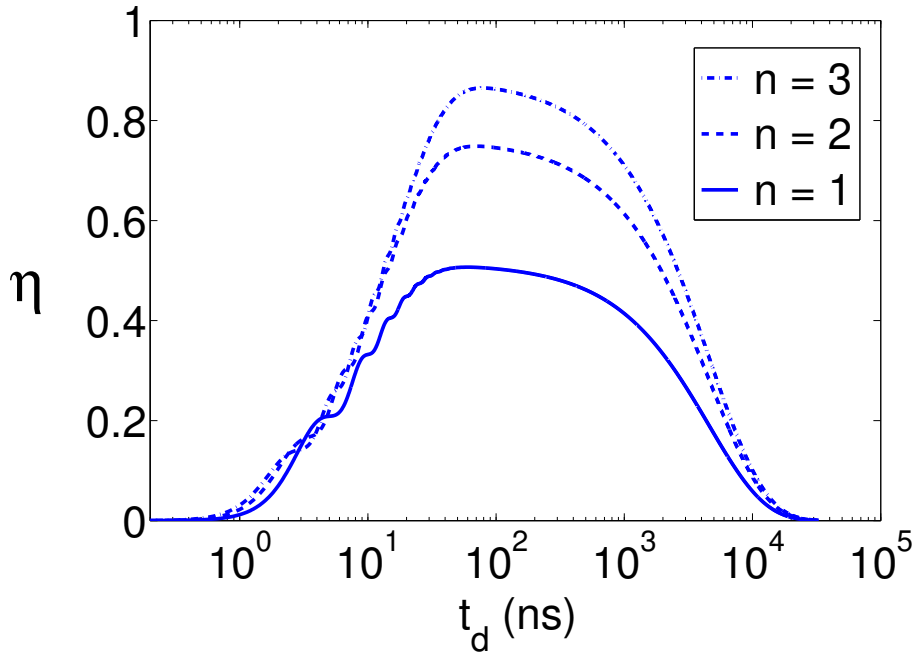

Figure 4.5: Efficiency η_n to detect a photon *vs.* detection time for $n = 1$ (solid blue), 2 (dashed blue), and 3 (dash-dotted blue) photons in the cavity. The rest of the parameters are as in Fig. 4.2. For three photons in the cavity, the efficiency to detect a photon is 85%.

photons in the cavity: $n = 1$ (solid blue), 2 (dashed blue), and 3 (dash-dotted blue). We find that detection efficiency increases with the increasing number of photons in the cavity and reaches 85% for three photons in the resonator. This result is consistent with previous studies [93, 91] that reported a higher detection efficiency, for the same parameters as above, when a continuous flux of photons was incident on the detector. For the case of a single photon in the cavity, the detector returns to the ground state after the photon is absorbed by the environment, and no further excitation of the junction is possible. However, when multiple photons are present in the cavity, other photons are available to induce excitation if the junction relaxes, thereby increasing the probability of photon detection. We note that for multiple photons in the cavity, the measured efficiency η can also be used to estimate the average number of photons in the cavity.

Recently, Peropadre *et al.* [94] proposed a phenomenological model for the JJ-based microwave photon detector that fails to address specific microscopic details of experimentally realized detectors [91]. Specifically: (1) Peropadre *et al.* treat tunneling from the

excited state of the junction by a non-hermitian term in the junction Hamiltonian; this is not consistent with the standard form of quantum tunneling. (2) These authors do not consider tunneling from the low-energy state of the junction, which is responsible for dark counts of the detector. (3) Finally, their model does not take into account the relatively strong relaxation from the excited to the ground state of the junction. This relaxation corresponds to a T_1 time of order of a few nanoseconds in present devices, which are strongly coupled to a 50 Ω readout line, and is responsible for a significant suppression of detector efficiency [91]. If the relaxation time were above 500 ns, the efficiency would reach nearly 100%, see Fig. 4(a).

4.5 Input-output theory and reflection coefficient

For practical realization of a photon detection scheme discussed in the previous section, it is important to address several issues that one may encounter in a real experiment. One of such concerns that directly impacts the detection efficiency is the power reflected by the detector. Since our goal is to maximize the detection efficiency, it is crucial to minimize the power reflected by the detector. In this section, we investigate the condition for minimizing the power reflected by the photon detector. We apply input-output theory [103] to calculate the reflection coefficient of the detector connected to a microwave source through a transmission line, taking into account switching behavior of and/or dissipative effect in the junction.

Consider a Josephson junction (JJ) biased with a current I close to the critical current I_0. The Lagrangian of the junction is given by:

$$\mathcal{L}[\dot{\Phi},\Phi] = \frac{C_J}{2}\Big(\frac{\partial\Phi}{\partial t}\Big)^2 - U(\Phi)\,, \quad \text{where } U(\Phi) = -E_J\cos(\tfrac{2\pi\Phi}{\Phi_0}) - \Phi I \quad \text{and } \Phi_0 \equiv h/2e. \tag{4.8}$$

If we expand the potential function around the local minimum $\Phi_{min} = \frac{\Phi_0}{2\pi}\sin^{-1}(I/I_0)$, we obtain

$$U(\Phi) = \frac{1}{2L_J}(\Phi - \Phi_{min})^2 + \ \mathcal{O}(\Phi^3)\,. \tag{4.9}$$

Here C_J and L_J are the junction's capacitance and inductance, respectively. We will assume that the JJ is positioned at $x = 0$ and is connected to a transmission line (left) whose characteristic impedance $Z_l = \sqrt{\frac{L_l}{C_l}}$, where L_l and C_l are the inductance and capacitance per unit length of the transmission line. Similarly, we model the Ohmic loss in the junction (tunneling in JJ can also be modeled this way) by connecting the junction in parallel to a semi-infinite transmission line (right) whose characteristic impedance $Z_r = \sqrt{\frac{L_r}{C_r}}$, where L_r and C_r are the inductance and capacitance per unit length of the right transmission line.

Far away from the junction (i. e., $x > 0$ or $x < 0$), the flux field $\Phi_{l,r}(x,t)$ in the left or right transmission line satisfies the following wave equation:

$$\frac{\partial^2 \Phi_{l,r}(x,t)}{\partial t^2} - v_{l,r}^2 \frac{\partial^2 \Phi_{l,r}(x,t)}{\partial x^2} = 0\,, \quad \text{where the phase velocity } v_{l,r} \equiv \sqrt{\frac{1}{L_{l,r} C_{l,r}}}. \tag{4.10}$$

The solution to the wave equation is given by [104]

$$\Phi_{l,r}(x,t) = \int_0^\infty \sqrt{\frac{\hbar Z_{l,r}}{2}} \frac{d\omega}{2\pi\sqrt{\omega}} \Big[a_{l,r}^{in}(\omega) e^{i(\pm k_{l,r} x - \omega t)} + a_{l,r}^{out}(\omega) e^{i(\mp k_{l,r} x - \omega t)} + h.c. \Big] \tag{4.11}$$

where $|k_{l,r}| = \frac{\omega}{v_{l,r}}$. The continuity of the flux field at $x = 0$ requires

$$\Phi_l(0-,t) = \Phi_r(0+,t)\,. \tag{4.12}$$

The discontinuity in the derivative (w.r.t. x) of the flux field at $x = 0$ leads to the Kirchhoff's current law, which is equivalent to the Euler-Lagrange equation of motion derived from the total Lagrangian density of the system (or Hamilton equation of motion in Hamiltonian formulation):

$$\frac{1}{L_l} \frac{\partial \Phi_l(0-,t)}{\partial x} - \frac{1}{L_r} \frac{\partial \Phi_r(0+,t)}{\partial x} + C_J \frac{\partial^2 \Phi_l(0,t)}{\partial t^2} + \frac{\Phi_l(0,t)}{L_J} = 0\,. \tag{4.13}$$

Plugging in the solution of the wave equation into the boundary conditions, Eqs. 4.12 and 4.13, we obtain:

$$\begin{aligned}
&\sqrt{Z_l} a_l^{out}(\omega) - \sqrt{Z_r} a_r^{out}(\omega) = -\sqrt{Z_l} a_l^{in}(\omega) + \sqrt{Z_r} a_r^{in}(\omega) \\
&X a_l^{out}(\omega) + Y a_r^{out}(\omega) = -X^* a_l^{in}(\omega) + Y a_r^{in}(\omega)\,, \quad \text{where} \\
&X \equiv \sqrt{\frac{Z_l}{L_J^2 \omega}} - \sqrt{C_J^2 Z_l \omega^3} - i\sqrt{\frac{\omega}{Z_l}} \quad \text{and} \quad Y \equiv -i\sqrt{\frac{\omega}{Z_r}}\,.
\end{aligned} \tag{4.14}$$

If we ignore the right input amplitude for a moment, we get $a_l^{out}(\omega) = R(\omega)\, a_l^{in}(\omega)$, where the reflection coefficient $R(\omega)$ is given by:

$$R(\omega) = -\frac{\omega_p Z_l Z_r - \omega^2 C_J Z_J Z_l Z_r + i\omega(Z_J Z_r - Z_J Z_l)}{\omega_p Z_l Z_r - \omega^2 C_J Z_J Z_l Z_r - i\omega(Z_J Z_r + Z_J Z_l)}\,. \tag{4.15}$$

Here $\omega_p = \sqrt{1/L_J C_J}$ and $Z_J = \sqrt{L_J/C_J}$ are the plasma frequency and the impedance of the junction, respectively. From the above expression for reflection coefficient, we see that for $Z_l = Z_r$ and $\omega = \omega_p$, we have $R = 0$.

This calculation indicates that the power reflected by the detector is minimal when the impedance of the transmission line is equal to the impedance due to tunneling or any internal loss in the detector. It also requires a resonance condition, namely, $\omega = \omega_p$.

4.6 Power absorbed by the detector

So far we only considered a detection model where the resonator was loaded with a fixed number of photons, which were then detected by a detector that was capacitively coupled to the resonator. Alternatively, in a more realistic setting, one can have a classical microwave source directly connected to the detector, or a microwave driven resonator connected to the detector. In this section, we present a rigorous method to compute the power absorbed by the detector in these alternative set-ups. This is an important calculation since one can show that the power absorbed by the detector is directly related to the efficiency of the photon detector. The schematics of circuit diagrams of a microwave driven resonator connected to a JJ and a microwave driven JJ are shown in Fig. 4.6.

Formalism

Here we present a formalism to compute the power absorbed by the detector in the presence of decoherence. Since the photon detector we consider here switches from a supercurrent state to the voltage state upon absorbing photons, we would like to characterize the wait time between the reset of the junction and switching to the voltage state. The wait time is often specified by a probability distribution which is known as the waiting time distribution.

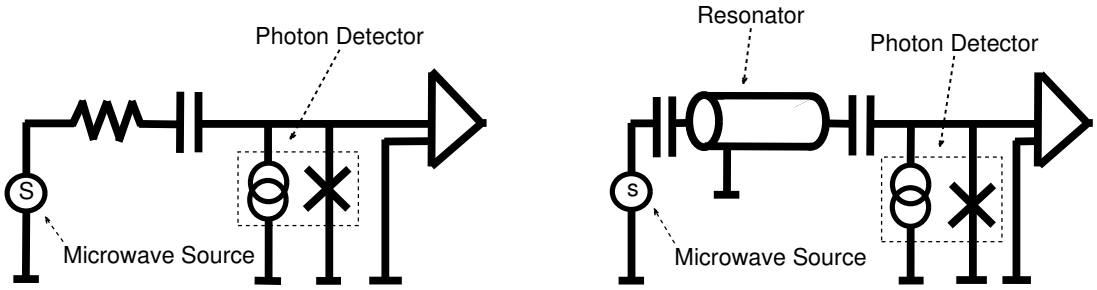

Figure 4.6: Schematic circuit diagram of JJ-based microwave photon detector (a) driven by a classical microwave source, (b) coupled to a microwave driven resonator.

This distribution allows us to compute the average switching rate of the detector, which is proportional to the power absorbed by the detector. In the following, we provide a derivation for the waiting time distribution[105].

For the sake of generality, we will not specify the Hamiltonian explicitly and simply denote it by $\hat{H}_{sys}$, which can represent either of the detection schemes shown in the circuit diagrams above. The time evolution of the density matrix of this system is characterized by a Liouvillian superoperator $\hat{\mathcal{L}}_{total}$,

$$\frac{d\hat{\rho}(t)}{dt} = \hat{\mathcal{L}}_{total}[\hat{\rho}(t)] \equiv \hat{\mathcal{L}}_0[\hat{\rho}(t)] + \hat{\mathcal{J}}_e[\hat{\rho}(t)] + \hat{\mathcal{J}}_g[\hat{\rho}(t)]\,, \quad \text{where} \tag{4.16}$$

$$\hat{\mathcal{L}}_0[\hat{\rho}(t)] \equiv \frac{1}{i\hbar}[\hat{H}_{sys}, \hat{\rho}(t)] + \hat{\mathcal{L}}_{dissip}[\hat{\rho}(t)]\,. \tag{4.17}$$

Here $\hat{\mathcal{L}}_{dissip}$ is the Lindblad superoperator that characterizes the dissipation in system in consideration and $\hat{\mathcal{J}}_i$ is the tunneling jump operator of the JJ from the **i**nitial metastable state $|\mathbf{i} \equiv g, e\rangle$ (or supercurrent state) to the final voltage state $|\mathbf{r}\rangle$ (or **r**esistive state), defined as

$$\hat{\mathcal{J}}_i[\hat{\rho}(t)] = \Gamma_i\, \hat{s}_i\, \hat{\rho}(t)\, \hat{s}_i^\dagger\,, \quad \text{where } \hat{s}_i \equiv \textstyle\sum_n |n, r\rangle\langle n, i|. \tag{4.18}$$

$\Gamma_{g,e}$ are tunneling rates from the ground and exited states, respectively and n is the number of photons in the resonator, if the resonator is present in the model. Since the tunneling rate from the ground state, which contributes to the dark count of the detector, is orders of magnitude smaller compared to the tunneling rate from the excited state, we neglect the

tunneling rate from the ground state in the following discussion. With this simplification, $\hat{\mathcal{L}}_0$ can be re-defined in terms of effective non-Hermitian Hamiltonian by absorbing the tunneling jump operator $\hat{\mathcal{J}}_e$ into it in the following way:

$$\hat{\mathcal{L}}_0[\hat{\rho}(t)] = \frac{1}{i\hbar}\Big(\hat{H}_{eff}\hat{\rho}(t) - \hat{\rho}(t)\hat{H}^{\dagger}_{eff}\Big) + \hat{\mathcal{L}}_{dissip}[\hat{\rho}(t)]\,, \quad \text{where} \tag{4.19}$$

$$\hat{H}_{eff} \equiv \hat{H}_{sys} - \frac{i\hbar\Gamma_e}{2}\hat{s}^{\dagger}_e\,\hat{s}_e\,. \tag{4.20}$$

For time-independent Liouvillian, the formal solution of the density matrix equation can be written as

$$\hat{\rho}(t) = e^{\hat{\mathcal{L}}_0+\hat{\mathcal{J}}_e}\,\hat{\rho}_{in} = \sum_{n=0}^{\infty}\int_0^t dt_n \int_0^{t_n} dt_{n-1}\cdots\cdots\int_0^{t_2} dt_1\, e^{\hat{\mathcal{L}}_0(t-t_n)}\,\hat{\mathcal{J}}_e\, e^{\hat{\mathcal{L}}_0(t_n-t_{n-1})}\,\hat{\mathcal{J}}_e\cdots$$
$$\cdots\cdots\,\hat{\mathcal{J}}_e\, e^{\hat{\mathcal{L}}_0(t_2-t_1)}\,\hat{\mathcal{J}}_e\, e^{\hat{\mathcal{L}}_0 t_1}\,\hat{\rho}_{in}\,. \tag{4.21}$$

One can define a conditioned density matrix (un-normalized) as

$$\hat{\rho}^c(\{t_1\cdots t_n\}) = e^{\hat{\mathcal{L}}_0(t-t_n)}\,\hat{\mathcal{J}}_e\, e^{\hat{\mathcal{L}}_0(t_n-t_{n-1})}\,\hat{\mathcal{J}}_e\cdots\hat{\mathcal{J}}_e\, e^{\hat{\mathcal{L}}_0(t_2-t_1)}\,\hat{\mathcal{J}}_e\, e^{\hat{\mathcal{L}}_0 t_1}\,\hat{\rho}_{in}\,. \tag{4.22}$$

The normalized conditioned-density matrix is then given by

$$\hat{\rho}^c_{norm} = \frac{\hat{\mathcal{J}}_e\, e^{\hat{\mathcal{L}}_0\tau}\,\hat{\rho}(0)}{W(\tau)}\,, \quad \text{where } \hat{\rho}(0) = |n,g\rangle\langle n,g|. \tag{4.23}$$

Here $W(\tau)$ is the normalizing factor and is also known as the waiting time distribution, which is given by

$$W(\tau) = \Gamma_e\,\mathrm{Tr}[\hat{s}_e\,\hat{\varrho}(\tau)\,\hat{s}^{\dagger}_e]\,, \quad \text{and } \tfrac{d\hat{\varrho}}{dt} = \hat{\mathcal{L}}_0[\hat{\varrho}(t)] \text{ with } \hat{\varrho}(0) = \hat{\rho}(0). \tag{4.24}$$

With this definition of waiting time distribution, we are now ready to compute the average switching rate of the JJ, which is given by

$$\left\langle \frac{1}{\tau} \right\rangle = \int_0^{\infty} \frac{1}{\tau}\, W(\tau) d\tau\,. \tag{4.25}$$

The average power absorbed by the detector can now be defined in terms of the switching rate in the following way:

$$P_{abs} = \hbar\,\omega_{eg}\left\langle \frac{1}{\tau} \right\rangle. \tag{4.26}$$

Here ω_{eg} is the frequency of the photon absorbed by the detector, which is equal to the characteristic frequency of the JJ.

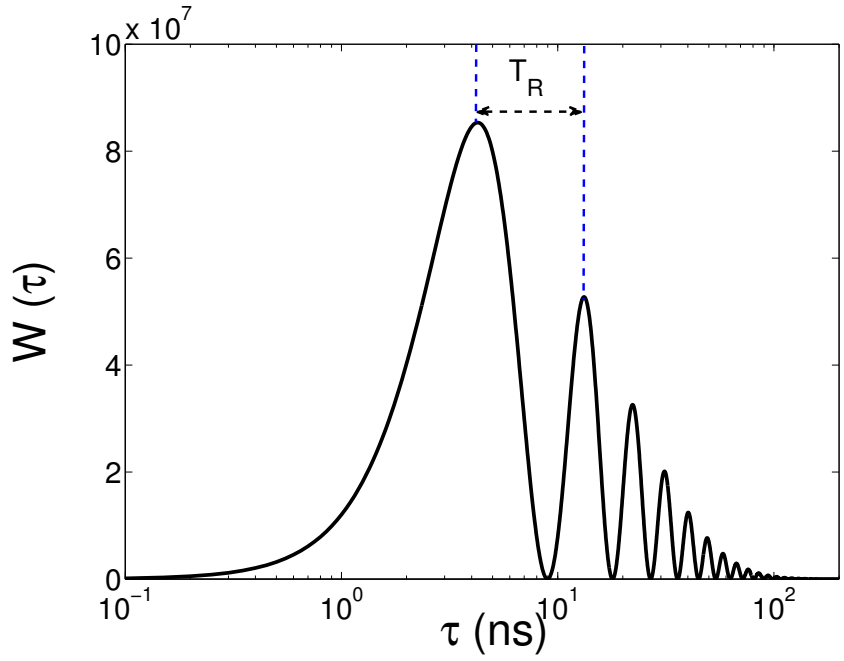

Figure 4.7: Waiting time distribution of a microwave driven resonator for $\langle n \rangle = 5$, $\Omega/2\pi = 50$ MHz, $\gamma = 0$.

Waiting time distribution

Below we compute and briefly discuss the waiting time distribution for two different detection schemes shown in the circuit diagrams above. The system Hamiltonian for Fig. [4.6] (a) is given by

$$\hat{H}_{sys} = \hbar\Delta_{eg}\hat{\Pi}_e + \frac{\hbar f}{2}(\hat{\sigma}_+ + \hat{\sigma}_-)\,, \tag{4.27}$$

where $\Delta_{eg} \equiv |\omega_d - \omega_{eg}|$ is the detuning between the drive frequency ω_d and the JJ's characteristic frequency ω_{eg}. $\hat{\Pi}_e$ is the projection operator for the excited state of the junction, $\hat{\Pi}_e = |e\rangle\langle e|$, and f is the drive amplitude. We choose to write $f = \sqrt{\langle n \rangle}\Omega$, anticipating its connection with an alternative detection scheme based on a microwave driven resonator, in which case $\langle n \rangle$ is the average number of photons in the resonator and Ω is vacuum Rabi frequency. However, for a JJ driven by a classical microwave source with drive amplitude f, the quantity f also characterizes the Rabi frequency.

In Fig. 4.7, we plot the waiting time distribution of a microwave driven JJ. Here we

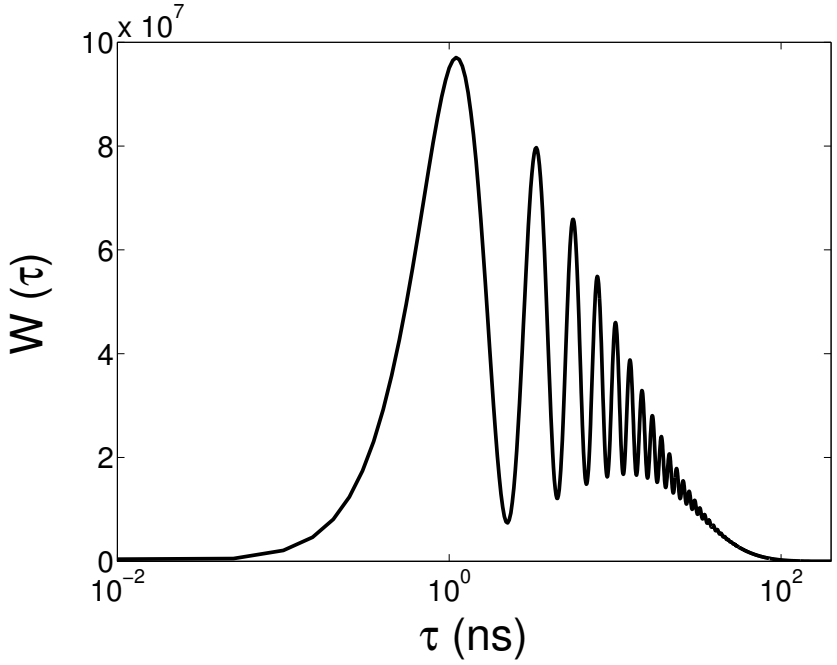

Figure 4.8: Waiting time distribution of a microwave driven resonator for $\langle n\rangle = 5$, $\Omega/2\pi =$ 200 MHz, $\gamma = 100$ MHz.

take $\langle n\rangle = 5, \Omega/2\pi = 50$ MHz and relaxation rate in the junction $\gamma = 0$ and $\Gamma_e = 7.3 \times 10^7$ s^{-1}. The first peak on the waiting time distribution always occurs at half the Rabi period, which is given by $T_R = 2\pi/f$ and the subsequent peaks are separated by a full Rabi period. This is due to the fact that the junction is most likely to switch when it reaches the excited state and it only takes half the Rabi period to reach the excited state for the first time, but a full Rabi period in all future times. The number of peaks that appear on the waiting time distribution are characteristics of the Rabi frequency. In addition, for non-zero γ, these peaks are not well resolved, as shown in Fig. 4.8. In this figure, $\gamma = 100$ MHz and $\Omega/2\pi = 200$ MHz.

Next, we consider the waiting time distribution for a microwave driven resonator connected to a JJ. Here the system Hamiltonian is given by

$$\hat{H}_{sys} = \frac{\hbar f}{2}(\hat{a} + \hat{a}^\dagger) + \hbar\Delta_r(\hat{a}^\dagger\hat{a} + \frac{1}{2}) + \hbar\Delta_{eg}\hat{\Pi}_e + \frac{\hbar\Omega}{2}(\hat{a}^\dagger\,\hat{\sigma}_- + \hat{a}\,\sigma_+)\,, \tag{4.28}$$

where the detuning $\Delta_r = |\omega_d - \omega_r|$, ω_r is the resonance frequency of the resonator and Ω is vacuum Rabi frequency. The drive amplitude f is given by $f = \sqrt{\langle n\rangle(4\Delta_r^2 + \kappa^2)}$, where κ

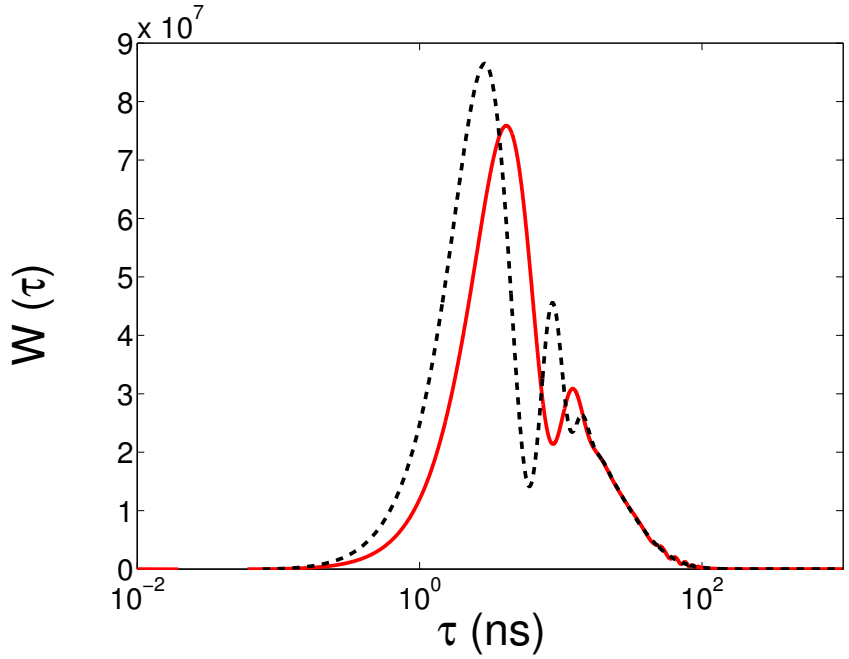

Figure 4.9: Waiting time distribution of a microwave driven resonator connected to a JJ for two different input powers: $\langle n \rangle = 5$ (solid red line) and $\langle n \rangle = 11$ (dashed black line). Other parameters are $\Omega/2\pi = 50$ MHz, $\gamma = 0$ and $\kappa = 1$ MHz.

is the inverse lifetime of photons in the resonator.

In Fig. 4.9, we plot the waiting time distribution of a microwave driven resonator connected to a JJ for two different input powers of the drive. We find that the waiting time distribution for this detection scheme is very different from that of a microwave driven JJ. For a coherent state in the resonator, we notice a far fewer oscillatory peaks on $W(\tau)$. This is due to the beating between the Rabi oscillations with different frequencies, which is caused due to different number of photons in the resonator.

Next, we compute the average switching rate of the detector. As shown in the previous section, the average switching rate is given by

$$\left\langle \frac{1}{\tau} \right\rangle = \int_0^\infty d\tau \, W(\tau) = \int_0^\infty d\tau \frac{\Gamma_e}{\tau} \, \mathrm{Tr} \left[\hat{s}_e \, e^{\hat{\mathcal{L}}_0 \tau} \, \hat{\varrho}(0) \, \hat{s}_e^\dagger \right] . \tag{4.29}$$

We numerically diagonalize $\hat{\mathcal{L}}_0$ and obtain the eigenvalues and eigenvectors, which can be written compactly as

$$\mathbf{D} \, \hat{\mathcal{L}}_0 \, \mathbf{D}^{-1} = \mathbf{\Lambda} \, , \tag{4.30}$$

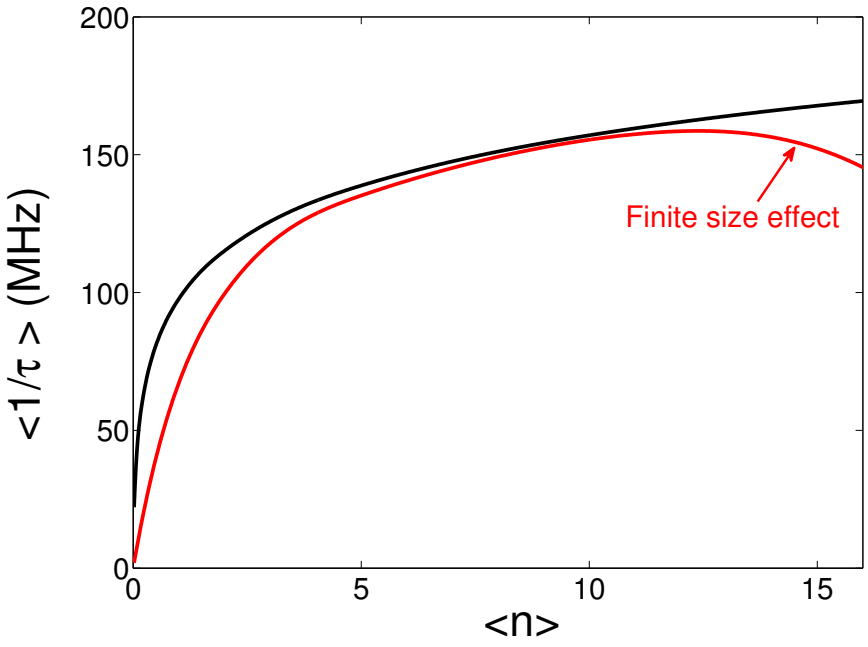

Figure 4.10: Average switching rates for two different detection schemes: a microwave driven resonator connected to a JJ (red solid line) and a microwave driven JJ (solid black line). Here $\Omega/2\pi = 50$ MHz, $\gamma = 0$ and $\kappa = 1$ MHz.

where $\mathbf{D}$ is the matrix of eigenvectors and $\mathbf{\Lambda}$ is the diagonal matrix of eigenvalues of $\hat{\mathcal{L}}_0$. If we plug this into the expression for switching rate, we obtain

$$\left\langle \frac{1}{\tau} \right\rangle = \Gamma_e \ \mathrm{Tr}\left[\hat{s}_e \, \mathbf{D} \left(\int_0^\infty \frac{e^{\mathbf{\Lambda}\tau}}{\tau} \, d\tau \right) \mathbf{D}^{-1} \, \hat{\varrho}(0) \, \hat{s}_e^\dagger \right]. \tag{4.31}$$

Since $\mathbf{D}\,\mathbf{D}^{-1} = \mathbf{I}$, $\mathrm{Tr}\left[\hat{s}_e \, \mathbf{D}\,\mathbf{D}^{-1} \, \hat{\varrho}(0) \, \hat{s}_e^\dagger\right] = \mathrm{Tr}\left[\hat{s}_e \, \hat{\varrho}(0) \, \hat{s}_e^\dagger\right]$, which is precisely 0. We can therefore introduce an exponent of an arbitrary complex number λ with a *negative* real part in the time integrand, which allows us to perform the time integration analytically:

$$\int_0^\infty \frac{\tau(e^{\mathbf{\Lambda}\tau} - e^{\lambda\tau})}{\tau^2} \, d\tau = -\log[-\mathbf{\Lambda}] + \log[-\lambda], \quad \text{where} \quad \mathrm{Re}[\mathbf{\Lambda}, \lambda] < 0 \,.$$

In Fig. 4.10, we plot the average switching rates for two different detection schemes. We find that average switching rates for these detection schemes coincide as we increase the number of photons in the resonator, as expected. The deviation in the switching rate from the expected value for a large photon numbers is simply a numerical artifact due to truncation of the full Hilbert space.

4.7 Discussion

In conclusion, we have presented a model to determine the quantum efficiency of a microwave photon detector based on a current-biased JJ. We have demonstrated that the efficiency to detect a single photon loaded in a cavity has maximal value $\Gamma_e/(\Gamma_e + \gamma)$. We have also determined that the bandwidth of the detector is characterized by the sum of the vacuum Rabi frequency and the broadening of the first excited state of the JJ due to tunneling and relaxation processes. Our simulations indicate that for currently used JJ photon detectors, the quantum efficiency is about 50% for the bias point $\Delta U/\hbar\omega_p = 2$ and about 85% for $\Delta U/\hbar\omega_p = 1.7$. We have finally investigated the probability to detect a photon in the case of a multiphoton initial resonator state and have found that the detection efficiency quickly approaches 100% as the initial number of photons increases, consistent with previous studies [93, 91] of a continuous flux of photons incident on the detector.

We also considered alternative photon detection schemes and studied several issues that are of importance for analyzing the efficiency of the detector based on such schemes. First, we derived a condition to minimize the power reflected by the photon detector. We then presented a rigorous method to accurately compute the power absorbed by the detector.

Chapter 5

Effect of decoherence on the Berry curvature

5.1 Introduction

Quantum computation based on geometric phases is another emerging paradigm that has become increasingly popular due to its resilience against errors. Geometric phases emerge naturally in quantum mechanics during the adiabatic evolution of the quantum mechanical state for instance, the Berry phase [106]. Since the Berry phase depends on the evolution path and not on the detailed dynamics, which suggests an inherent fault tolerance, it can be a useful resource for quantum computation [107]. The past measurement technique of the Berry phase in superconducting circuits was based on an interference experiment wherein the drive parameter was changed adiabatically [29]. A recent approach towards the detection of the Berry curvature (and hence the Berry phase) relies on the dynamical response of the generalized force to quench velocity of the generalized displacement [30]. This approach is more feasible than previous approaches since it does not require a strict adiabatic condition, which is hard to achieve in generic experimental settings. Although quantum computation based on geometric phases is robust against error, the entanglement of the qubit system with its environment makes it difficult to separate the geometric and

dynamical contributions to quantum gates. Thus, it is necessary to analyze the behavior of the Berry phase and curvature in the presence of decoherence. Here we present results for the Berry curvature measurement in the presence of decoherence using density matrix formalism within linear response theory. We also study the effect of the third level on the measurement of the Berry curvature in phase or transmon qubits.

5.2 Berry phase and curvature

The Berry phase is defined as the phase accumulated by the wave function during the adiabatic evolution around a closed path in a parameter space defined by $\vec{I}(t)$. This geometric phase γ_B can also be obtained by integrating the Berry connection $\vec{A}$, which is analogous to a vector potential in the parameter space, along a closed path $\mathcal{P}$:

$$\gamma_B = \oint_{\mathcal{P}} \vec{A} \cdot d\vec{l}, \quad \text{where} \tag{5.1}$$

$$\vec{A} = i\Big\langle \Psi(\vec{I})|\nabla|\Psi(\vec{I})\Big\rangle \quad \text{and} \quad \nabla \equiv (\partial_{I_x}, \partial_{I_y}, \partial_{I_z})\,. \tag{5.2}$$

The curl of the Berry connection then gives the Berry curvature, which can be thought of as a magnetic field in the parameter space:

$$F_{\mu\,\nu} = \partial_\mu A_\nu - \partial_\nu A_\mu\,, \quad \text{where } \partial_\mu \equiv \partial_{I_x,\,I_y,\,I_z}\,. \tag{5.3}$$

From the Stoke's theorem, it then follows that the Berry phase is given by integrating the Berry curvature over an area enclosed by the closed path, namely

$$\gamma_B = \oint_{\mathcal{P}} \vec{A} \cdot d\vec{l} = \int_{\mathcal{S}} F_{\mu\,\nu}\, d\mu\, d\nu\,. \tag{5.4}$$

One can also show that the Berry curvature is directly related to the geometric tensor χ, also known as Fubini's metric on quantum rays, which is often used to describe the manifolds of adiabatically connected wave functions $\Psi(\vec{I})$ [108]:

$$\chi_{\mu\,\nu} = \Big\langle \partial_\mu \Psi(\vec{I})\big|\partial_\nu \Psi(\vec{I})\Big\rangle - \Big\langle \partial_\mu \Psi(\vec{I})\big|\Psi(\vec{I})\Big\rangle\Big\langle \Psi(\vec{I})\big|\partial_\nu \Psi(\vec{I})\Big\rangle\,. \tag{5.5}$$

It is straightforward to show that $F_{\mu\,\nu} = -2\,\mathrm{Im}\,\chi_{\mu\,\nu}$. In this chapter we will only focus on the Berry phase or curvature of the ground state Ψ_g of the system Hamiltonian $\hat{H}(\vec{I})$, for which the geometric tensor can be written as

$$\chi^{g}_{\mu\,\nu} = \sum_{n\neq g} \frac{\left\langle \Psi_g(\vec{I})\middle|\partial_\mu \hat{H}\middle|\Psi_n(\vec{I})\right\rangle\left\langle \Psi_n(\vec{I})\middle|\partial_\nu \hat{H}\middle|\Psi_g(\vec{I})\right\rangle}{(E_g - E_n)^2}\,. \tag{5.6}$$

Here E_n is the energy eigenvalue of the n^{th} eigenstate Ψ_n of the Hamiltonian $\hat{H}(\vec{I})$. We use this formula to compute the analytical Berry curvature for two-level and three-level systems. We note that the drive field $\vec{I}(t)$ corresponds to the magnetic field in case of a spin qubit and to the microwave drive in other solid-state charge qubits.

5.3 Berry curvature in a two-level system

The Hamiltonian of a spin-1/2 particle in the magnetic field $\vec{I}$ is given by :

$$\hat{H}(t) = -\frac{\hbar\Delta}{2}\vec{\hat{\sigma}}\cdot\vec{I}(t)\,, \tag{5.7}$$

where $\vec{I}(t) = (I_x(t), I_y(t), I_z(t))$ is a dimensionless field amplitude with $I_z(t) \equiv 1$ and Larmor frequency Δ. For a non-zero magnetic field along the x-direction and a zero field along the y-direction, we can write the Hamiltonian as

$$\hat{H}(t) = -\frac{\hbar\Delta}{2}\left(\hat{\sigma}_z + \hat{\sigma}_x\, I_x(t)\right). \tag{5.8}$$

The x-component of the magnetic field drive is set to 0 at $t = 0$, which is then ramped quadratically with time while the y-component of the field is set to zero at all time, i.e., $I_x(t) = 1/2\, v_x^2\, t^2$ with $I_x(T) = 0.5$ or any other value, and $I_y(t) = 0$. Here v_x is the ramp velocity of the x-component of the field at the end of the drive or sweep time T. This quadratic protocol is slightly different from the linear quenching of the x-component of the drive proposed in Ref. [30], where the quench velocity is held at a constant value. However, for the quadratic protocol, the ramp velocity need not be held constant, a convenience that makes this protocol more attractive experimentally.

The response of the system to changing magnetic field drive in x-direction is obtained by calculating the y-component of the magnetization ($m_y = \langle\sigma_y\rangle/2$) for different ramp velocities v_x. Within the linear response regime, the slope of the curve $m_y(v_x)$ determines the Berry curvature of the system [30]. The qubit is first prepared in the ground state of the Hamiltonian $H(t)$ at $t = 0$. Subsequently, the x-component of the drive is ramped quadratically with time. After time $t = T$, the y-component of the magnetization is computed from the density matrix as $m_y(T) = \mathrm{Tr}[\hat{\sigma}\,\hat{\rho}(T)]/2 = \mathrm{Im}\,\hat{\rho}(T)$.

Results

In order to calculate the magnetization, we first need to compute the time evolution of density matrix of the qubit. First, we consider the evolution of the system in the absence of environment and study the effect of decoherence later. The density matrix equation in this case is simply:

$$\frac{d\hat{\rho}(t)}{dt} = \frac{1}{i\,\hbar}\Big[\hat{H}(t), \hat{\rho}(t)\Big]\,. \tag{5.9}$$

We perform a transformation (rotation) of the two level system that follows the eigenstate basis, which we refer to as "adiabatic frame". When the field is in $x-z$ plane, we can write the unitary transformation as

$$\hat{H}^U(t) = \mathcal{U}(t)\,\hat{H}(t)\,\hat{\mathcal{U}}^\dagger(t) - i\hbar\,\hat{\mathcal{U}}(t)\,\frac{d\hat{\mathcal{U}}^\dagger(t)}{dt}\,,\ \text{ where } \hat{\mathcal{U}}(t) = \exp[i\,\theta(t)\,\hat{\sigma}_y/2]\,, \tag{5.10}$$

and $\theta(t) = \arctan(I_x(t)/I_z)$ is the angle formed by the the x-component of the drive with respect to the z-direction. In this basis, the Hamiltonian $\hat{H}^U$ is given by

$$\begin{aligned}\hat{H}^U(t) &= -\frac{\hbar\Delta}{2}\,I(t)\,\hat{\sigma}_z + \hat{\mathcal{N}}(t)\,, \quad \text{where}\\ \hat{\mathcal{N}}(t) &\equiv -\frac{\hbar\Delta}{2}\,\dot{\theta}(t)\,\hat{\sigma}_y = -\frac{\hbar\Delta}{2}\left(\frac{I_z}{(I_z^2 + I_x^2(t))}\frac{dI_x(t)}{dt}\sigma_y\right).\end{aligned} \tag{5.11}$$

The form of the equation of motion of the density matrix in the adiabatic frame remains unchanged and is given by

$$\frac{d\hat{\rho}^U(t)}{dt} = \frac{1}{i\hbar}\Big[\hat{H}^U(t)\,, \hat{\rho}^U(t)\Big]\,. \tag{5.12}$$

Due to non-linear time-dependent nature of the rotation operator $\hat{\mathcal{U}}$, the Hamiltonian picks up an additional term $\hat{\mathcal{N}}(t)$ in the adiabatic frame. This term is negligibly small only in the adiabatic limit, that is, when $\dot{\theta} \ll I(t)$. From this new expression for the Hamiltonian, it is easy to see that the y-component of the magnetization is given by

$$\langle \hat{\sigma}_y(t) \rangle \equiv \mathrm{Tr}\left[\hat{\rho}^U(t)\,\hat{\sigma}_y\right] = \left[\frac{I_z}{2\,I^3(t)}\right]\frac{dI_x(t)}{dt}\,, \tag{5.13}$$

and the Berry curvature $F_{x\,y}$ is given by the quantity inside the bracket evaluated at the end of the drive time T, i.e., $F_{x\,y} = I_z/2I^3(T)$.

We now proceed to calculate the Berry phase by integrating the Berry curvature evaluated at each point on a circular disk of radius $I_\rho(t)$ located I_z above the $x-y$ plane in the parameter space defined by $\vec{I}(t)$:

$$\gamma_B = \int_s F_{x\,y}\,dx\,dy = \int_0^{2\pi} d\phi \int_0^{I_\rho(t)} d\eta\,\frac{\eta\,I_z}{2\,(I_z^2+\eta^2(t))^{3/2}} = \pi\left(1-\frac{I_z}{I(t)}\right), \tag{5.14}$$

where $I_\rho(t)$ is the radial component of the field, that is, $I_\rho(t) = \sqrt{I_x^2(t)+I_y^2(t)}$. This expression for the Berry phase is identical to a well known expression obtained from the adiabatic measurement protocol [29, 109, 110], that is, $\gamma_B = \pi(1-\cos(\alpha))$, where α is the angle between $\vec{I}(t)$ and the z-axis in the parameter space and is given by $\alpha = \tan^{-1}(I_\rho(t)/I_z)$. Hence, γ_B can be viewed as the solid angle subtended by the circular disk of radius I_ρ at the origin in the parameter space.

The Berry curvature measurement discussed above requires measurement of the magnetization in the y-direction. However, experimentally, it is much more convenient to measure the expectation value of $\langle \hat{\sigma}_z \rangle$. Therefore, we also consider the Berry curvature measurement by first measuring the $\langle \hat{\sigma}_z \rangle$. In order to achieve this, we let the qubit or spin to freely precess for time τ in the presence of a constant magnetic field by turning off the velocity. We then measure the difference between the maximum and minimum values of $\langle \hat{\sigma}_z(\tau) \rangle$ for each ramp velocity and extract the Berry curvature. We find that the following relation holds true:

$$\delta\langle \hat{\sigma}_z \rangle \equiv \frac{1}{2}\Big[\max(\langle \hat{\sigma}_z(\tau)\rangle) - \min(\langle \hat{\sigma}_z(\tau)\rangle)\Big] = \frac{\sin\theta\,I_z}{2\,I^3(t)}\,\frac{dI_x(t)}{dt}\,. \tag{5.15}$$

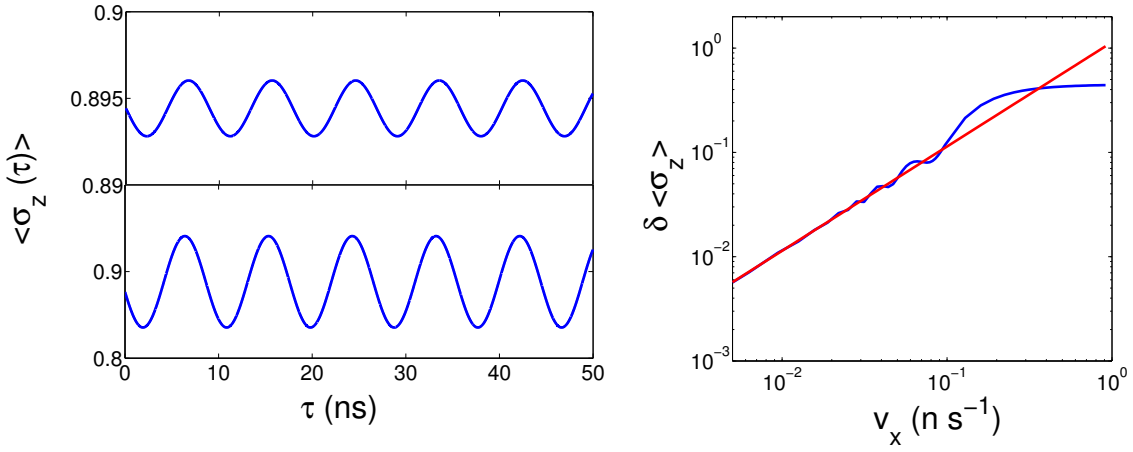

Figure 5.1: The left panel is a free precession of $\langle\hat{\sigma}_z\rangle$ for two different ramp velocities: $v_x = 0.00314$ ns^{-1} (top) and $v_x = 0.0974$ ns^{-1} (bottom). The right panel is the difference between the maximum and minimum of $\langle\hat{\sigma}_z(\tau)\rangle$ vs. the ramp velocity v_x of a quadratic drive with detuning $\Delta/2\pi = 100$ MHz: analytical result without decoherence (red solid line), and a full numerical solution (blue solid line) of the density matrix equation without decoherence.

On the left panel of Fig. 5.1, we plot the time evolution of $\langle\hat{\sigma}_z(\tau)\rangle$ for various ramp velocities. On the right panel, we plot the difference between the maximum and minimum of those oscillations and find excellent agreement between the numerical and analytical results. Using Eq. 5.15, the Berry curvature can then be extracted from the slope of this line.

Decoherence

Next we consider the effect of decoherence on the Berry curvature. We can naturally introduce pure dephasing and relaxation mechanisms with the Lindblad superoperator in the eigenbasis frame where the system Hamiltonian is diagonal. The adiabatic frame is not suitable for this purpose since the Hamiltonian $\hat{H}^U$ in this frame is not truly diagonal. We note that the adiabatic frame would be a true eigenbasis frame if $\dot{\theta} \ll I(t)$. However, this is not applicable in our case where $\dot{\theta}/I(t) \lesssim 1$. Therefore, we perform an additional transformation such that the final Hamiltonian is truly diagonal or approximately diagonal with error roughly $\mathcal{O}\Big(\Big(\frac{\dot{\theta}(t)}{I(t)}\Big)^2\Big)$ or $\mathcal{O}\Big(\ddot{\theta}(t)\Big)$, which we assume to be negligibly small. The

unitary transformation is given by:

$$\hat{H}^D(t) = \hat{\mathcal{D}}(t)\,\hat{H^U}(t)\,\hat{\mathcal{D}}^\dagger(t) - i\hbar\,\hat{\mathcal{D}}(t)\,\frac{d\,\hat{\mathcal{D}}^\dagger(t)}{dt}\,,\ \text{ where } \hat{\mathcal{D}}(t) = \exp[-i\,\beta(t)\,\hat{\sigma}_x/2]\,, \quad (5.16)$$

and $\beta(t) = \arctan(\dot{\theta}(t)/I(t))$ is the angle of the x-component of the drive with respect to the z-direction in the adiabatic frame. After the transformation, the Hamiltonian $\hat{H}^D$ becomes

$$\hat{H}^D(t) = -\frac{\hbar\Delta}{2}\sqrt{I^2(t) + \dot{\theta}^2(t)}\,\hat{\sigma}_z + \hat{\mathcal{Q}}(t)\,, \quad (5.17)$$

where the "drag term" $\hat{\mathcal{Q}}(t)$ is given by

$$\hat{\mathcal{Q}}(t) \equiv \frac{\hbar\Delta}{2}\,\dot{\beta}(t)\,\hat{\sigma}_x \quad \text{and} \quad \dot{\beta}(t) = \frac{\left[I_z\,I(t)\,\frac{\partial^2 I_x(t)}{\partial t^2} - I_z\left(\frac{\partial I_x(t)}{\partial t}\right)^2\right]}{\left[I^2(t) + I_z^2\left(\frac{\partial I_x(t)}{\partial t}\right)^2\right]}\,. \quad (5.18)$$

Due to non-linear time-dependent nature of the rotation operator $\hat{\mathcal{D}}(t)$, the Hamiltonian picks up an additional term $\hat{\mathcal{Q}}(t)$, which is negligibly small. However, for the sake of clarity, we choose the following sinusoidal drive

$$I_x(t) = I\sin(\theta(t)) \text{ and } I_z(t) = I\cos(\theta(t)) \quad (5.19)$$

for which the rotation operator $\hat{\mathcal{D}}$ is truly time independent:

$$\hat{\mathcal{D}} = \exp\Big[-i\,\arctan(\Omega/I)\,\sigma_x/2\Big]\,. \quad (5.20)$$

Here $\theta = \Omega\,t$ and I is the amplitude of the sinusoidal drive, which, unlike in the case of a quadratic drive, is time-independent. Consequently, $\dot{\beta}(t) = 0$ and the Hamiltonian becomes truly diagonal. In the eigenbasis frame, the evolution of the density matrix of the qubit coupled to its environment is governed by the following master equation, which is characterized by a phenomenological decay rate γ ($T_1 = 1/\gamma$) and a pure dephasing rate γ_ϕ ($T_\phi = 1/\gamma_\phi$) for the qubit:

$$\begin{aligned}
\frac{d\hat{\rho}^D(t)}{dt} &= \frac{1}{i\hbar}\Big[\hat{H}^D(t)\,,\hat{\rho}^D(t)\Big] + \hat{\mathcal{L}}_\gamma[\hat{\rho}^D(t)] + \hat{\mathcal{L}}_{\gamma_\phi}[\hat{\rho}^D(t)]\,, \quad \text{where} \\
\hat{\mathcal{L}}_\gamma[\hat{\rho}^D(t)] &= \gamma\left(\hat{\sigma}_-\hat{\rho}^D\hat{\sigma}_+ - \frac{1}{2}\{\hat{\sigma}_+\hat{\sigma}_-,\hat{\rho}^D\}\right) \quad \text{and} \\
\hat{\mathcal{L}}_{\gamma_\phi}[\hat{\rho}^D(t)] &= \gamma_\phi\left(\hat{\Pi}_0\,\hat{\rho}^D\,\hat{\Pi}_0^\dagger - \frac{1}{2}\{\hat{\Pi}_0^\dagger\,\hat{\Pi}_0,\hat{\rho}^D\}\right)\,, \text{with } \hat{\Pi}_0 = |0\rangle\langle 0|\,.
\end{aligned} \quad (5.21)$$

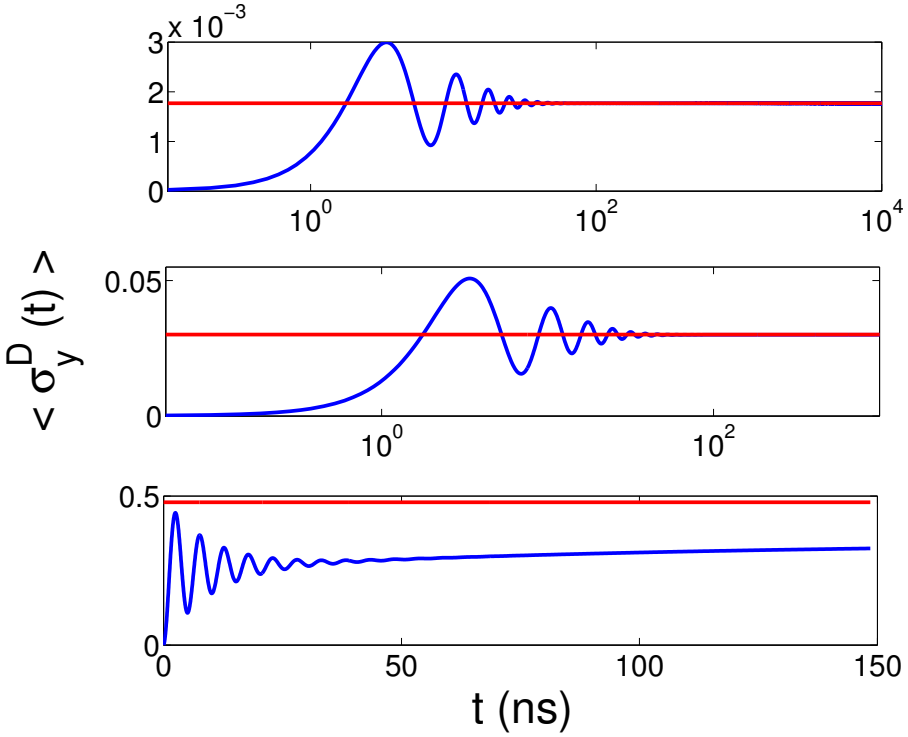

Figure 5.2: Magnetization $\langle \hat{\sigma}_y^D(t) \rangle$ in the eigenbasis frame *vs*. drive time (t) for a sinusoidal drive with detuning $\Delta/2\pi = 100\,\text{MHz}$ and amplitude $I = \sqrt{2}$: analytical magnetization at the end of the drive time T in the absence of decoherence (red solid line) and a full numerical solution (blue solid line) of the density matrix equation in the presence of decoherence with rates $\gamma = 1 \times 10^7\,\text{s}^{-1}$ and $\gamma_\phi = 1 \times 10^8\ \text{s}^{-1}$. Here three panels correspond to three different drive velocities $\Omega = 0.00314\ \text{ns}^{-1}$ (top), $0.053407\,\text{ns}^{-1}$ (middle), and $0.8513\,\text{ns}^{-1}$ (bottom).

We fist investigate the dynamics of the magnetization for several decoherence parameters. The y-component of the magnetization in the eigenbasis frame is given by

$$\langle \hat{\sigma}_y^D(t) \rangle \equiv \text{Tr}\left[\hat{\rho}^D(t)\,\hat{\mathcal{D}}\,\hat{\sigma}_y\,\hat{\mathcal{D}}\right] \tag{5.22}$$

In Fig. 5.2, we plot the y-component of the magnetization in the eigenbasis frame as a function of time for three different velocities of the sinusoidal drive. Here we choose the amplitude of the drive to be $I = \sqrt{2}$ and the angle between the x-component of the drive at the end of the drive and z-axis to be $\theta(T) = \pi/4$. For our choice of pure dephasing and relaxation times of 10 ns and 100 ns, respectively, we observe rapid oscillations in magnetization at timescales shorter than the pure dephasing time. Dephasing essentially

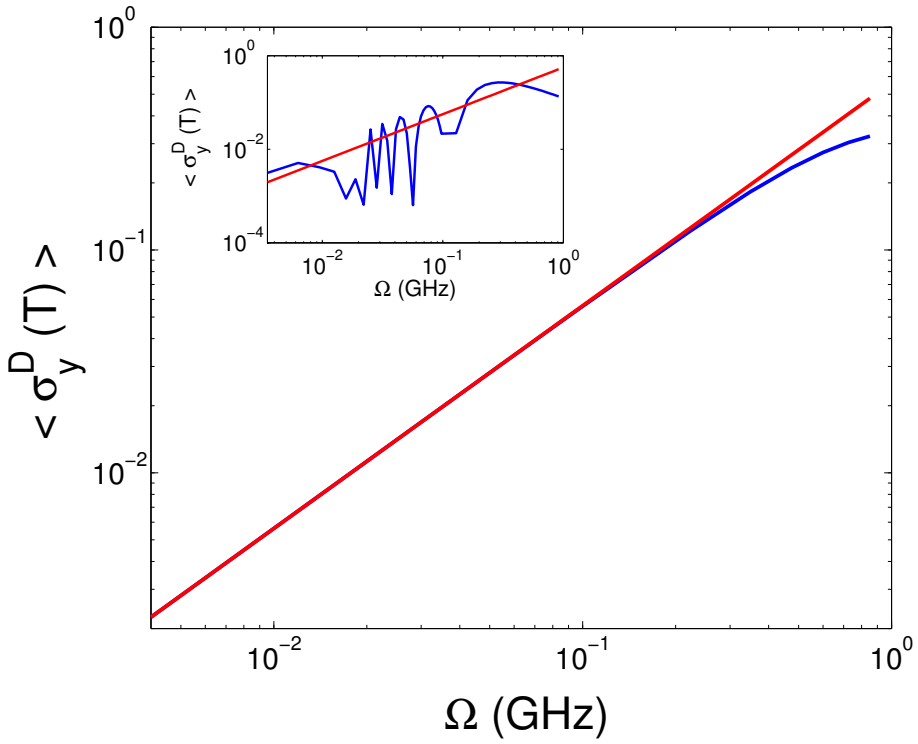

Figure 5.3: Magnetization $\langle \hat{\sigma}_y^D(T) \rangle$ in the eigenbasis frame *vs.* the angular velocity Ω of a sinusoidal drive with detuning $\Delta/2\pi = 100\,\text{MHz}$ and amplitude $I = \sqrt{2}$: analytical result at the end of the drive time T in the absence of decoherence (red solid line) and a full numerical solution (blue solid line) of the density matrix equation in the presence of decoherence with rates $\gamma = 1 \times 10^7\,\text{s}^{-1}$ and $\gamma_\phi = 1 \times 10^8\ \text{s}^{-1}$. The plot in the inset is of the y-component of the magnetization in the absence of decoherence.

suppresses these oscillations as time progresses while the relaxation forces the spin to return to the ground state.

Next, we plot the y-component of the magnetization *vs.* the drive velocity of a sinusoidal drive in the eigenbasis frame, as shown in Fig. 5.3. Our numerical result indicates that decoherence has negligible effect on the magnetization and hence the Berry curvature. The inset in Fig. 5.3 displays the y-component of the magnetization in the absence of decoherence. Here we find that the response is not linear with respect to the drive velocity. Thus, we conclude that decoherence is essential for the linear response of the magnetization to the drive velocity, at least for a sinusoidal drive.

The effect of decoherence on the adiabatic response of a driven open quantum system was

also previously studied by Avron *et. al.* [111]. They considered the effect of pure dephasing on the Berry curvature in the adiabatic limit assuming that instantaneous stationary states move continuously with the control parameter. With this assumption, they introduced the Lindblad superoperator to take into account pure dephasing of the quantum system in the adiabatic frame. However, it is important to note that the system Hamiltonian is not truly diagonal in this frame. Nevertheless, it is possible to derive their result if we look for a steady state solution of the density matrix in the adiabatic frame, in the following form:

$$\begin{aligned} \hat{\rho}(t) &= \hat{\rho}_0 + \delta\hat{\rho}(t)\,, \quad \text{where} \\ \hat{\rho}_0 &= \frac{1}{2}(1-\hat{\sigma}_z) \quad \text{and} \\ \delta\hat{\rho}(t) &= A(t)\,\hat{\sigma}_z + B(t)\,\hat{\sigma}_y + C(t)\,\hat{\sigma}_z\,. \end{aligned} \tag{5.23}$$

Here A, B and C are unknown coefficients whose first time derivatives are zero. In order to simplify notations, here we dropped the superscript U and chose to use simply $\hat{\rho}$ to represent the density matrix in the adiabatic frame. We then plug the above ansatz into the master equation and compare coefficients to obtain the following set of equations:

$$\begin{aligned} \frac{\dot{\theta}}{2} - A\gamma_\phi - \frac{A\gamma}{2} + \hbar\Delta I(t)\,B - C\,\dot{\theta} &= 0 \\ -\hbar\Delta I(t)\,A - B\gamma_\phi - \frac{B\gamma}{2} &= 0 \\ A\dot{\theta} - \gamma(C-1) &= 0\,. \end{aligned} \tag{5.24}$$

We solve these equations for B and obtain the y-component of the magnetization:

$$\langle\hat{\sigma}_y\rangle \equiv \mathrm{Tr}[\hat{\rho}(t)\,\hat{\sigma}_y] = \left\{ \frac{\Delta^2\,I^2(t)}{[\Delta^2\,I^2(t) + (\gamma/2+\gamma_\phi)^2]}\;\frac{I_z}{2\,I^3(t)} \right\} \frac{dI_x(t)}{dt}\,. \tag{5.25}$$

From this, we can easily read off the Berry curvature, which is given by the quantity inside the curly bracket in the above expression. We find that the correction due to the decoherence on the Berry curvature of an ideal system is given by $\Delta^2\,I^2(t)/[\Delta^2\,I^2(t) + (\gamma/2+\gamma_\phi)^2]$, which is consistent with the result derived in Ref. [111] that used a different approach and only considered the effect of pure dephasing.

In Fig. 5.4, we plot the y-component of the magnetization for different ramp velocities of a quadratic drive $I_x(t) = v_x^2\,t^2/2$. We find excellent agreement between numerical and

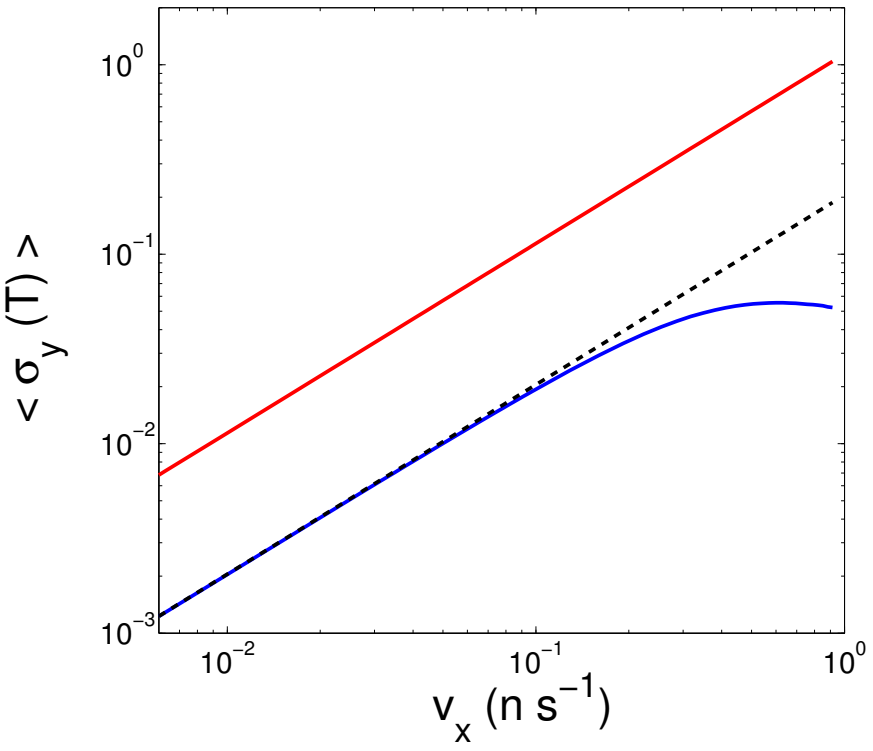

Figure 5.4: Magnetization $\langle\hat{\sigma}_y(T)\rangle$ vs. the ramp velocity v_x of a quadratic drive with detuning $\Delta/2\pi = 100$ MHz: analytical result in the absence of decoherence (red solid line), analytical result with the relaxation rate $\gamma = 1$ GHz and the pure dephasing rate $\gamma_\phi = 1$ GHz (black dashed line), and a full numerical solution (blue solid line) of the density matrix equation in the presence of decoherence.

analytical results in the presence of decoherence. Nonetheless, we believe that the effect of decoherence can be accurately described in the eigenbasis frame [112], where we discovered that decoherence does not hinder the curvature measurement, but instead assists in the linear response of the magnetization, in particular for the sinusoidal drive.

5.4 Berry curvature in superconducting qubits

In this section, we consider the Berry curvature measurement in superconducting qubits. In real qubits like phase or transmon, the presence of the third level cannot be ignored and its effect on the measurement of the Berry curvature should be carefully studied. Nonetheless, the results presented in the previous section is also applicable to a three-level system with

anharmonicity much larger than detuning. For definiteness, here we only consider a phase qubit. The Hamiltonian of a flux-biased phase qubit $\hat{H}_q$ is written in terms of operators $\hat{Q}$ and $\hat{\delta}$, the charge and phase difference of the JJ, respectively:

$$\hat{H}_q = \frac{\hat{Q}^2}{2C} + \frac{1}{2L}\left(\Phi_b - \frac{\Phi_0}{2\pi}\,\hat{\delta}\right)^2 - \frac{I_0\Phi_0}{2\pi}\,\cos\hat{\delta}\,, \tag{5.26}$$

where L (C) is loop inductance (junction capacitance), Φ_b is the external magnetic flux applied to the phase qubit, I_0 is the critical current of the JJ, and $\Phi_0 = h/2e$ is the flux quantum. The qubit is capacitively coupled to a microwave current source, which is used to drive the qubit. This coupling introduces a time-dependent part in the qubit Hamiltonian:

$$\hat{P}(t) = \frac{\Phi_0 I(t)}{2\pi}\hat{\delta}\,. \tag{5.27}$$

Here $I(t) = I_x(t)\cos\omega_d t + I_y(t)\sin\omega_d t$ is the microwave current with frequency ω_d. Total Hamiltonian of the driven qubit is then given by $\hat{H}(t) = \hat{H}_q + \hat{P}(t)$. We truncate the qubit Hamiltonian Eq. 5.26, along with the time-dependent term Eq. 5.27, to three localized levels and obtain the following Hamiltonian:

$$\hat{H}(t) = \hbar\sum_{j=1}^{2}\left[\omega_{j-1}\hat{\Pi}_j + a(t)\lambda_j\hat{\sigma}_j^+ + a(t)^*\lambda_j\hat{\sigma}_j^-\right] + \hat{H}_{nr}\,, \tag{5.28}$$

where $\hat{\Pi}_j = |j\rangle\langle j|$ is the projector for the j^{th} level, $\hat{\sigma}_j^+ = |j\rangle\langle j-1|$ is the raising operator, $a(t) = (I_x(t) - iI_y(t))e^{i\omega_d t}/2$ is the amplitude of microwave drive, $\lambda_j = \Phi_0\langle j|\hat{\delta}|j-1\rangle/2\pi\hbar$ is the matrix element of the phase operator, $\omega_j = (\varepsilon_{j+1} - \varepsilon_0)/\hbar$, ε_j is an energy eigenvalue of time-independent Hamiltonian and $\hat{H}_{nr}$ contains non-resonant terms, which we neglect.

We transform the Hamiltonian Eq. 5.28 to a frame rotating with frequency ω_d with respect to the laboratory frame and obtain:

$$\hat{H}^R(t) = \hbar\sum_{j=1}^{2}\left[\Delta_j\hat{\Pi}_j + \frac{I_x(t)}{2}\lambda_j\hat{\sigma}^x_{j-1,j} + \frac{I_y(t)}{2}\lambda_j\hat{\sigma}^y_{j-1,j}\right], \tag{5.29}$$

where detuning $\Delta_1 = \Delta = \omega_0 - \omega_d$, $\Delta_2 = \delta_{an} + 2\,\Delta$, and the anharmonicity parameter $\delta_{an} \equiv \omega_1 - 2\,\omega_0$. We define operators $\hat{\sigma}^x_{j,k} = |k\rangle\langle j| + |j\rangle\langle k|$ and $\hat{\sigma}^y_{j,k} = i|k\rangle\langle j| - i|j\rangle\langle k|$.

We consider a setup where the drive current $I_x(t)$ increases quadratically with time. Here $I_x(t) = v_x^2\,t^2/2$ and we require that $I_x(T) = 0.5$. The y-quadrature drive $I_y(t)$ is set to zero at all times.

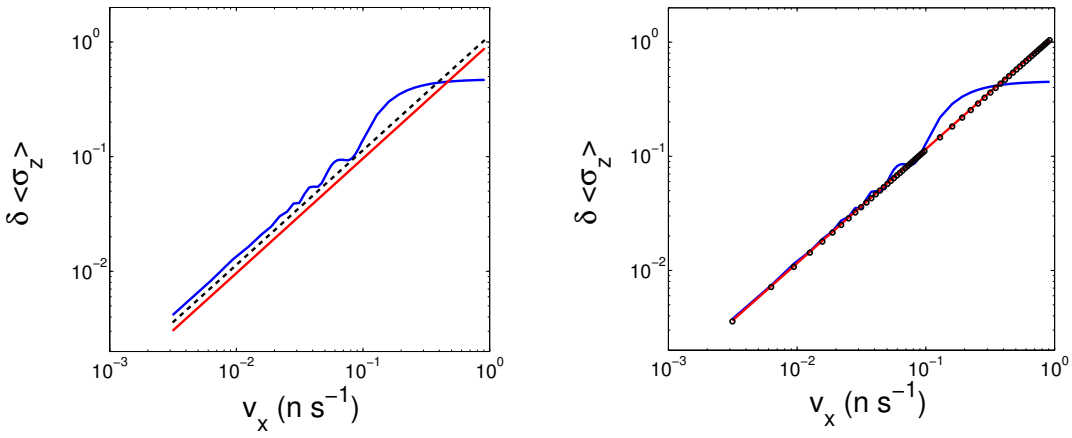

Figure 5.5: The difference between the maximum and minimum of $\langle\hat{\sigma}_z(\tau)\rangle$ *vs.* the ramp velocity v_x of a quadratic drive with detuning $\Delta/2\pi = 100$ MHz and anharmonicity $\delta_{an}/2\pi = 200$ MHz (left panel) and 1000 MHz (right panel). The solid blue line is the result obtained for a three-level system from a full numerical solution of the density matrix equation, the solid red line is the analytical result for a strictly three-level system, and the black dashed line on the left panel and black circles on the right panel correspond to the analytical result for a strictly two-level system.

Results

For a three-level system, it is convenient experimentally to perform a direct measurement of $\langle\hat{\sigma}_z\rangle$ instead of the y-component of the magnetization, in part due to difficulty in performing $\pi/2$-rotation in the presence of the third level. For the sake of simplicity, we do not consider decoherence and focus on the effect of the third level on the Berry curvature measurement. In Fig. 5.5, we plot the result obtained from $\langle\hat{\sigma}_z\rangle$ measurement as a function of ramp velocities for two different anharmonicities. For comparison, we also plot the Berry curvature obtained analytically for strictly two- and three-level systems. We find that as we increase the anharmonicity δ_{an}, all three plots coincide, as expected. However, for anharmonicity close to that of a transmon qubit, $\delta_{an}/2\pi = 200$ MHz, we find a few percentage difference between the result obtained from a full numerical simulation that takes the third level into account and that of analytical results for a strictly two- or three-level system.

5.5 Discussion

We have presented both theoretical and numerical analysis of the effect of decoherence on the measurement of the Berry curvature in superconducting qubits. We find that decoherence forces magnetization to respond linearly to the drive velocity in case of linear drives, thereby assisting in the Berry curvature measurement. In addition, we presented a formula for the correction due to dephasing and relaxation to the Berry curvature in a two-level system in the adiabatic frame. This result is consistent with previous studies of the effect of pure dephasing on the curvature. However, we clarified that the adiabatic frame is not well suited for studying the effect of decoherence on the curvature. Furthermore, we studied the effect of the third level on the Berry curvature measurement in phase or transmon qubits, which are attractive candidates for experimental measurement of the Berry curvature.

Chapter 6

Qubit relaxation from evanescent-wave Johnson noise: Dipole approximation

6.1 Introduction

So far in this thesis, we considered a phenomenological model of the noises and studied their effect on fidelity of control and measurement in superconducting qubit devices. In this chapter, we turn our attention to microscopic description of one of such noises that can be a cause of concern in semiconducting qubit devices.

Semiconducting quantum dots are promising candidates for scalable quantum information processing. Quantum dots are realized in a variety of experimental setups, including a Si and GaAs two-dimensional electron gas [113, 114, 115], semiconductor nanowires [116] and carbon nanotubes [117]. Several experiments performed on laterally coupled double quantum dots (DQDs) have demonstrated precise and rapid control of the coupling between electronic charge states and coherent manipulation of trapped electrons, leading to realization of a DQD as a qubit.

A schematic of the cross-section of such an architecture is shown in Fig. 6.1. These de-

vices are fabricated from heterostructures of GaAs and AlGaAs grown by molecular beam epitaxy. Free electrons are introduced by doping the AlGaAs layer with Si, which accumulate at the GaAs/AlGaAs interface, deep down in the minimum of the vertical potential, that provides strong confinement of the electrons along the growth direction. However, these electrons are free to move along the interface, where they form a two dimensional electron gas (2DEG) and can have a high mobility due to a relatively low electron density. The quantum dots are then defined by etching through the 2DEG or by depositing metallic gates on top of the heterostructure. Applying a negative voltage on these gates will deplete the 2DEG below them, leading to electron confinement in a desired location.

In almost all of these implementations, confinement and manipulation of an electron in a quantum dot is achieved by applying an electrostatic potential through metallic gates. While the metallic gates are crucial for qubit control, they can also act as a source of decoherence during qubit operations. This creates a control – isolation dilemma: connections from the outside world are what make the devices useful, but they are also sources of decoherence.

Several other decoherence mechanisms, such as hyperfine coupling of the trapped electron spin to host lattice nuclear spins in spin-based qubits [118] and electron coupling to phonon modes [119, 120, 50] in charge-based qubits, have been previously studied in an effort to identify the major source of decoherence in semiconductor qubits. A more recent study investigated decoherence due to voltage fluctuations in the metallic gates using the lumped circuit model of a DQD charge qubit [51]. In almost all of these studies, [119, 120, 50, 51] the estimated energy relaxation rate is at least an order of magnitude smaller than the rate observed experimentally [114, 113], suggesting that a different decoherence mechanism is dominant in current experimental setups for charge qubits.

The relaxation of a charge or spin qubit can also be induced by the thermal and quantum fluctuations of electromagnetic fields. The fluctuations of the electromagnetic fields are greatly enhanced in the vicinity of conductors because of the evanescent waves [121, 122, 123, 124, 125, 126]. An illustration of the concept is shown in Fig. 6.2. This evanescent-wave

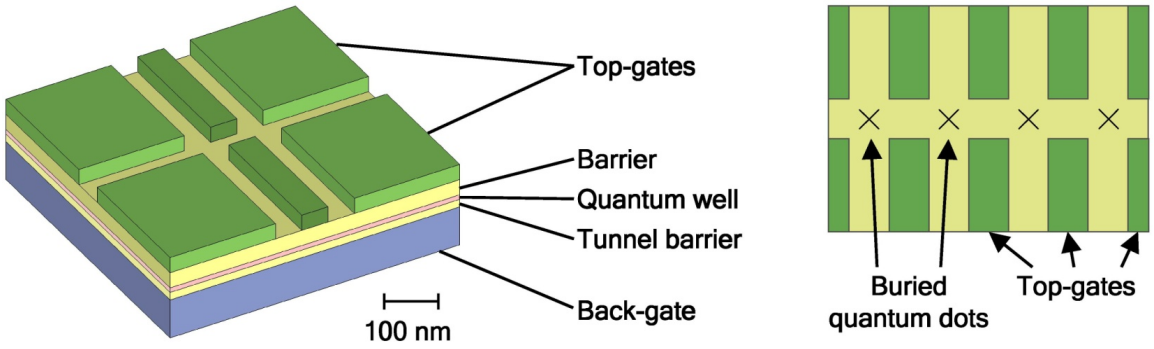

Figure 6.1: Schematic of the cross-section of a quantum dot architecture with surface metallic gates (green) and back gates (blue). Figure courtesy of Prof. Mark Eriksson's group.

Johnson noise (EWJN) has been shown, both theoretically [127] and experimentally [128], to be an important source of decoherence for atomic qubits near the metallic walls of a trap. In this work we investigate the effects of metallic device elements in solid-state qubit architectures. Similar investigations have been carried out previously using lumped –circuit calculations of Johnson noise [59, 129, 51]. Here we do the noise calculations taking into account the detailed spatial dependence of the fields and the important effects of non-local corrections to the electromagnetic response functions [130, 131].We focus particularly on situations likely to be of interest to experimenters, such as an electron in a quantum dot close to a gate electrode.

We pause here to mention that the EWJN originates from properties of the metal near its surface. The expressions for the electromagnetic field fluctuations presented in this paper are for a conducting half space. However, our treatment can be extended to calculate the strength of EWJN in the vicinity of a conducting slab of finite thickness. In this case, the electromagnetic fluctuations are independent of the thickness of the slab as long as this thickness is significantly larger than the skin depth of the metal. As such, we anticipate that EWJN may be alternatively interpreted as arising from overdamped surface plasmon excitations which exist within a skin depth of the surface of the metal [126].

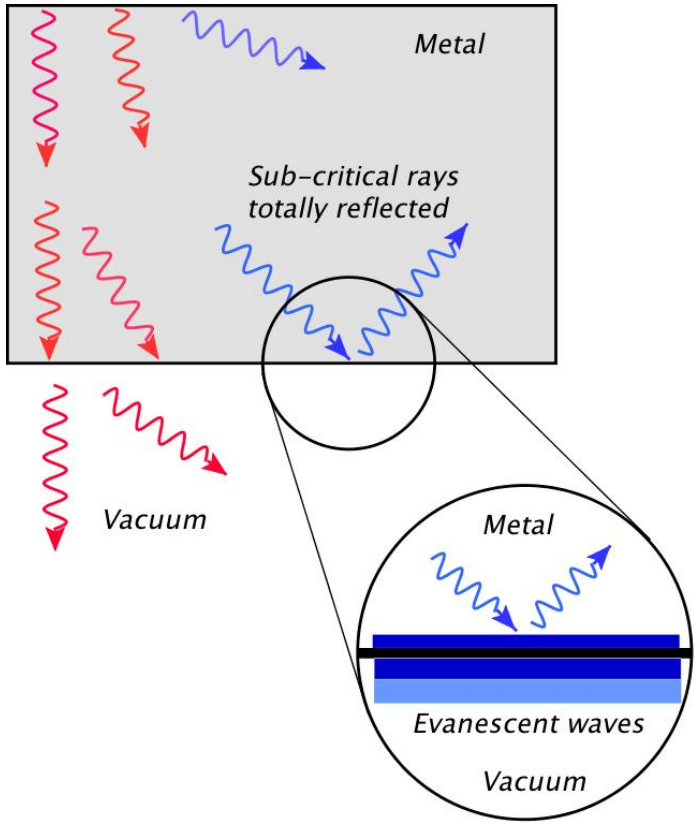

Figure 6.2: An illustration of evanescent-waves leaking outside of a conducting surface. This figure is adapted from Ref. [124].

6.2 Formalism

The interaction Hamiltonian between the fluctuating electric and magnetic fields and charge or spin qubits within the dipole approximation, which we will assume throughout this chapter, is given by :

$$H_{int} = -\vec{d} \cdot \vec{E}(\vec{r}, t)\,, \quad \text{(charge qubit)} \tag{6.1}$$

$$H_{int} = -\vec{\mu} \cdot \vec{B}(\vec{r}, t)\,, \quad \text{(spin qubit)}\,, \tag{6.2}$$

where $\vec{d}$ and $\vec{\mu}$ are electric and magnetic dipole moments, respectively. To describe the decoherence of qubits resulting from the evanescent electromagnetic fields surrounding a conducting gate, it is necessary to compute spectral densities S_{ij} of the electric and magnetic

field fluctuations, which are obtained from the cross-correlation tensor for the fields:

$$S_{ij}^{E}(\vec{r},\vec{r}\,',\omega) \equiv \frac{1}{2}\int_{0}^{\infty} e^{i\omega\tau}\left\langle\left\{E_i\left(\vec{r},\tau\right)\,,\,E_j\left(\vec{r}\,',0\right)\right\}\right\rangle\,d\tau \tag{6.3}$$

$$S_{ij}^{B}(\vec{r},\vec{r}\,',\omega) \equiv \frac{1}{2}\int_{0}^{\infty} e^{i\omega\tau}\left\langle\left\{B_i\left(\vec{r},\tau\right)\,,\,B_j\left(\vec{r}\,',0\right)\right\}\right\rangle\,d\tau \tag{6.4}$$

Fermi's golden rule imply that the relaxation rate $1/T_{1,c,s}$ of a (charge or spin, respectively) qubit transition of a particular frequency will be proportional to the spectral densities at that frequency, evaluated at coincident spatial arguments $\vec{r} = \vec{r}\,'$ (within the dipole approximation):

$$\frac{1}{T_{1,c}} = \frac{d^2}{\hbar^2} S_{ii}^{E}(\vec{r},\vec{r},\omega) \tag{6.5}$$

$$\frac{1}{T_{1,s}} = \frac{\mu^2}{\hbar^2} S_{ii}^{B}(\vec{r},\vec{r},\omega) \tag{6.6}$$

These spectral densities are connected to the electric and magnetic susceptibilities or response functions

$$\chi_{ij}^{E}(\vec{r},\vec{r}\,',\omega) \equiv \frac{i}{\hbar}\int_{-\infty}^{\infty} \theta(\tau)\, e^{i\omega\tau}\left\langle\left[E_i\left(\vec{r},\tau\right)\,,\,E_j\left(\vec{r}\,',0\right)\right]\right\rangle\,d\tau \tag{6.7}$$

$$\chi_{ij}^{B}(\vec{r},\vec{r}\,',\omega) \equiv \frac{i}{\hbar}\int_{-\infty}^{\infty} \theta(\tau)\, e^{i\omega\tau}\left\langle\left[B_i\left(\vec{r},\tau\right)\,,\,B_j\left(\vec{r}\,',0\right)\right]\right\rangle\,d\tau \tag{6.8}$$

by fluctuation dissipation theorem [132]:

$$S_{ij}^{E,B}(\vec{r},\vec{r}',\omega) = \hbar\,\coth\left(\frac{\hbar\omega}{2k_B T}\right)\mathrm{Im}\,\chi_{ij}^{E,B}(\vec{r},\vec{r}',\omega)\,. \tag{6.9}$$

As a result, the relaxation time $T_{1,c}$ of a charge qubit with dipole moment $\vec{d}$ pointing in the ith direction at position $\vec{r}$ and level separation ω will be given by

$$\frac{1}{T_{1,c}} = \frac{d^2}{\hbar}\,\mathrm{Im}\,\chi_{ii}^{E}(\vec{r},\vec{r},\omega)\,(1+N(\omega,T))\,, \tag{6.10}$$

and $T_{1,s}$ of a spin qubit with magnetic dipole moment $\vec{\mu}$ in the ith direction at position $\vec{r}$ and level separation ω will be given by

$$\frac{1}{T_{1,s}} = \frac{\mu^2}{\hbar}\,\mathrm{Im}\,\chi_{ii}^{B}(\vec{r},\vec{r},\omega)\,(1+N(\omega,T))\,, \tag{6.11}$$

where $N(\omega,T) = 1/[\exp(\hbar\omega/k_B\,T)-1]$ is the Planck's function. We deal first with fields that have been averaged over distances of the order of a_{atomic} and l_{mean}, where a_{atomic}

is an interatomic distance and l_{mean} is the mean free path in the metal. As a result the dielectric function $\epsilon(\vec{r},\omega)$ may be treated as a local function of space. This approximation breaks down in the near vicinity of the conducting surface, and the influence of a nonlocal dielectric response on the electric and magnetic field fluctuations is addressed below. The conducting electrodes in semiconductor qubit architectures are commonly constructed of copper. Therefore, all numerical results presented here use the electronic properties of copper near 0K. In this case, a local dielectric function may be used for distances much larger than the Fermi wavelength $\lambda_F = \sqrt{4\pi^2\hbar^2/mE_F} \approx 0.4$ nm. We work in a gauge where the scalar potential $\phi = 0$, so that for harmonic fields we have $\vec{E}_\omega = i\omega\vec{A}_\omega$.

The electric and magnetic susceptibilities can be shown [133, 126] to be directly related to the equilibrium retarded photon Green's function by the relations

$$\chi^E_{ij}(\vec{r},\vec{r}\,',\omega) = \frac{\omega^2}{\epsilon_0 c^2} D_{ij}\left(\vec{r},\vec{r}\,',\omega\right) \tag{6.12a}$$

$$\chi^B_{ij}(\vec{r},\vec{r}\,',\omega) = \frac{1}{\epsilon_0 c^2}\varepsilon_{ikm}\varepsilon_{jnp}\partial_k\partial_n D_{mp}\left(\vec{r},\vec{r}\,',\omega\right) \tag{6.12b}$$

where i, j are Cartesian indices that run over x, y, z, and D_{ij} satisfies

$$\left[-\delta_{ij}\left(\nabla^2 + \frac{\omega^2\epsilon\left(\vec{r},\omega\right)}{c^2}\right) + \partial_i\partial_j\right] D_{ik}\left(\vec{r},\vec{r}\,'\right) = \delta^3\left(\vec{r}-\vec{r}\,'\right)\delta_{jk}\,. \tag{6.13}$$

The geometry of a particular problem is expressed through the function $\epsilon\left(\vec{r},\omega\right)$. Eqs. 6.10 and 6.11 assume the charge or spin qubit can be adequately approximated as a point dipole. The effect of a qubit with an extended spatial distribution will be considered in future work. The task of computing D_{ij} in a particular geometry is, in general, a complicated problem in electrodynamics. In this chapter, we shall limit ourselves to the situation where the separation of the qubit from the metal surface is much less than any radius of curvature of the surface so that the surface can be thought of as flat.

Let z be the distance from the surface. The result for the spectral density of the electric field for local electrodynamics has been obtained by Henkel *et. al* [127]:

$$\chi^E_{xx}(z,z,\omega) = \frac{1}{8\pi\epsilon_0}\mathrm{Re}\int_0^\infty \frac{pdp}{q}e^{2iqz}\left(\frac{\omega^2}{c^2}r_s(p) - q^2 r_p(p)\right)\,, \tag{6.14a}$$

$$\chi^E_{zz}(z,z,\omega) = \frac{1}{4\pi\epsilon_0}\mathrm{Re}\int_0^\infty \frac{p^3}{q}dpe^{2iqz}r_p(p)\,, \tag{6.14b}$$

where $q = \sqrt{\omega^2/c^2 - p^2}$ for $p^2 \leq \omega^2/c^2$ and $q = i\sqrt{p^2 - \omega^2/c^2}$ for $p^2 > \omega^2/c^2$ is the z-component of the wavevector, and p is the transverse component. Our notation follows that of Ford and Weber [130].

$$r_s\,(p) = \frac{q - \sqrt{\omega^2\epsilon/c^2 - p^2}}{q + \sqrt{\omega^2\epsilon/c^2 - p^2}} \tag{6.15a}$$

and

$$r_p\,(p) = \frac{\epsilon q - \sqrt{\omega^2\epsilon/c^2 - p^2}}{\epsilon q + \sqrt{\omega^2\epsilon/c^2 - p^2}} \tag{6.15b}$$

are the Fresnel reflection coefficients. The corresponding expressions for the spectral densities of the magnetic field are identical to Eqs. 6.14 if we multiply by $1/c^2$ and make the replacement $r_s \leftrightarrow r_p$.

We are interested in separations that are sufficiently small so that retardation, and hence, radiation of the electromagnetic field may be neglected. This is known as the quasistatic approximation, and it is formally employed by taking the limit $c \to \infty$. This results in the greatly simplified expressions

$$\chi^E_{zz}(z,z,\omega) = 2\chi^E_{xx}(z,z,\omega) = \frac{1}{16\pi\epsilon_0 z^3}\mathrm{Im}\frac{\epsilon - 1}{\epsilon + 1}\,, \tag{6.16a}$$

$$\chi^B_{zz}(z,z,\omega) = 2\chi^B_{xx}(z,z,\omega) = \frac{\omega^2}{16\pi\epsilon_0 c^4 z}\mathrm{Im}(\epsilon - 1)\,. \tag{6.16b}$$

Employing this approximation has eliminated the functional difference between the transverse and longitudinal components of the field fluctuations. The quasistatic expressions differ from the exact values by less than 1% when $z < \delta/10$, where δ is the skin depth of the metal. For copper near absolute zero, $\delta \sim 3\,\mu$m. Eqs. 6.16 diverge as $z \to 0$, but this divergence is not physical: it is an artifact of treating the dielectric function as local at distances comparable to the interatomic spacing. In any differential equation satisfied by the spatial Fourier components of D_{ij}, a local dielectric function will be independent of the wavevector while a nonlocal one will have a nontrivial wavevector dependence. It is conventional to represent the spatial Fourier components of the nonlocal dielectric function

as a tensor quantity in the form

$$\epsilon_{ij}(\vec{k},\omega) = \epsilon_l(k,\omega)\frac{k_i k_j}{k^2} + \epsilon_t(k,\omega)\left(\delta_{ij} - \frac{k_i k_j}{k^2}\right), \tag{6.17}$$

where we have separated the function into its longitudinal ϵ_l and transverse ϵ_t components.

Nonlocality in the dielectric function changes the reflection coefficients. In the quasistatic approximation r_p is [130]

$$r_p = \frac{1 - \dfrac{2p}{\pi}\displaystyle\int_0^\infty d\kappa \frac{1}{k^2\epsilon_l(k,\omega)}}{1 + \dfrac{2p}{\pi}\displaystyle\int_0^\infty d\kappa \frac{1}{k^2\epsilon_l(k,\omega)}} \tag{6.18a}$$

and r_s becomes

$$r_s = \frac{\frac{2ic^2}{\pi\omega}\int_0^\infty d\kappa/\{\epsilon_t(k,\omega) - c^2\,k^2/\omega^2\} - \omega/q}{\frac{2ic^2}{\pi\omega}\int_0^\infty d\kappa/\{\epsilon_t(k,\omega) - c^2\,k^2/\omega^2\} - \omega/q}\,. \tag{6.18b}$$

Here $k^2 = p^2 + \kappa^2$,

$$\epsilon_l(k,\omega) = 1 + \frac{3\omega_p^2}{k^2 v_F^2}\frac{(\omega + i\nu) f_l((\omega + i\nu)/kv_F)}{\omega + i\nu f_l((\omega + i\nu)/kv_F)} \tag{6.19a}$$

$$\epsilon_t(k,\omega) = 1 - \frac{\omega_p^2}{\omega(\omega + i\nu)} f_t((\omega + i\nu)/kv_F) \tag{6.19b}$$

$$f_l(x) = 1 - \frac{x}{2}\ln(x+1)/(x-1) \tag{6.20a}$$

$$f_t(x) = \frac{3}{2}x^2 - \frac{3}{2}x(x^2-1)\ln(x+1)/(x-1), \tag{6.20b}$$

ν is the electron collision frequency, $\omega_p = (ne^2/m\epsilon_0)^{1/2}$ is the plasma frequency, and v_F is the Fermi velocity.

Although Eqs. 6.14 are derived assuming locality, it is a convenient fact [130] that these equations are also valid in the nonlocal regime, as long as the nonlocal form of the Fresnel coefficients Eqs. 6.18 are used.

6.3 Results

In Fig. 6.3, we present the zero-temperature results for the relaxation time T_1 from EWJN for a qubit with an electric dipole moment of magnitude $|e|a_B$, where a_B is the Bohr radius.

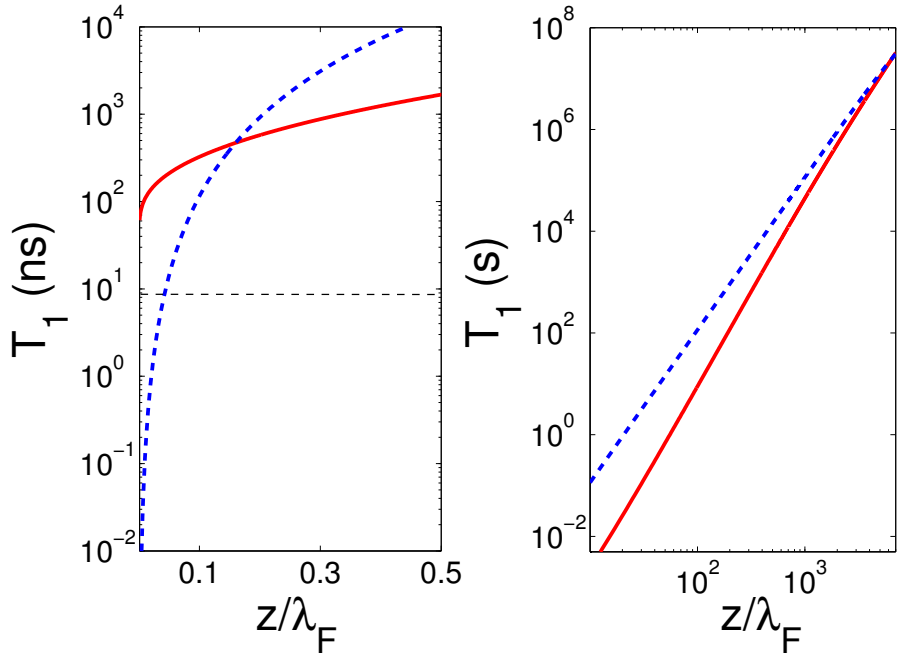

Figure 6.3: Plot of the T_1 time of a charge qubit computed from Eq. (1) using the local approximation (dashed blue) and the full nonlocal theory (solid red). We used the values $E_F = 7$ eV, $\omega = 6\pi \times 10^8$ s^{-1}, $\nu = \pi \times 10^{13}$ s^{-1}, and $\omega_p = 1.6 \times 10^{16}$ s^{-1}, appropriate for a copper surface and a device operating in the GHz range. The dipole moment is taken as $d = |e|a_B$, where $|e|$ is minus the charge on the electron and a_B is the Bohr radius. These results are for zero temperature. The dashed horizontal line in the left figure represents the strength of the electric field fluctuations inside the bulk of a uniform metal.

Both the local and nonlocal results are shown. It is seen that the correct nonlocal dielectric function eliminates the unphysical divergence of $1/T_1$ at $z = 0$. For separations $z \sim \lambda_F$, the differences are very significant, while for $z > l_{mean} = v_F/\nu \approx 200\lambda_F$, the local and nonlocal results nearly coincide. It is interesting to note that for the electric field fluctuations there is a crossover region where the nonlocal result becomes larger than the local result in the range $\lambda_F < z < l_{mean}$ (see Fig. 6.3), in alignment with the results of Volokitin *et. al* [125] who showed an enhancement of the nonlocal result above the local result. We see that at $T = 0$ and GHz operations, T_1 from spontaneous emission is of the order of seconds at separations $z \sim 30\lambda_F$. These results are directly applicable to atomic qubits, but the rate $1/T_1$ is proportional to the square of the dipole moment, so rates for other charge qubits are easily deduced.

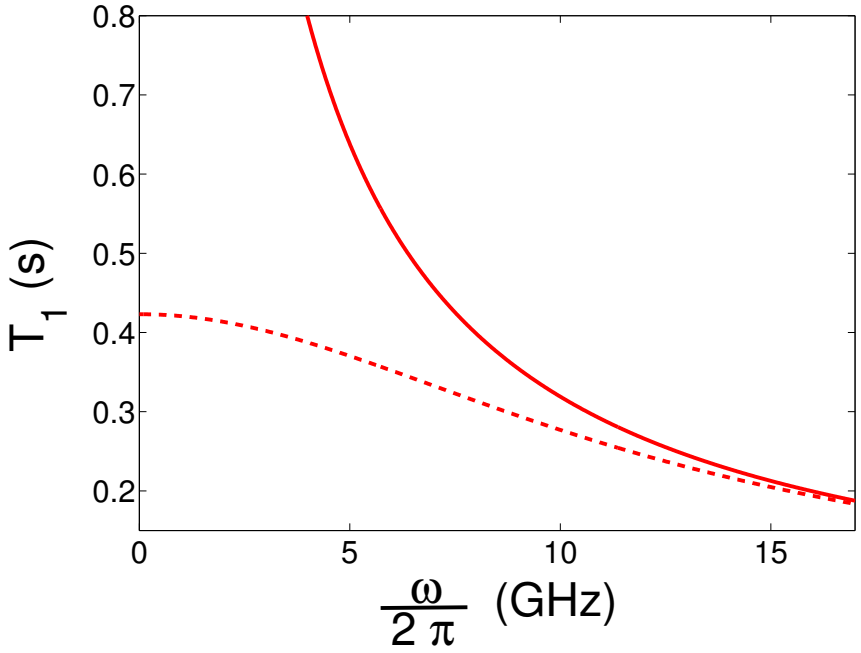

Figure 6.4: Plot of the T_1 time *vs.* frequency ω of a charge qubit computed from Eq. (1) at different temperatures (solid red at 0 K and dashed red at 25 mK) at fixed $z = 30\lambda_F$. $E_F = 7$ eV, $\nu = \pi \times 10^{13}$ s^{-1}, $\omega_p = 1.6 \times 10^{16}$ s^{-1}, and $d = |e|a_B$, as in Fig. 6.3.

Fig. 6.4 shows that T_1 falls off slowly at higher frequencies. The divergence of T_1 as $\omega \to 0$ is removed by including a small finite temperature. Fig. 6.4 is plotted using the non-local expression for the z-component of the field fluctuations.

Fig. 6.5 gives the analogous results for magnetic EWJN on a spin qubit with a magnetic dipole moment of 1 Bohr magneton. Nonlocal corrections are somewhat stronger for this case, and persist to larger distances. Interestingly, the falloff with distance of T_1 is slower for magnetic EWJN than for electric EWJN. However, magnetic relaxation times are typically somewhat larger than electric relaxation times. The crossover of the local and nonlocal results is not present in the magnetic case. Fig. 6.6 shows that the frequency and temperature dependence of magnetic EWJN is similar to the electric EWJN shown in Fig. 6.4. Brief mention should be made of the dip that is observed as $\omega \to 0$ in Fig. 6.6. The reflection coefficients r_s contribute to the magnetic field fluctuations. This contrasts with the electric case, where only r_p contributes to leading order in ω/c. The dip is a result

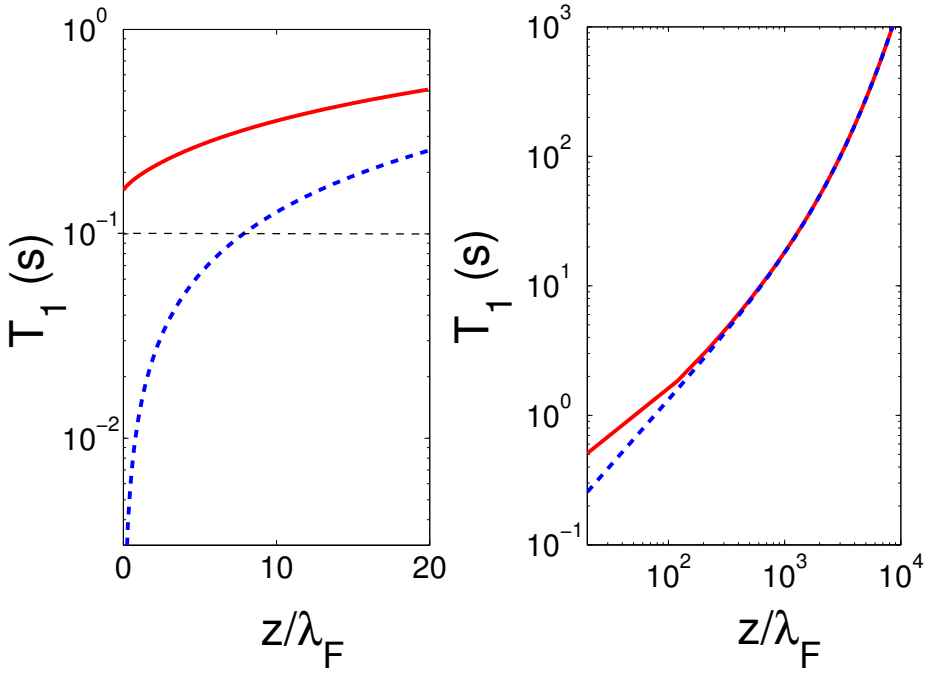

Figure 6.5: Plot of T_1 time for a spin qubit at zero temperature computed from Eq. (2) in the local approximation (dashed blue) and the full nonlocal theory (solid red). $E_F = 7$ eV, $\omega = 6\pi \times 10^8$ s^{-1}, $\nu = \pi \times 10^{13}$ s^{-1}, and $\omega_p = 1.6 \times 10^{16}$ s^{-1}, appropriate for a copper surface and a device operating in the GHz range. We have taken $\mu = g\mu_B$, appropriate for a single electron, where the gyrometric factor of an electron $g \approx 2$. The rate $1/T_1$ is proportional to the square of μ, so rates for other local magnetic qubits can be easily deduced. The dashed horizontal line in the left figure represents the strength of the magnetic field fluctuations inside the bulk of a uniform metal.

of the contributions of r_s to the field fluctuations. The r_s term in χ^B_{ii} is linear in ω as $\omega \to 0$ and negative, while the r_p term is cubic in ω as $\omega \to 0$ and positive. We should also mention that for extremely small ω the factor of $N(\omega, T)$ cancels out the linear ω dependence and the dip flattens out as $\omega \to 0$ (not observable in the resolution of Fig. 6.6).

The limit of the nonlocal quasistatic field fluctuations as $z \to 0$ should be of the same order of magnitude as the value of these fluctuations inside the metal. To check this, we calculate the electromagnetic Green's function inside the bulk of a uniform metal using a nonlocal dielectric function. The result is

$$D_{ij}(\vec{k}, \omega) = \frac{1}{\omega^2 \epsilon_t / c^2 - k^2} \left(\delta_{ij} - \frac{c^2 k_i k_j}{\omega^2 \epsilon_l} + \frac{k_i k_j}{k^2 \epsilon_l} (\epsilon_t - \epsilon_l) \right) \tag{6.21}$$

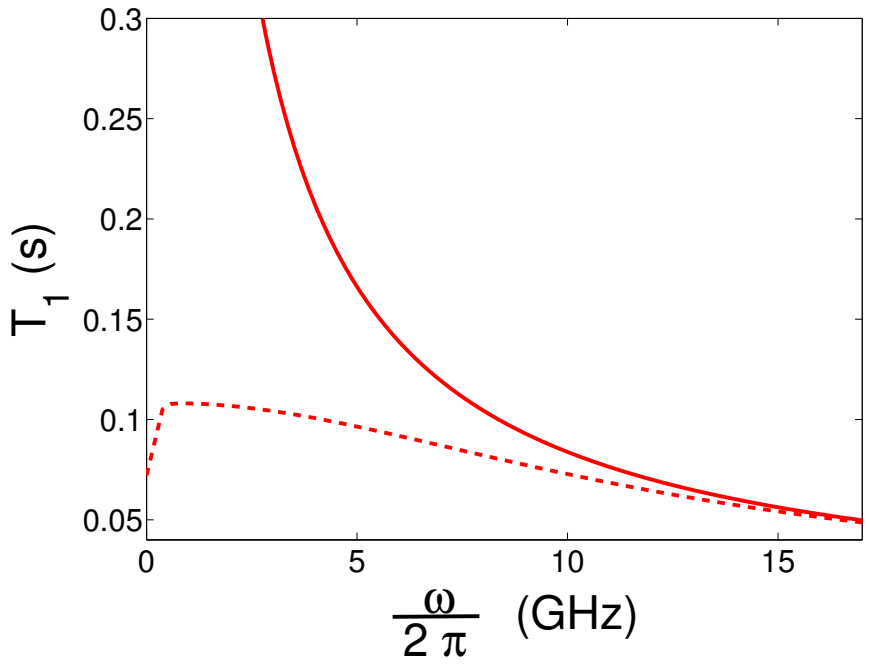

Figure 6.6: Plot of the T_1 time *vs.* frequency of spin qubit computed at different temperatures (solid red at 0 K and dashed red at 25 mK) at fixed $z = 30\lambda_F$. $E_F = 7$ eV, $\nu = \pi \times 10^{13}$ s^{-1}, and $\omega_p = 1.6 \times 10^{16}$ s^{-1}, appropriate for a copper surface. $\mu = g\mu_B$ as in Fig. 6.5.

$$D_{ij}(\vec{r} - \vec{r}\,', \omega) = \frac{1}{(2\pi)^3} \int d^3\vec{k} e^{i\vec{k}\cdot(\vec{r}-\vec{r}\,')} D_{ij}(\vec{k}, \omega) \tag{6.22}$$

Numerical evaluation of Eq. 6.22 when $\vec{r} = \vec{r}\,'$ gives (imaginary parts) $D_{xx} = D_{zz} \sim 3 \times 10^{19}$ m^{-1}. An evaluation of the Green's function outside the metal in the nonlocal quasistatic regime for $z \to 0$ gives (imaginary part) $D_{xx} \sim 1.25 \times 10^{19}$ m^{-1} and $D_{zz} \sim 2.47 \times 10^{19}$ m^{-1}, slightly less than in the bulk of a uniform metal, as expected.

We see that there are three relevant distance regimes. For $z < \lambda_F$, a quasistatic approximation to Henkel's results 6.14 using the *nonlocal* expressions for r_s and r_p will accurately describe the field fluctuations. For intermediate distances $\lambda_F < z < l_{mean}$, there is a significant enhancement in the electric field fluctuations of the nonlocal expression compared to the local expression. For distances $l_{mean} < z < 10\,\delta$, local forms Eq. 6.14 will accurately describe the field fluctuations, while for $z >> \delta$, retardation effects must also be taken into account.

Comparison of our results with experimental measurements of T_1 times for spin relaxation in single-electron quantum dots supports the notion that relaxation from EWJN may sometimes constitute the dominant relaxation mechanism in present semiconductor qubit architectures. In particular, we reference the low B saturation of T_1 for a single electron in Fig. 6.6(d) of [134] by Xiao *et. al.* In their measurements, T_1 saturates to ~ 40 ms. Plugging their values of $z = 50$ nm and $\hbar\omega = 0.4$ meV into Eq. 6.16b gives a value of $T_1 \sim 15$ ms. That our expression gives a shorter relaxation time than what was measured can be understood because we assume the gates constitute a conducting half-space, rather than the more sparse gate geometry used in [134]. It is also instructive to compare our results with the measurements of Elzerman et al. in [135]. They measured a T_1 of 0.55 ms at a magnetic field of $10\,T$. Using their values of $z = 90$ nm and $\hbar\omega = 0.2$ meV, our results predict $T_1 \sim 1$ s. EWJN is clearly not the dominant relaxation mechanism in this situation. Through a perusal of the literature, we have found generally that EWJN is insufficient to describe the spin relaxation rate in experiments with a high external magnetic field.

6.4 Discussion

The density of photon states in a metal is very high owing to the large polarizability. For blackbody radiation, this high density of states does not matter, since total internal reflection reduces the outgoing radiation flux to its universal Stefan-Boltzmann value. In contrast, the evanescent waves are strongly enhanced and the resultant electromagnetic noise just outside the surface can be intense. This is a concern for quantum devices operating close to metallic objects. This paper has concentrated on the frequency, temperature, and distance dependence of the noise, and on the effects of assuming a local dielectric function. We conclude that the effect is significant for charge qubits with large dipole moments such as double quantum dots. The EWJN relaxation may be the limiting decoherence effect in designs which involve close proximity to bulk metals. For magnetic qubits the effects are smaller, but as can be seen by comparison to [134], they can still be significant. We found that nonlocal effects are very important at short distances - indeed, local calculations can

produce spurious divergences. At distances large compared to the Fermi wavelength of the metal, local approximations work well.

We have not considered extended qubits for which the off-diagonal function $D_{ii}(\vec{r}, \vec{r}\,')$ at $\vec{r} \neq \vec{r}\,'$ is required. The extended qubit geometries will be considered in detail in the next chapter.

Chapter 7

Qubit relaxation due to evanescent-wave Johnson noise: Beyond dipole approximation

7.1 Introduction

In this chapter, we continue our discussion about the decoherence in a quantum dot due to electromagnetic field fluctuations near the metallic gates. In Fig. 7.1, we show the schematic cross-section of the type of device we consider in this chapter [136]. The picture of the actual device is shown on the right panel. The previous chapter 6, as well as other theoretical estimates [127] of the effect of Johnson noise in atomic and quantum dot based qubits, use the dipole approximation, which is a valid approximation if the distance from the metallic gate to the qubit is much larger than the size of the qubit. However, it may be necessary to go beyond the dipole approximation in the case of EWJN in a quantum dot.

Here we present our study of the energy relaxation of a single electron charge qubit in a DQD system and a single electron spin qubit in a single quantum dot. We assume that the primary source of field fluctuations are the metallic top gates of the quantum dot architecture. Back gates are typically a distance on the order of a micron from the qubits,

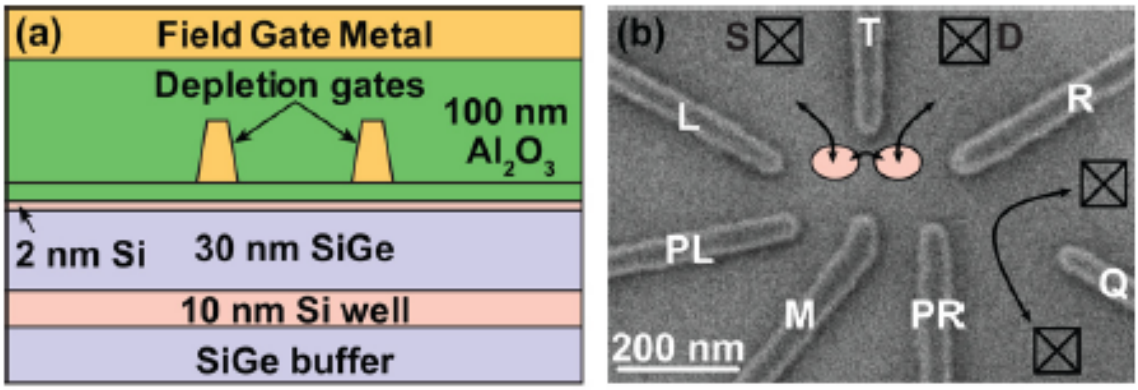

Figure 7.1: (a) Schematic cross-section of the device. (b) Scanning electron micrograph of the actual device. Pictures reprinted with permission from Ref. [136]. Copyright 2011, AIP Publishing LLC.

which is too far to experience significant EWJN enhancement. We consider the detailed spatial variation of the electromagnetic field fluctuations and present results beyond the dipole approximation which take into account the finite size of the quantum dot. We show that this extension of the dipole approximation removes the unphysical divergence in the relaxation rate at the metallic surface.

This chapter is organized as follows: In Section 7.2 we present our formalism for calculating the relaxation rate of a charge qubit beyond dipole eapproximation. Results are presented for a DQD geometry. Section 7.3 presents the formalism and results for the relaxation rate of a spin qubit in a single QD. In Section 7.4 we derive an enhancement of the noise spectrum that results as the thickness of the metallic gate is decreased. Finally, Section 7.5 summarizes our results. Our results indicate that EWJN is the dominant cause of energy relaxation in some spin qubit experiments, particularly those performed in a small external magnetic field, and is comparable in effect with previously studied noise sources in charge qubits.

7.2 Charge qubit

We consider a charge qubit realized in a gated lateral DQD in an AlGaAs/GaAs heterostructure where electron confinement along the z direction is much smaller than in the x or y directions, so that we can safely decouple the dynamics along x and y directions from the z direction [1]. The total Hamiltonian of the charge qubit and its interaction with the electromagnetic environment is given by

$$H = H_q + H_{int} \tag{7.1}$$

where H_q is the Hamiltonian of the charge qubit in a DQD, which we model in the basis of the localized charge states $\{|L\rangle, |R\rangle\}$ as $H_q = \varepsilon/2(|L\rangle\langle L| - |R\rangle\langle R|) + \Delta/2(|L\rangle\langle R| + |R\rangle\langle L|)$. ε is the bias energy between the two dots, and Δ is the tunneling amplitude. In the energy eigenbasis this Hamiltonian reduces to

$$H_q = \frac{\hbar\omega}{2}\sigma_z \tag{7.2}$$

where σ_z is the Pauli matrix, and $\hbar\omega = \sqrt{\varepsilon^2 + \Delta^2}$. For all our calculations except those in Fig. 7.3, we will set $\varepsilon = 0$. The interaction Hamiltonian H_{int} may be expressed in this same basis as

$$H_{int} = -\int d\vec{r}\left[\hat{\sigma}_x \vec{M}_r(\vec{r}) + \hat{\sigma}_z \vec{M}_\phi(\vec{r})\right] \cdot \vec{A}(\vec{r}, t) \ , \tag{7.3}$$

where $\vec{A}(\vec{r}, t)$ is the vector potential of the fluctuating field. $\vec{M}_r$ and $\vec{M}_\phi$ are associated with energy relaxation and pure dephasing in the charge qubit, respectively and are defined as

$$\vec{M}_r(\vec{r}) \equiv \frac{e}{m}\psi_+^*(\vec{r})\,\vec{p}\,\psi_-(\vec{r}) - \frac{ie\hbar}{2m}\psi_+^*(\vec{r})\,\psi_-(\vec{r})\,\nabla\,,$$
$$\vec{M}_\phi(\vec{r}) \equiv \frac{e}{2m}\left[\psi_+^*(\vec{r})\,\vec{p}\,\psi_+(\vec{r}) - \psi_-^*(\vec{r})\,\vec{p}\,\psi_-(\vec{r})\right] - \frac{ie\hbar}{4m}\left[\psi_+^*(\vec{r})\,\psi_+(\vec{r})\,\nabla - \psi_-^*(\vec{r})\,\psi_-(\vec{r})\,\nabla\right].$$

Here m is the effective mass and $\vec{p}$ is the momentum operator of the trapped electron. Because we are operating within the weak field limit, the term proportional to $\vec{A}^2$ has been dropped from the interaction Hamiltonian. We choose the gauge where the scalar potential

[1] In the 1D case of a DQD realized in carbon nanotube [117], or semiconducting nanowire [116], we assume the electron dynamics along the x direction are decoupled from that of the y and z directions.

$\phi = 0$ so that $\vec{E} = -\partial_t \vec{A}$. The expression for H_{int} derives from an interaction in terms of operator quantities of the form

$$H_{int} = -\frac{e}{2m}\Big(\vec{A}(\vec{r},t)\cdot\vec{p} + \vec{p}\cdot\vec{A}(\vec{r},t)\Big)\,. \tag{7.4}$$

This symmetrized version of the vector potential is not strictly necessary in our case since we are only interested in the near-field contribution to the Greens function for which $\nabla\cdot\vec{A} = 0$, but we included it to keep our results more generally applicable. The relaxation rate $\Gamma_{1,c} = 1/T_{1,c}$ can be calculated using the following expression, which follows directly from the Fermi golden rule:

$$\Gamma_{1,c} = \frac{1}{\hbar^2}\sum_{ij}\int d^3\vec{r}\int d^3\vec{r}\,'\, M_r^{*i}(\vec{r})\, M_r^j(\vec{r}\,')S_{ij}(\vec{r},\vec{r}\,',\omega)\,, \tag{7.5}$$

where S_{ij} is the spectral density of the vector potential:

$$S_{ij}(\vec{r},\vec{r}\,',\omega) \equiv \frac{1}{2}\int_0^\infty e^{i\omega\tau}\left\langle\{A_i\left(\vec{r},\tau\right)\,,\,A_j\left(\vec{r}\,',0\right)\}\right\rangle\, d\tau \tag{7.6}$$

The spectral density is related to the response function or susceptibility of the vector potential,

$$\chi_{ij}(\vec{r},\vec{r}\,',\omega) \equiv \frac{i}{\hbar}\int_{-\infty}^\infty \theta(\tau)\, e^{i\omega\tau}\left\langle[A_i\left(\vec{r},\tau\right)\,,\,A_j\left(\vec{r}\,',0\right)]\right\rangle\, d\tau\,, \tag{7.7}$$

via fluctuation-dissipation theorem [132]:

$$S_{ij}(\vec{r},\vec{r}\,',\omega) = \hbar\,\coth\left(\frac{\hbar\omega}{2k_BT}\right)\chi_{ij}^{''}(\vec{r},\vec{r}\,',\omega)\,, \tag{7.8}$$

where $\chi_{ij}^{''}(\vec{r},\vec{r}\,',\omega)$ is the imaginary part of the susceptibility and is given by

$$\chi_{ij}^{''}(\vec{r},\vec{r}\,',\omega) \equiv \mathrm{Im}\,\chi_{ij}(\vec{r},\vec{r}\,',\omega) = \frac{1}{2\hbar}\int_{-\infty}^\infty e^{i\omega\tau}\left\langle[A_i\left(\vec{r},\tau\right)\,,\,A_j\left(\vec{r}\,',0\right)]\right\rangle\, d\tau\,. \tag{7.9}$$

Combining the Fermi's golden rule with fluctuation-dissipation theorem, the zero temperature relaxation rate can be written as:

$$\Gamma_{1,c} = \frac{1}{\hbar}\sum_{ij}\int d^3\vec{r}\int d^3\vec{r}\,'\, M_r^{*i}(\vec{r})\, M_r^j(\vec{r}\,')\,\mathrm{Im}\,\chi_{ij}(\vec{r},\vec{r}\,',\omega)\,, \tag{7.10}$$

At finite temperature, the emission (transition from excited to ground state) and absorption (transition from ground to excited state) rates are given by

$$\Gamma^e_{1,c} = (1 + N(\omega, T))\Gamma_{1,c}\,,$$
$$\Gamma^a_{1,c} = N(\omega, T)\Gamma_{1,c} \tag{7.11}$$

The Planck function $N(\omega, T) = 1/[\exp(\hbar\omega/k_B T) - 1]$ gives the average occupation number of environment modes with frequency ω at temperature T. The response function or susceptibility of the vector potential χ_{ij} is related to the retarded photon Green's function D_{ij} by [133]

$$\chi_{ij}\left(\vec{r}, \vec{r}\,', \omega\right) = \frac{1}{\epsilon_0 c^2} D_{ij}\left(\vec{r}, \vec{r}\,', \omega\right)\,,$$

where i, j are Cartesian indices that run over x, y, z and the square brackets denote the commutator. D_{ij} is obtained by solving

$$\left[-\delta_{ij}\left(\nabla^2 + \frac{\omega^2 \epsilon\left(\vec{r}, \omega\right)}{c^2}\right) + \partial_i \partial_j\right] D_{ik}\left(\vec{r}, \vec{r}\,', \omega\right) = \delta^3\left(\vec{r} - \vec{r}\,'\right)\delta_{jk}. \tag{7.12}$$

Here the relative permittivity $\epsilon(\vec{r}, \omega)$ characterizes the geometry of a particular problem. In this section, we shall limit ourselves to the case where the metallic top gate of the lateral DQD is approximated by the half-space, $z < 0$. Then we can derive an analytical expression for D_{ij} [133, 122]

$$D_{ij}(\vec{r}, \vec{r}\,', \omega) = \frac{1}{4\pi^2}\int e^{i\vec{k}\cdot\vec{\boldsymbol{\imath}}_\parallel}\tilde{D}_{ij}(\vec{k}, z, z', \omega)\, d\vec{k}\,, \tag{7.13}$$

$$\tilde{D}_{xx}(\vec{k}, z, z', \omega) = \frac{i}{2q} e^{iq(z+z')}\left[r_s(k, \omega)\cos^2\theta - \frac{q^2 c^2}{\omega^2} r_p(k, \omega)\sin^2\theta\right], \tag{7.14}$$

where r_s and r_p are Fresnel's reflection coefficients given by

$$r_p(k, \omega) = \frac{\epsilon q - q_1}{\epsilon q + q_1}\,, \quad r_s(k, \omega) = \frac{q - q_1}{q + q_1}\,.$$

Here $\vec{k} \equiv (k_x, k_y)$, $\vec{\boldsymbol{\imath}}_\parallel \equiv \vec{r}_\parallel - \vec{r}\,'_\parallel = (x - x', y - y')$, θ is the angle between $\vec{k}$ and the x-axis, and $q = \sqrt{\omega^2/c^2 - k^2}$ and $q_1 = \sqrt{\epsilon\omega^2/c^2 - k^2}$ are the z-components of the photon wavevector in the vacuum and the metal, respectively. All other components of $\tilde{D}_{ij}$ can be derived from

$\tilde{D}_{xx}$. [133] In this work we consider $\epsilon \approx i\sigma/\omega\epsilon_0$, where $\sigma = 6 \times 10^7$ S/m is the conductivity of the copper gate.

We pause briefly to mention that typical models of the interaction of a DQD with the electromagnetic field use the dipole interaction Hamiltonian

$$H_{int} = -\vec{E}(\vec{r}) \cdot \vec{d}, \tag{7.15}$$

which will result in a relaxation rate of

$$\Gamma_{1,c} = \frac{d^2\omega}{8\pi\hbar z^3\sigma} \tag{7.16}$$

in the quasistatic approximation, where $\vec{d}$ is the dipole moment of the qubit and $\vec{E}(\vec{r})$ is the strength of the fluctuating electric field evaluated at the location of the qubit. Here we also assume that the dipole moment points along the z-direction. This expression approximates that the electric field is uniform over the spatial extent of the qubit, which is equivalent to treating the qubit as a point dipole. Here we also . As such, the qubit is able to couple to arbitrarily small wavelengths of the electromagnetic spectrum, and the relaxation rate is seen to diverge at shorter distances as $\sim 1/z^3$ if the conductor is modeled with a local dielectric function [127, 33]. Using the complete electromagnetic interaction Hamiltonian 7.4 accounts for fluctuations of the field over the spatial extent of the qubit. If the wavelength of a particular Fourier component of the field fluctuations is smaller than the length of the qubit in that direction, its influence on the electron will average out and it will not contribute to qubit relaxation. The exact and dipole approximation forms of the interaction Hamiltonian, Eqs. 7.4 and 7.15, converge when the distance from the gate becomes larger than the spatial extent of the qubit.

We present calculations of the relaxation time for charge qubits that highlight the differences between these two forms of the interaction. First we consider DQDs in a one dimensional nanowire, which are realizable in semiconducting nanowires [117] or carbon nanotubes [116]. In such a geometry, the wave functions of trapped electrons in quantum dots have appreciable spatial extent in only one direction. We model the confining potential of the DQD as a symmetric double square well potential and compute the lowest two

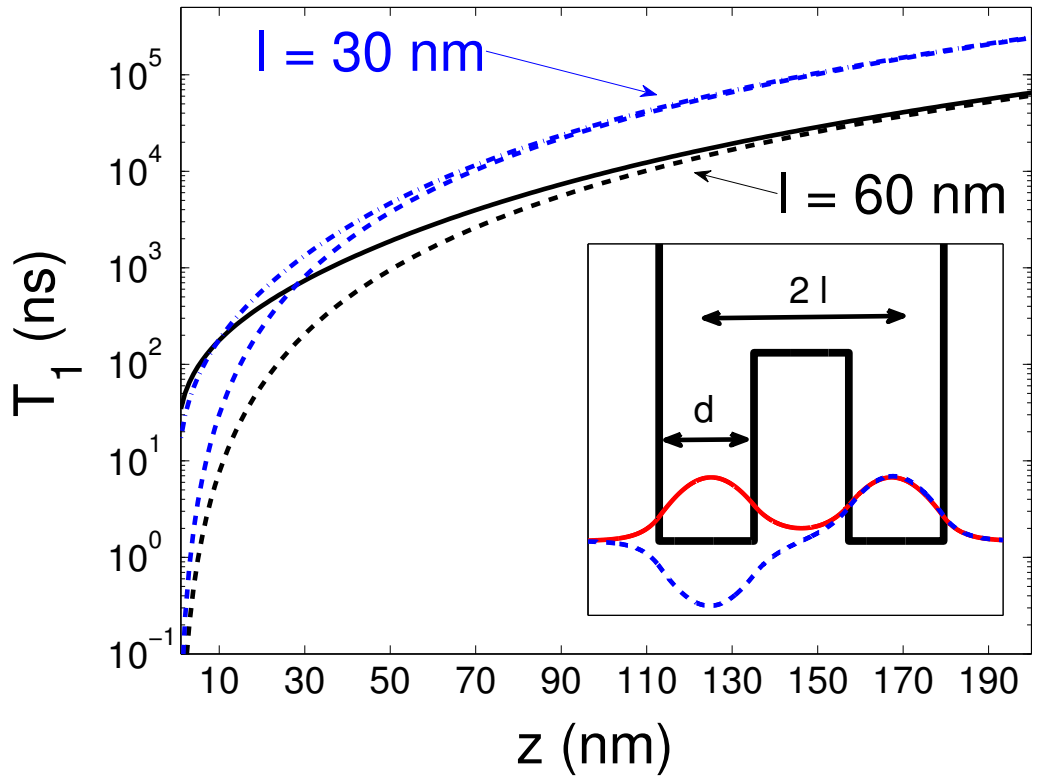

Figure 7.2: Energy relaxation time T_1 *vs.* the distance from the metallic gate to the DQDs z for dot geometry of $d = 30$ nm and $l = 30$ nm (dashed and dash-dotted blue lines) and 60 nm (solid and dashed black lines) at 0 K, $\omega/2\pi = 1$ GHz, and $\varepsilon = 0$. Solid and dash-dotted lines are T_1 times for the exact form of the interaction Hamiltonian, whereas dashed lines are for the dipole form of the interaction. The inset in the figure displays confining potential of a typical DQD in a one dimensional nanowire and the corresponding symmetric ground state and antisymmetric first excited state.

eigenenergies and wavefunctions. We then compute the relaxation rate between these two lowest states which are separated by a fixed transition frequency $\omega/2\pi = 1$ GHz. A plot of the wave functions and the shape of the potential is shown in the inset of Fig. 7.2.

We plot the energy relaxation time T_1 vs. the distance z from the metallic gate to the DQD in Fig. 7.2. In this plot, we choose the size of the dot in the x-direction $d = 30$ nm and half the separation between the dots $l = 30$ nm (dash-dotted and dashed blue lines) and 60 nm (solid and dashed black lines). The curves that are shown in solid and dash-dotted lines are relaxation times for the exact form of the interaction Hamiltonian, whereas those

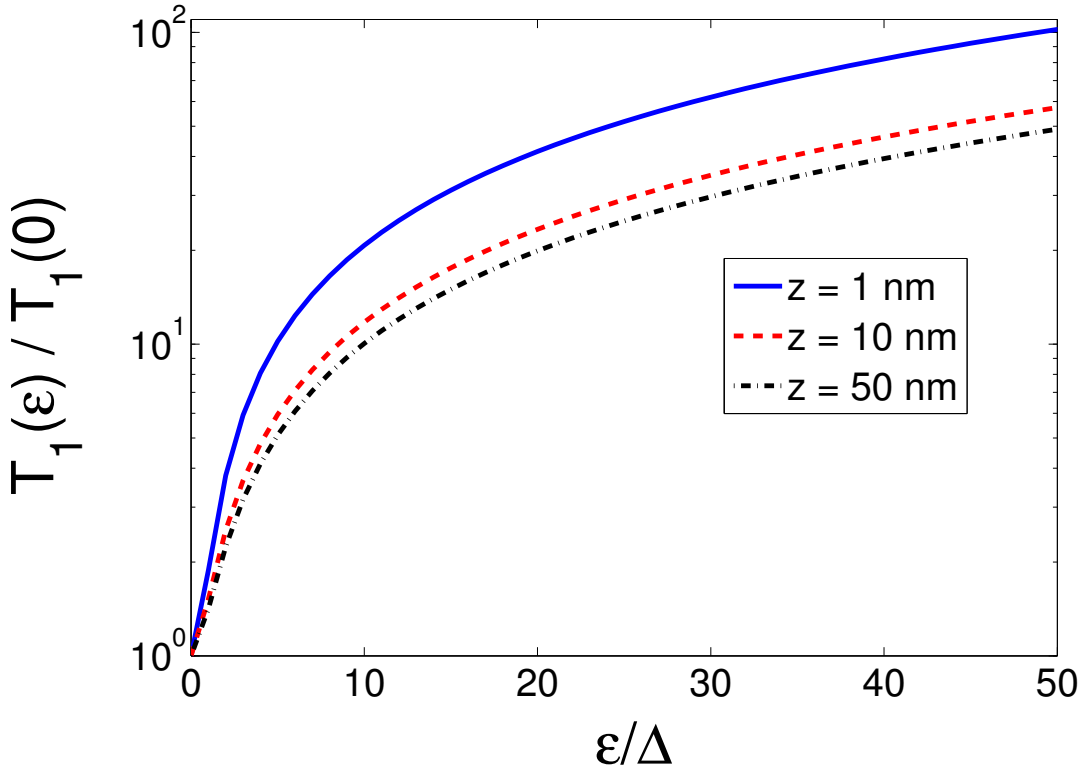

Figure 7.3: Ratio of the T_1 time for finite bias ε to the T_1 time at zero bias *vs.* ε/Δ for three values of distances z from the metallic gate: 1 nm (solid blue line), 10 nm (dashed red line) and 50 nm (dash-dotted black line), for a dot geometry of $d = 30$ nm and $l = 30$ nm at 0 K temperature.

shown in dashed lines are obtained using the dipole form of the interaction. The curves show significant deviation of the exact relaxation rate from the dipole relaxation rate at shorter distances and convergence of the two results at longer distances.

In Fig. 7.3, we present the ratio of T_1 for a charge DQD qubit at bias ε to the T_1 obtained at $\varepsilon = 0$ *vs.* the ratio ε/Δ. An increase in bias increases the level splitting and decreases the dipole moment of the DQD. Since the relaxation time $T_1 \sim 1/\omega d^2$, where $d = 2l \sin(\arctan(\Delta/\varepsilon))$ is the dipole moment of the quantum dot, T_1 increases for larger bias.

Next, we present results from the relaxation rate calculation for a DQD in a two-dimensional quantum well. In this treatment we label the z-axis as the vertical confinement

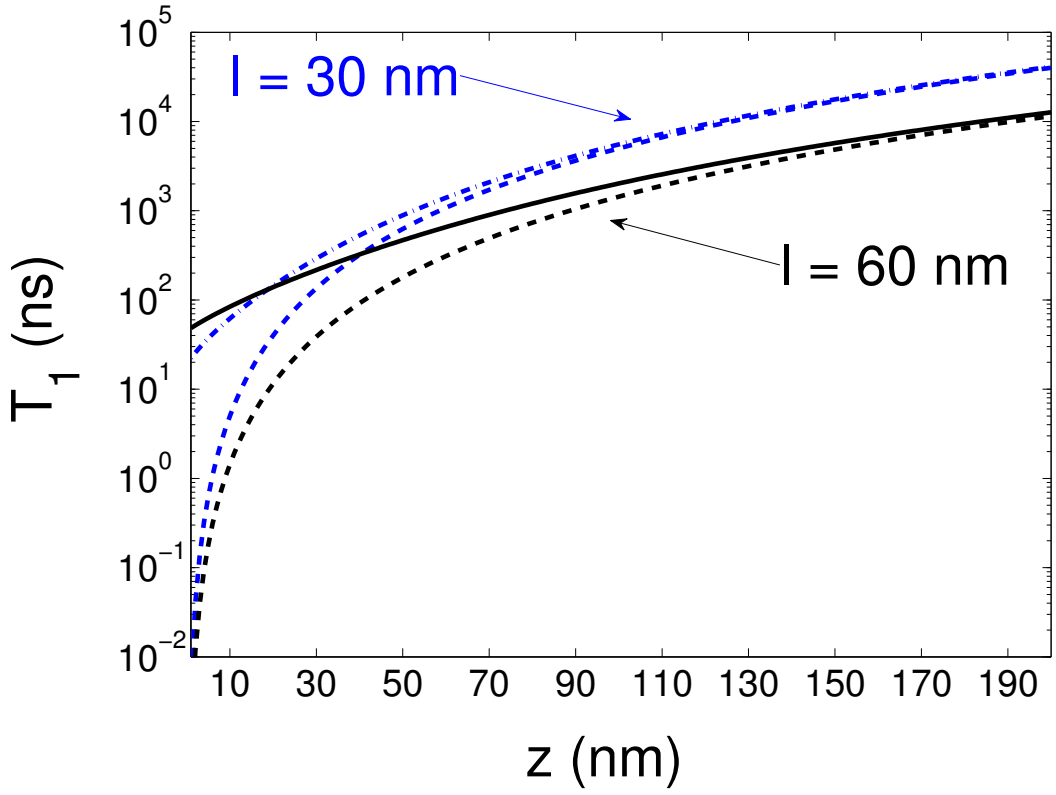

Figure 7.4: Energy relaxation time T_1 *vs.* the distance from the metallic gate to the DQDs z for dot geometry of $d = f = 30$ nm and $l = 30$ nm (dashed and dash-dotted blue lines) and 60 nm (solid and dashed black lines) at 0 K, $\omega/2\pi = 1$ GHz, and $\varepsilon = 0$. Solid and dash-dotted lines are T_1 times for the exact form of the interaction Hamiltonian, whereas dashed lines are for the dipole form of the interaction.

direction and do not consider excitations along the z-direction. We model the confining potential by a symmetric double rectangular well in 2D and numerically compute the lowest two eigenenergies and wavefunctions. We then compute the electron relaxation rate between these two lowest states. The results are qualitatively similar to the one-dimensional case and are shown in Fig. 7.4, where we plot the energy relaxation time T_1 *vs.* the distance z from the metallic gate to the DQD. In this plot, we choose the size of the dot in the x-direction $d = 30$ nm, the size in the y-direction $f = 30$ nm and half the separation between the dots l to be 30 nm (dashed and dash-dotted blue lines) and 60 nm (solid and dashed black lines). We find that for $l = 30$ nm and $z = 90$ nm, T_1 is $4\,\mu$s while for $l = 60$ nm, T_1 is roughly

1.6 μs. These relaxation times are somewhat longer than the experimentally reported value of $T_1 = 20$ ns in DQD-based charge qubits. [114, 137] We note that the relaxation rate for a two-dimensional DQD is shorter than for a one-dimensional DQD of comparable geometry by about a factor of 5. A two-dimensional DQD is able to couple to obliquely oriented wavevectors in addition to those which point in the direction of separation between the dots, and this can be reasonably expected to enhance relaxation by a geometric factor of order unity.

7.3 Spin qubit

We now focus on the calculation of the relaxation rate for a single electron in a spin qubit realized in a single quantum dot. Here the system H_s and the interaction H_{int} Hamiltonians are given by

$$H_s = -g\mu_B\, \vec{\sigma} \cdot \vec{B}_0/2 \tag{7.17}$$

$$H_{int} = -g\mu_B\, \vec{\sigma} \cdot \vec{B}(\vec{r}, t) \tag{7.18}$$

where $\vec{\sigma}$ is the vector of Pauli matrices, g is the gyrometric factor of the trapped electron in a quantum dot, μ_B is the Bohr magneton, $\vec{B}_0$ is the externally applied magnetic field and $\vec{B}(\vec{r}, t)$ is the fluctuating EWJN field. The rate of spin flip from excited $|\uparrow\rangle$ to ground $|\downarrow\rangle$ at $T = 0$ K can be obtained from the Fermi golden rule

$$\Gamma_{1,s} = \frac{1}{\hbar} \int d^3\vec{r} \int d^3\vec{r}\,' M_{r,s}(\vec{r})\, M_{r,s}(\vec{r}\,')\epsilon_{ijk}\epsilon_{ij'k'}\, \mathrm{Im}\, \chi^B_{kk'}(\vec{r}, \vec{r}\,', \omega) n_j n_{j'}\,, \tag{7.19}$$

where repeated indices are summed over, and n_j are the components of a unit vector $\hat{n}$ in the direction of $\vec{B}_0$. The effect of finite temperature on the transition rates is the same as for charge qubits, as shown in Eq. 7.11. The magnetic response function or susceptibility χ^B_{ij} and the matrix element $M_{r,s}(\vec{r})$ are

$$\chi^B_{ij}(\vec{r}, \vec{r}\,', \omega) = \frac{\varepsilon_{ikm}\varepsilon_{jnp}}{\epsilon_0 c^2} \partial_k \partial_n D_{mp}(\vec{r}, \vec{r}\,', \omega) \tag{7.20}$$

$$M_{r,s}(\vec{r}) \equiv g\mu_B |\psi_0(\vec{r})|^2\,. \tag{7.21}$$

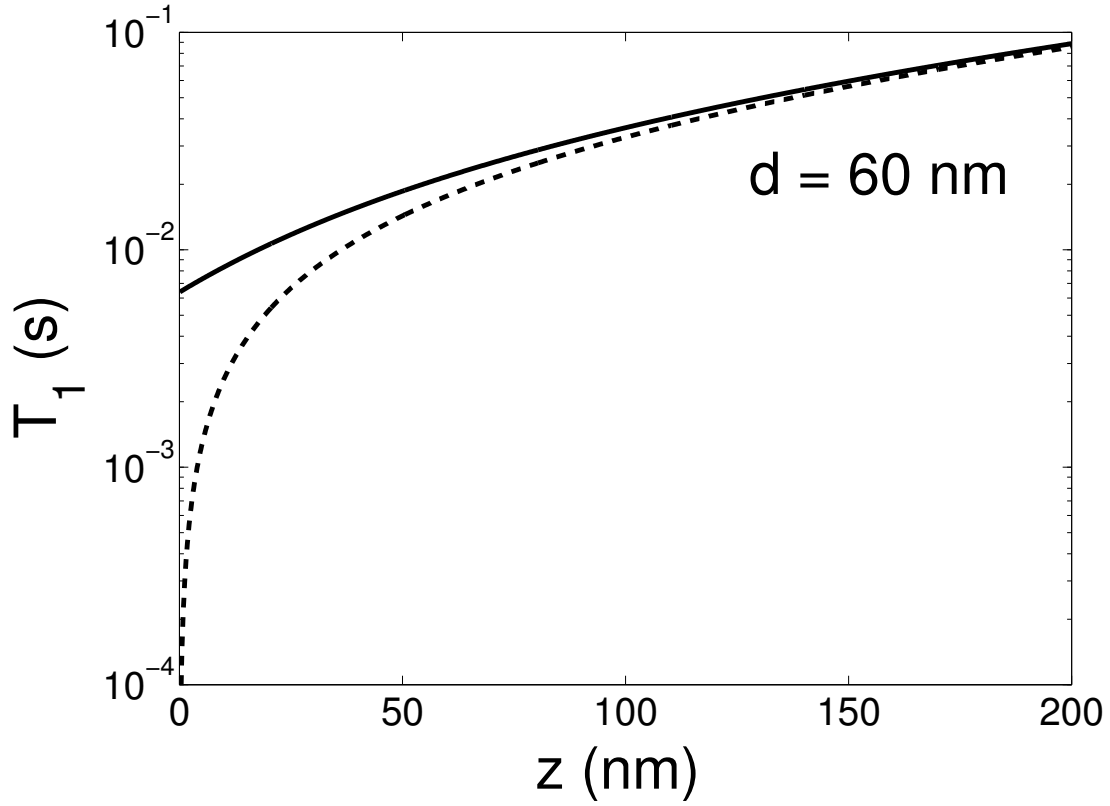

Figure 7.5: Energy relaxation time T_1 *vs.* the distance from the metallic gate to quantum dot z for spin qubit (in Si) single dot geometry of $d = 60$ nm at 0 K temperature and $g\mu_B B_0/2\pi\hbar = 50$ GHz. The solid line represent T_1 time for the exact form of the interaction Hamiltonian, whereas the dashed line is for the dipole form of the interaction.

Here the spin qubit frequency $\omega = g\mu_B B_0/\hbar$ and $\psi_0(\vec{r})$ is the spatial part of the the ground state wave function of the spin qubit. Eq. 7.19 is a generalization beyond the dipole approximation of the simpler expression[33]:

$$\Gamma_{1,s} = \frac{g^3\mu_B^3\sigma B_0}{16\pi\hbar^2\epsilon_0^2 c^4 z}, \tag{7.22}$$

which has been obtained by using the quasistatic limit for the Green's function 7.20, and assuming it is constant over the spatial extent of the qubit. Eq. 7.22 also assumes the external magnetic field $\vec{B}_0$ points in the z-direction.

A plot of energy relaxation time T_1 *vs.* the distance from the metallic gate z for a spin qubit is displayed in Fig. 7.5. Here we consider a single quantum dot of diameter $d = 60$

nm and approximate the ground state spatial wave function of the spin qubit by the ground state wave function of a harmonic potential. We assume the Zeeman splitting between spin states is 50 GHz, typical of experiments in spin qubits. [135] The solid line is the T_1 time obtained using the non-local magnetic spectral density while the dotted line is obtained for a local spectral density, which diverges as $\sim 1/z$ as one approaches the metallic gate. The reason for saturation of the T_1 time at smaller distances is similar to the case for charge qubits. There is a slight distinction in that the spin case involves a spatially extended dipole interaction, as opposed to the charge case which involves qenuine quadrupole and higher multipole contributions. This distinction is largely technical, however, and a saturation of T_1 as $z \to 0$ is observed in both cases.

We find that the T_1 time for a spin qubit in a GaAs quantum dot with an external magnetic field of 10 T and $z = 90$ nm is roughly 1 s which is larger than the experimentally reported value [135] of 0.55 ms, and generally EWJN does not seem to be the dominant source of decoherence for semiconductor devices in large magnetic fields. GaAs has a strong spin-orbit interaction (SOI), which mixes the Zeeman-split spin states with orbitally excited states. Spin relaxation can then occur via coupling of the qubit to piezoelectric phonon noise in the 2DEG layer. The relaxation rate from this mechanism scales as B^5 and is the dominant pathway for spin relaxation at large external magnetic fields $B > 1$ T [138, 139]. Additionally, Marquardt and Abalmassov [129] calculate relaxation of spin qubits from electric EWJN via the SOI. Again, mixing of the charge and spin states via the SOI allows spin relaxation to be induced from electric field fluctuations. They estimate the power spectrum of the Johnson noise using a lumped circuit model and found a B^3 dependence of the relaxation rate. Our treatment involves a direct coupling of the fluctuating magnetic field from the top gates with the spin states, and our rate scales linearly with the magnetic field. We therefore expect our relaxation pathway to dominate at low magnetic fields, and indeed while we predict a much slower relaxation rate than measured by Amasha *et. al* [138] for $B \sim 7$ T, at $B = 1$ T our results predict $T_1 \sim 5$ s which is comparable to their measured value of $T_1 = 1$ s. Additionally, in Si quantum dots with a 2 T external magnetic field and

$z = 50$ nm, we predict a T_1 time of 15 ms which is smaller than the experimentally reported value of 40 ms [134]. However, it must be kept in mind that we have so far considered the simpler top gate geometry of a conducting half-space rather than the thin layer of finger gates used in these experiments. In the next section we address modifications to our calculations that we expect from more realistic gate geometry.

7.4 Thin metallic gates

A conducting half-space is an analytically convenient gate geometry, but a poor approximation to the thin top gates commonly used in semiconductor devices. In this section we present an exact treatment of the behavior of EWJN in the vicinity of a metallic film of finite thickness. Changing the half-space to a thin film affects EWJN by modifying the reflection coefficients r_s and r_p. The power spectrum of the resultant EWJN is obtained by substituting these modified reflection coefficients into the photon Green's function 7.14, and the relaxation time of, e.g. a charge qubit, is obtained by plugging Eq. 7.14 into Eqs. 7.5 and 7.13. The modified reflection coefficients for a film of thickness a take the form

$$r_p(k,\omega,a) = \frac{\epsilon^2 q^2 - q_1^2}{q_1^2 + \epsilon^2 q^2 + 2iqq_1\epsilon\cot(q_1 a)} \tag{7.23}$$

$$r_s(k,\omega,a) = \frac{q^2 - q_1^2}{q^2 + q_1^2 + 2iqq_1\cot(q_1 a)}. \tag{7.24}$$

They differ significantly from the half-space result only when the thickness a is of the order or smaller than the skin depth δ, and they reduce to the half-space result for $a \gg \delta$. A derivation of Eqs. 7.23 and 7.24 is given in the Appendix. Eqs. 7.23 and 7.24 are exact, but for a good conductor they can be cast into a simpler approximate form

$$r_p(k,\omega,a) \approx \left(1 + \frac{2q_1}{\epsilon k}\cot\left(q_1 a\right)\right)^{-1} \tag{7.25}$$

$$r_s(k,\omega,a) \approx -\left(1 - \frac{2c^2 q_1 k}{\epsilon\omega^2}\cot(q_1 a)\right)^{-1}. \tag{7.26}$$

These expressions have been obtained by expanding Eqs. 7.23 and 7.24 for large imaginary ϵ and then taking the quasistatic approximation $q \to ik$. The first approximation

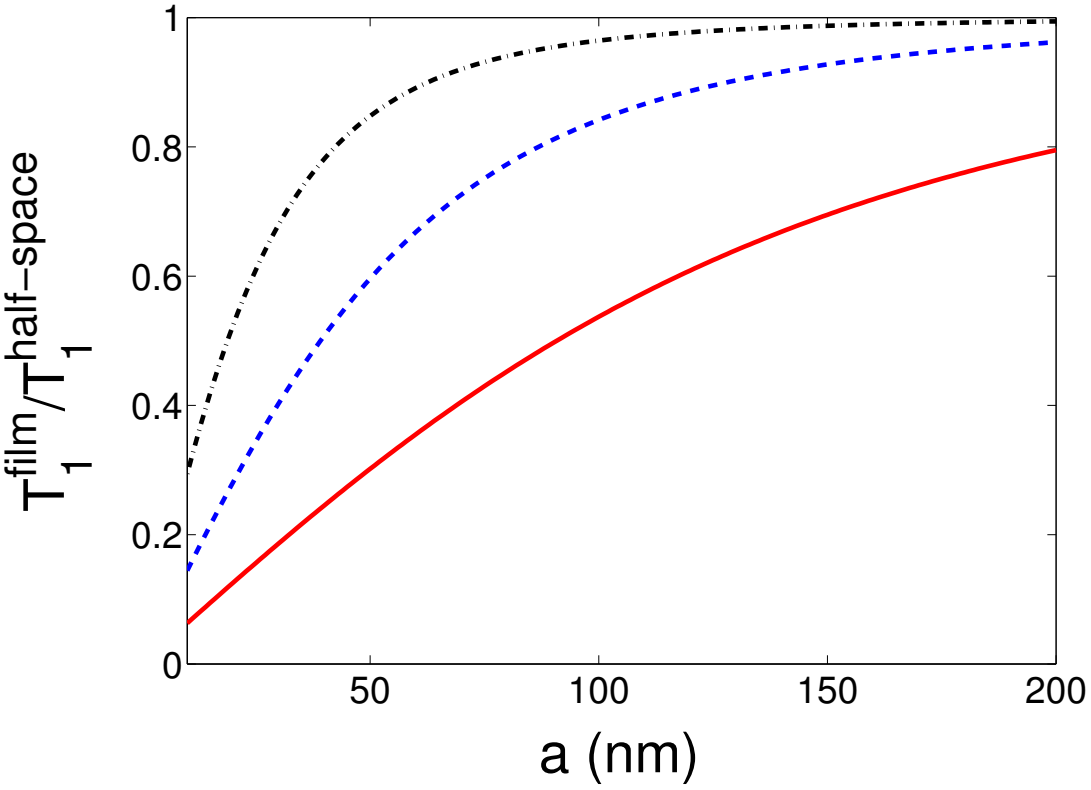

Figure 7.6: Ratio of energy relaxation time T_1 from conducting film to T_1 time from half-space *vs*. thickness of the film a for a DQD charge qubit in one dimension with dot geometry $d = 30$ nm and $l = 60$ nm at 0 K temperature. We take the exact form of the interaction Hamiltonian. The distance z from the film or half-space is chosen as follows: $z = 10$ nm (black dash-dotted line), $z = 50$ nm (blue dashed line) and $z = 150$ nm (solid red line). Other parameters are the same as in Fig. 7.2.

is extremely accurate for copper near zero temperature and the second is accurate for all distances z such that EWJN is appreciably enhanced above blackbody radiation [33]. The remarkable feature of Eqs. 7.25 and 7.26 is that they show the strength of the fluctuating fields outside the film are actually amplified relative to the half-space result. This can be understood by analogy to the behavior of a particle trapped in a finite one-dimensional potential well. For a given width of the well, the wavefunction will have an exponentially decaying tail in the forbidden region. As the confinement is increased, the particle will be squeezed and its wavefunction will leak farther into the forbidden region. It will be interesting to see if this enhancement is observable in the Casimir attraction between 2 thin

conducting plates.

Using the modified expression for the reflection coefficients, we compute the T_1 time of a DQD charge qubit in one dimension due to the metallic film. In Fig. 7.6, we plot the ratio of the T_1 time obtained for the film to the time computed for the metallic half-space as a function of the film thickness. We take the exact form of the interaction Hamiltonian for a variety of distances from the gate. We find that for distance $z > a$, the relaxation time due to the film can be reduced by over an order of magnitude relative to the half-space. It converges to the half-space result as z becomes smaller than the thickness of the film.

Common semiconductor qubit architectures employ thin finger-shaped top gates which are more sparse than the films considered here. An exact treatment of EWJN from a detailed finger gate geometry would be prohibitively difficult, but we expect to a reasonable approximation that EWJN from finger gates will be reduced by a factor of the fraction of the top gate layer that is not composed of metal. Our results should then overestimate the relaxation rate by a geometric factor. We note however that newer accumulation-mode architectures employ a second top gate above the confinement top gates [136]. These accumulation gates are solid sheets and are typically around 100 nm from the qubit, so our treatment should accurately describe their contribution to relaxation.

7.5 Discussion

In conclusion, we have presented a detailed study of the effect of evanescent-wave Johnson noise on energy relaxation of quantum dots beyond the dipole approximation. We have noted that previous studies of charge and spin qubits which use the dipole approximation allow contribution from infinitely large components of the photon wavevector leading to overestimation and divergence of the energy relaxation rate as $z \to 0$. We have demonstrated that it is possible to remedy this spurious divergence by taking into account the finite size of the quantum dot. While a non-local permittivity of the surface metal will remove the divergence in the field fluctuations at the boundary, we have shown that the finite size of the dot provides an alternative normalization mechanism by enforcing a finite

cutoff in the magnitude of the contributing wavevector. In addition, we have derived a novel enhancement of the EWJN field fluctuations that occurs outside a metallic film, relative to the field outside a metallic half-space.

This chapter has focused exclusively on relaxation, though we expect dephasing times from EWJN to be of comparable magnitude. The power spectrum of EWJN is linear in ω, and this will suppress contribution from the small frequency part of the electromagnetic spectrum, which typically enhances dephasing rates. While the temperature dependence of the relaxation rate is simply given by the Planck function, we do expect a more non-trivial temperature dependence of the dephasing rate.

Of particular interest are experimental signatures of EWJN-induced relaxation. Notably, at zero temperature the charge relaxation rate scales linearly with the qubit transition frequency and as the inverse cubic power of the distance between the qubit and the metallic top gates. The zero temperature spin relaxation rate scales linearly with the external magnetic field and inversely with the distance to the gates. Our results indicate that EWJN from the metallic top gate is not a dominant source of relaxation in charge qubits, but can be the dominant noise source for energy relaxation in spin qubits held at low external magnetic field.

Chapter 8

Conclusions

In this thesis, we have considered several aspects of superconducting and semiconducting qubits, exploring mainly the effect of decoherence on these devices. In the second chapter 2, we discuss different noise sources that plague semiconducting and superconducting qubits and present different methods we can use to study the dynamics of open quantum systems. In the third chapter 3, we investigate the effect of the Ohmic environment on optimally controlled phase qubit. Here we compare possible choices of microwave pulses for NOT gate operation. Specifically, we consider three options: single-quadrature pulses and two-quadrature microwave (control) pulses with both variable and fixed frequency. Two-quadrature pulses led to significant suppression of the gate error compared to single-quadrature pulses. However, the presence of dissipative environment increased the gate error even for two-quadrature pulses significantly above the required threshold for fault tolerant quantum computation in currently available phase qubits. We further investigate how the environmental coupling strength affects the gate error and found that an improvement of the qubit relaxation time is crucial for effectiveness of the DRAG pulses. We determine that two-quadrature pulses with fixed driving frequency suppress the gate error below the required threshold for a reasonable gate time of $7\,ns$, but for qubits with the relaxation time ten times longer than the currently observed relaxation time.

In chapter 4, we present a model to determine the quantum efficiency of a microwave

photon detector based on a current-biased JJ. We demonstrate that the efficiency to detect single photon loaded in a cavity is determined by relaxation and tunneling rates. We also determine that the bandwidth of the detector is characterized by the sum of the vacuum Rabi frequency and the broadening of the first excited state of the JJ due to tunneling and relaxation processes. Our results indicate that for currently used JJ photon detectors, the quantum efficiency of around 80% can be achieved even for modest junction parameters. In addition, we present alternative schemes for photon detection and present a systematic method to compute the power absorbed by the detector in such schemes.

In chapter 5, we discuss the effect of decoherence on the Berry curvature and present results which demonstrate that the curvature is immune to decoherence in non-adiabatic measurement protocols. Surprisingly, decoherence forces magnetization to respond linearly to the drive velocity in case of the sinusoidal drive, thereby assisting in the measurement of the Berry curvature. Furthermore, we analyze the prospect of measuring the Berry curvature in superconducting qubits. Here we investigate the effect of the third level in phase or transmon qubits on the measurement of the Berry curvature.

In the remaining chapters, we discuss the origin and effect of Johnson noise in semiconducting qubits. In chapter 6, we identify evanescent wave Johnson noise as an important source of decoherence in both spin and charge qubits. Here we carry out analysis within the dipole approximation of the qubit-field interaction. Finally, in chapter 7, we continue to discuss the effect of evanescent wave Johnson noise on extended qubit geometries. Here we go beyond the dipole approximation and present result for relaxation rates for both spin and charge qubits. We also consider the finite thickness nature of metallic gates and present enhancement of electric evanescent-wave Johnson noise compared to field fluctuations from extended gate geometry. These results serve as an important constraint on future device architectures.

Appendix A

Supplemental information for chapter 3

A.1 Hamiltonian of a flux-biased phase qubit

In this appendix, we detail the derivation of the Hamiltonian of a flux-biased phase qubit used in Eq. 3.2. The phase qubit consists of a superconducting loop interrupted by a Josephson junction. The Josephson junction consists of an insulating barrier sandwiched between two superconducting layers. In 1962, B.D. Josephson predicted that super current would tunnel through the insulating barrier even in the absence of applied voltage [140]. He showed that magnitude of super current I_s depends only on the phase difference δ (Josephson phase) between the order parameters of two superconducting electrodes. This is called the first Josephson equation which reads

$$I_s = I_0 \sin\delta \ , \tag{A.1}$$

where I_0 is the critical current of the junction. The second Josephson equation relates time evolution of the Josephson phase with the voltage drop V across the junction, that is,

$$\frac{d\delta}{dt} = 2e\frac{V}{\hbar} \ , \tag{A.2}$$

where h and e are Planck's constant and electronic charge, respectively. The dynamics of the phase qubit is best understood within a phenomenological resistively and capacitively shunted junction model (RCSJ) of a Josephson junction [141]. In a flux-biased phase qubit, biasing is done by coupling external flux to the superconducting loop, instead of directly injecting the bias current. This technique helps prevent, to some extent, noise in the bias circuitry to couple to the qubit.

Applying Kirchoff's law to the RCSJ circuit model along with Josephson equations and phase quantization condition in a superconductor, we obtain the following equation of motion,

$$C\left(\frac{\Phi_0}{2\pi}\right)^2\frac{d^2\delta}{dt^2}+\left(\frac{\Phi_0}{2\pi}\right)^2\frac{1}{R}\frac{d\delta}{dt}+\left(\frac{\Phi_0}{2\pi}\right)\frac{d}{d\delta}\left[\frac{\Phi_0}{4\pi L}\left(\delta-\frac{2\pi\Phi_b}{\Phi_0}\right)^2-I_0\cos\delta\right]=0\ , \quad \text{(A.3)}$$

where C, R and L are junction capacitance, shunt resistance and loop inductance, respectively. The parameters Φ_b and $\Phi_0 \equiv \frac{h}{2e}$ are external bias flux applied to the phase qubit and superconducting flux quantum, respectively. Eq. A.3 represents the equation of motion of a fictitious particle with mass $C\left(\frac{\Phi_0}{2\pi}\right)^2$ under the potential energy given by

$$U(\delta)=\frac{\Phi_0}{2\pi}\left[\frac{\Phi_0}{4\pi L}\left(\delta-\frac{2\pi\Phi_b}{\Phi_0}\right)^2-I_0\cos\delta\right]\ . \quad \text{(A.4)}$$

The parameter Φ_b can be tuned into appropriately to change the potential energy landscape of a flux-biased phase qubit. For instance, when $\Phi_b = \Phi_0$, the potential energy takes the shape of a symmetric double well. Typically, for the qubit operation, this parameter is tuned in between $0.95 - 0.98$ of Φ_c, where Φ_c is a critical flux of the qubit for which the second minimum in $U(\delta)$ disappears. With this expression for the potential energy, the Hamiltonian of a flux-biased phase qubit is given by:

$$H_q=\frac{Q^2}{2C}+\frac{\Phi_0}{2\pi}\left[\frac{\Phi_0}{4\pi L}\left(\delta-\frac{2\pi\Phi_b}{\Phi_0}\right)^2-I_0\cos\delta\right]\ . \quad \text{(A.5)}$$

Here Q corresponds to charge across the Josephson junction. Until now, charge and phase of the JJ were treated as classical variables. In order to study the quantum properties of the phase qubit, these variables must be promoted to operators. Hence, for a phase qubit, $\hat{Q}$ and $\hat{\delta}$ are treated as a conjugate momentum and position operators, respectively

that satisfy the commutation relationship $\left[\hat{Q}, \hat{\delta}\right] = i2e$. In $\delta-$representation, the operator $\hat{\delta} \to \delta$ and $\hat{Q} \to -2ie\frac{\partial}{\partial\delta}$. Therefore, in this representation, time-independent Schrodinger's equation takes the following form:

$$\frac{-2e^2}{C}\frac{\partial^2\psi}{\partial\delta^2} + \frac{\Phi_0}{2\pi}\left[\frac{\Phi_0}{4\pi L}\left(\delta - \frac{2\pi\Phi_b}{\Phi_0}\right)^2 - I_0\cos\delta\right]\psi(\delta) = E\psi(\delta)\ . \tag{A.6}$$

In the following section, we will outline a numerical method to solve this time-independent Schrodinger's equation.

A.2 Numerical solution of the Schrodinger's equation

Here we will detail the algorithm used to obtain the numerical solution of the time-independent Schrodinger's equation. The Schrodinger's equation is discretized over a one dimensional spatial interval $[\delta_0, \delta_N]$ of $N+2$ points such that $\delta_j = \delta_0 + j\epsilon$, where ϵ is the step size, and $j \in [0, N]$. The boundary conditions on wave functions over this interval are such that $\psi_n(\delta_0) = \psi_n(\delta_N) = 0$. On the discretized interval, time-independent Schrodinger's equation of the qubit system can be written as

$$A\psi_n^{''}(\delta_j) + \bar{U}(\delta_j)\psi_n(\delta_j) = \bar{E}_n\psi_n(\delta_j)\ , \quad \text{where} \tag{A.7}$$

$$\bar{U}(\delta_j) = A_1\left[\frac{1}{2}\left(\delta_j - \frac{2\pi\Phi_b}{\Phi_0}\right)^2 - \beta_L\cos(\delta_j)\right]\ . \tag{A.8}$$

Here, $A = -1$, $\bar{E_n} = -E_n/A_0$, $A_0 = -2e^2/C$, $A_1 = -\frac{\Phi_0^2}{4A_0\pi^2L}$ and $\beta_L = \frac{2\pi I_0 L}{\Phi_0}$. We have rescaled the potential and kinetic energy terms for numerical stability. The derivative in Eq. A.7 is approximated using the finite differences scheme as follows:

$$\psi_n^{''}(\delta_j) \approx \frac{-\psi_n(\delta_{j+2}) + 16\psi_n(\delta_{j+1}) - 30\psi_n(\delta_j) + 16\psi_n(\delta_{j-1}) - \psi_n(\delta_{j-2})}{12\epsilon^2} \tag{A.9}$$

The error in this approximation scheme is of the order of ϵ^4. With this approximation for the derivatives, evaluating Eq. A.7 at each discretized point, we obtain a system of $N-1$ linear equations, which can be written in a matrix form. The eigen functions and eigenvalues of this matrix are the desired energy eigenvalues and wave functions of the Schrodinger's equation.

Appendix B

Supplemental information for chapter 6

B.1 Derivation of Green's tensor for half space

In this appendix, we will derive Green's function for the metallic half space. We begin by calculating Green's function for parallel plate geometry in three spatial dimensions. Our starting point for the calculation of Green's function in the free space between two conducting half spaces of relative permittivities $\epsilon_1(\vec{r},\omega)$ and $\epsilon_2(\vec{r},\omega)$ in three dimensions will be:

$$\left(-\delta_{ij}\left(\nabla^2+\frac{\omega^2\epsilon(\vec{r},\omega)}{c^2}\right)+\partial_i\partial_j\right)D_{ik}(\vec{r},\vec{r}\,')=\delta^3(\vec{r}-\vec{r}\,')\delta_{jk} \tag{B.1}$$

The dependence of $D_{ik}(\vec{r},\vec{r}\,')$ on ω is suppressed to simplify notation. We take the boundaries of the two conducting half spaces to be located at $z=0$ and $z=l$, with vacuum for $0<z<l$. Because the geometry is translationally invariant in the x and y directions, we expand D_{ik} in a Fourier series for $x-x'$ and $y-y'$:

$$\tilde{D}_{ij}(\vec{k},z,z')=\int e^{-i\vec{k}\cdot\vec{z}_\parallel}D(\vec{r},\vec{r}\,')d^2\vec{z}_\parallel \tag{B.2}$$

$$D(\vec{r},\vec{r}\,')=\frac{1}{(2\pi)^2}\int e^{i\vec{k}\cdot\vec{z}_\parallel}\tilde{D}_{ij}(\vec{k},z,z')d^2\vec{k} \tag{B.3}$$

Here $\vec{\imath}_{\parallel} \equiv \vec{r}_{\parallel} - \vec{r'}_{\parallel} \equiv (x - x', y - y')$. After B.3 is plugged into B.1, the resulting set of differential equations will significantly decouple if we choose $\vec{k}$ to lie along the x-axis, i.e., choose $\vec{k} = (k, 0)$. Once this is done, B.1 reduces to

$$\left(\frac{\partial^2}{\partial z^2} + \frac{\omega^2\epsilon}{c^2}\right)\tilde{D}_{xj}(k,z,z') - ik\frac{\partial}{\partial z}\tilde{D}_{zj}(k,z,z') = \delta_{xj}\delta(z-z') \tag{B.4}$$

$$\left(-k^2 + \frac{\omega^2\epsilon}{c^2}\right)\tilde{D}_{zj}(k,z,z') - ik\frac{\partial}{\partial z}\tilde{D}_{xj}(k,z,z') = \delta_{zj}\delta(z-z') \tag{B.5}$$

$$\left(-k^2 + \frac{\partial^2}{\partial z^2} + \frac{\omega^2\epsilon}{c^2}\right)\tilde{D}_{yj}(k,z,z') = \delta_{yj}\delta(z-z') \tag{B.6}$$

Where $j = x, y, z$. Combining these equations we arrive at

$$\left(\frac{\partial^2}{\partial z^2} + q^2\right)\tilde{D}_{yy}(k,z,z') = \delta(z-z') \tag{B.7}$$

$$\left(\frac{\partial^2}{\partial z^2} + q^2\right)\tilde{D}_{xx}(k,z,z') = \frac{q^2c^2}{\omega^2\epsilon}\delta(z-z') \tag{B.8}$$

$$\tilde{D}_{zx}(k,z,z') = \frac{ik}{q^2}\frac{\partial}{\partial z}\tilde{D}_{xx}(k,z,z') \tag{B.9}$$

$$\tilde{D}_{zz}(k,z,z') = \frac{ik}{q^2}\frac{\partial}{\partial z}\tilde{D}_{xz}(k,z,z') + \frac{1}{q^2}\delta(z-z') \tag{B.10}$$

We solve first for $\tilde{D}_{yy}$; its boundary value problem is

$$\tilde{D}_{yy}(k,z,z') = \begin{cases} Ae^{-iq_1 z} & , \quad z < 0 \\ C_1 e^{-iqz} + C_2 e^{iqz} + \frac{1}{2\,i\,q}e^{iq|z-z'|} & , \quad 0 \le z < l \\ Be^{iq_2(z-l)} & , \quad l \le z \end{cases} \tag{B.11}$$

$$q^2 \equiv \omega^2/c^2 - k^2, \quad q_1^2 \equiv \epsilon_1\omega^2/c^2 - k^2, \quad q_2^2 \equiv \epsilon_2\omega^2/c^2 - k^2 \tag{B.12}$$

Since $\tilde{D}_{yy}$ and $\partial\tilde{D}_{yy}/\partial z$ must be continuous at the interfaces at $z = 0, l$, we can now determine the constants C_1 and C_2 to be

$$C_1 = \frac{i}{2q\triangle}\left(e^{iqz'} + \frac{q+q_1}{q-q_1}e^{-iqz'}\right) \tag{B.13}$$

$$C_2 = \frac{i}{2q\triangle}\left(e^{-iqz'} + \frac{q+q_2}{q-q_2}e^{iq(z'-2l)}\right) \tag{B.14}$$

$$\triangle \equiv 1 - \frac{(q+q_1)(q+q_2)}{(q-q_1)(q-q_2)}e^{-2iql} \tag{B.15}$$

We plug these back into $\tilde{D}_{yy}$ and obtain

$$\tilde{D}_{yy}(k,z,z') = \frac{-ci}{2\omega v \triangle}\left(\frac{v+\sqrt{\epsilon_1-u^2}}{v-\sqrt{\epsilon_1-u^2}}e^{-i\omega v(z+z')/c} + \frac{v+\sqrt{\epsilon_2-u^2}}{v-\sqrt{\epsilon_2-u^2}}e^{i\omega v(z+z'-2l)/c}\right) + \frac{ci}{2\omega v}\left(2\cos(\omega v[z-z']/c)/\triangle - e^{i\omega v|z-z'|/c}\right), \tag{B.16}$$

where we have introduced the definitions $q \equiv \omega\sqrt{1-u^2}/c \equiv \omega v/c$, $u = ck/\omega$, and

$$v = \begin{cases} \sqrt{1-u^2} & , \quad 0 < u < 1 \\ i\sqrt{u^2-1} & , \quad u > 1 \end{cases} \tag{B.17}$$

A similar calculation will yield $\tilde{D}_{xx}$, although the boundary conditions for this problem are $\tilde{D}_{xx}$ and $\epsilon/q^2(\partial\tilde{D}_{xx}/\partial z)$ continuous across the boundaries at $z = 0, l$. The result is

$$\tilde{D}_{xx}(k,z,z') = \frac{civ}{2\omega\triangle_1}\left(\frac{\epsilon_1 v+\sqrt{\epsilon_1-u^2}}{\epsilon_1 v-\sqrt{\epsilon_1-u^2}}e^{-i\omega v(z+z')/c} + \frac{\epsilon_2 v+\sqrt{\epsilon_2-u^2}}{\epsilon_2 v-\sqrt{\epsilon_2-u^2}}e^{i\omega v(z+z'-2l)/c}\right) + \frac{civ}{2\omega}\left(2\cos(\omega v[z-z']/c)/\triangle_1 - e^{i\omega v|z-z'|/c}\right) \tag{B.18}$$

$$\triangle_1 \equiv 1 - \frac{(\epsilon_1 v+\sqrt{\epsilon_1-u^2})(\epsilon_2 v+\sqrt{\epsilon_2-u^2})}{(\epsilon_1 v-\sqrt{\epsilon_1-u^2})(\epsilon_2 v-\sqrt{\epsilon_2-u^2})}e^{-2i\omega v l/c} \tag{B.19}$$

From Eqs. B.9 and B.10, $\tilde{D}_{zz}(k,z,z')$ is determined to be

$$\tilde{D}_{zz}(k,z,z') = -\frac{k^2}{q^2}\tilde{D}_{xx}(-k,z',z) \tag{B.20}$$

Next, we back Fourier transform to obtain these quantities in the real space. Eqs. B.16 and B.18 were obtained assuming that $\vec{k}$ lies entirely in the x direction. Because of spatial invariance in the $x-y$ plane, B.18 would be equal to $\tilde{D}_{yy}(k,z)$ if $\vec{k}$ were chosen to point in the y-direction. Eqs. B.16 and B.18 are then the contributions into the k_x and k_y Fourier components of $D_{yy}(\vec{r},\vec{r}\,',\omega)$, respectively. We can therefore construct

$$D_{yy}(\vec{r}_\parallel,z,\omega) = D_{xx}(\vec{r}_\parallel,z,\omega) = \frac{1}{(2\pi)^2}\int e^{i\vec{k}\cdot\vec{r}_\parallel}\left(\tilde{D}_{yy}(k,z,\omega)\sin^2\theta + \tilde{D}_{xx}(k,z,\omega)\cos^2\theta\right)d^2\vec{k} \tag{B.21}$$

The exponential term vanishes in the limit $\vec{r} \to \vec{r}\,'$, and the angular integration simply gives a factor of π. The trigonometric factors are squared because the Green's function is related to the expectation value of the square of the electric field.

$$D_{yy}(\vec{r}_\parallel,z,\omega) = D_{xx}(\vec{r}_\parallel,z,\omega) = \frac{1}{4\pi}\int_0^\infty\left(\tilde{D}_{yy}(k,z,\omega)+\tilde{D}_{xx}(k,z,\omega)\right)kdk \tag{B.22}$$

Meanwhile the integral expression for $D_{zz}(\vec{r}_{\parallel}, z, \omega)$ may be trivially derived and is equal to

$$D_{zz}(\vec{r}_{\parallel}, z, \omega) = \frac{1}{2\pi} \int_0^{\infty} \frac{k^3}{q^2} \tilde{D}_{xx}(k, z, z')dk \tag{B.23}$$

The case of a half space can be obtained from B.22 by taking the limit $l \to \infty$ in the evanescent range of q (when it is imaginary):

$$\lim_{l\to\infty} \tilde{D}_{yy}(k, z) \mid_{k>\omega/c} = \frac{ci}{2\omega v} \left(\frac{v - \sqrt{\epsilon_1 - u^2}}{v + \sqrt{\epsilon_1 - u^2}} e^{2i\omega v z/c} + 1 \right) \tag{B.24}$$

$$\lim_{l\to\infty} \tilde{D}_{xx}(k, z) \mid_{k>\omega/c} = \frac{-civ}{2\omega} \left(\frac{\epsilon_1 v - \sqrt{\epsilon_1 - u^2}}{\epsilon_1 v + \sqrt{\epsilon_1 - u^2}} e^{2i\omega v z/c} - 1 \right) \tag{B.25}$$

This leads to the following expression for $D^{hs}_{xx,yy}$:

$$D^{(hs)}_{yy}(\vec{r}_{\parallel}, z, \omega) = D^{(hs)}_{xx}(\vec{r}_{\parallel}, z, \omega) = \frac{i\omega}{8\pi c} \int_0^{\infty} \frac{udu}{v} \left(e^{2i\omega v z/c} \left(r_s(u) + (u^2 - 1) r_p(u) \right) + 2 - u^2 \right), \tag{B.26}$$

where we have introduced

$$r_p(u) = \frac{\epsilon v - \sqrt{\epsilon - u^2}}{\epsilon v + \sqrt{\epsilon - u^2}} \quad \text{and} \quad r_s(u) = \frac{v - \sqrt{\epsilon - u^2}}{v + \sqrt{\epsilon - u^2}}. \tag{B.27}$$

r_p is the reflection coefficient for the part of the electric field perpendicular to the plane of incidence and r_s is the reflection coefficient for the part of the electric field parallel to the plane of incidence. The imaginary part of the response function (near-field only) is given by

$$\begin{aligned} \operatorname{Im} \chi^E_{xx}(\vec{r}, \vec{r}', \omega) &= \frac{\omega^2}{\epsilon_0 c^2} \operatorname{Im} D^{(hs)}_{xx}(\vec{r}_{\parallel}, z, \omega) \\ &= \frac{\omega^3}{8\pi\epsilon_0 c^3} \operatorname{Re} \int_0^{\infty} \frac{udu}{v} e^{2i\omega v z/c} \Big(r_s(u) + (u^2 - 1) r_p(u) \Big) \end{aligned} \tag{B.28}$$

Appendix C

Supplemental information for chapter 7

C.1 Derivation of generalized Fermi's golden rule

In this appendix, we will derive the generalized Fermi's golden rule used in Eq. 7.5. Consider a system-bath interaction Hamiltonian

$$H_{SB} = -\frac{e}{2m^*}\left(\vec{A}(\vec{r})\cdot\vec{p}+\vec{p}\cdot\vec{A}(\vec{r})\right). \tag{C.1}$$

Since $\left[\vec{p},\vec{A}(\vec{r})\right] = -i\hbar\nabla\cdot\vec{A}(\vec{r})$, the interaction Hamiltonian can be written as: $H_{SB} = -\frac{e}{m^*}\vec{A}(\vec{r})\cdot\vec{p} + \frac{ie\hbar}{2m^*}\nabla\cdot\vec{A}(\vec{r})$. The relaxation rate for $|-\rangle \longrightarrow |+\rangle$ transition at zero temperature can be calculated using the Fermi's golden rule. To calculate the total relaxation rate, we have to sum over all initial reservoir states weighted with the probability to find these states and over all final reservoir states, namely :

$$\begin{aligned}\Gamma_{-\to+} =& \frac{2\pi e^2}{m^{*2}\hbar}\sum_{ij}\sum_{R'R}\frac{1}{2}\Big[\langle R',\psi_+|A_i(\vec{r})p_i - i\hbar/2\partial_i A_i(\vec{r})|\psi_-,R\rangle^*\langle R',\psi_+|A_j(\vec{r'})p_j \\ & - i\hbar/2\partial_j A_j(\vec{r'})|\psi_-,R\rangle + i\leftrightarrow j\Big]P(R)\,\delta(\varepsilon_- + \varepsilon_R - \varepsilon_+ - \varepsilon_{R'}),\end{aligned} \tag{C.2}$$

where $\varepsilon_\pm$ are energies of $|\pm\rangle$ states, $|R\rangle(|R'\rangle)$ are reservoir initial (final) states respectively, and $P(R)$ is the probability to find the reservoir in initial state R. Next, rewrite the delta

function in terms of its Fourier transform

$$\delta(\varepsilon_- + \varepsilon_R - \varepsilon_+ - \varepsilon_{R'}) = \frac{1}{2\pi\hbar}\int d(t-t')\, e^{i\omega(t-t')}\, e^{i\frac{\varepsilon_R - \varepsilon_{R'}}{\hbar}(t-t')}, \quad \text{where } \omega \equiv (\varepsilon_- - \varepsilon_+)/\hbar\,,$$

and introduce time-dependent Heisenberg operator $\vec{A}(\vec{r},t)$ to obtain

$$\begin{aligned}
\Gamma_{-\to+} = \frac{1}{2}\Big[&\frac{e^2}{m^{*2}\hbar^2}\sum_{ij}\int d\vec{r}\,\psi_+(\vec{r})\,(i\hbar)\partial_i\psi_-^*(\vec{r})\int d\vec{r}'\,\psi_+^*(\vec{r}')\,(-i\hbar)\partial_j\psi_-(\vec{r}') \\
&\times\sum_{R'R}P(R)\int\langle R'|A_i(\vec{r},t)|R\rangle^*\langle R'|A_j(\vec{r}',t')|R\rangle\, e^{i\omega(t-t')}\,d(t-t') \quad + \\
&\frac{e^2}{m^{*2}\hbar^2}\sum_{ij}\int d\vec{r}\,\psi_+(\vec{r})\,(i\hbar)\partial_i\psi_-^*(\vec{r})\int d\vec{r}'\,\psi_+^*(\vec{r}')\psi_-(\vec{r}') \\
&\times(-i\hbar)\partial_j\sum_{R'R}P(R)\int\langle R'|A_i(\vec{r},t)|R\rangle^*\langle R'|A_j(\vec{r}',t')|R\rangle\, e^{i\omega(t-t')}\,d(t-t') \quad + \\
&\frac{e^2\hbar^2}{4m^{*2}\hbar^2}\sum_{ij}\int d\vec{r}\,\psi_+(\vec{r})\,\psi_-^*(\vec{r})\int d\vec{r}'\,\psi_+^*(\vec{r}')\,\psi_-(\vec{r}') \\
&\times\partial_i\partial_j\sum_{R'R}P(R)\int\langle R'|A_i(\vec{r},t)|R\rangle^*\langle R'|A_j(\vec{r}',t')|R\rangle\, e^{i\omega(t-t')}\,d(t-t') + i\leftrightarrow j\Big]\,.
\end{aligned}$$

This expression can be simplified further by using the completeness relation for the reservoir final states and the following definition of the equilibrium cross correlation function

$$\langle\{A_i(\vec{r},t)\,,A_j(\vec{r}',t')\}\rangle = \sum_R P(R)\langle R|\{A_i(\vec{r},t)\,,A_j(\vec{r}',t')\}|R\rangle\,, \quad \text{and its Fourier transform}$$

$$\int e^{i\omega\tau}\frac{1}{2}\langle\{A_i\left(\vec{r},\tau\right)\,,A_j\left(\vec{r}',0\right)\}\rangle\; d\tau \equiv S_{ij}\left(\vec{r},\vec{r}',\omega\right)\,, \quad \text{where } \{\,,\} \text{ is anticommutator.}$$

Here S_{ij} is the spectral density of the vector potential. This simplifies the above expression for the relaxation rate to

$$\begin{aligned}
\Gamma_{-\to+} = &\frac{e^2}{m^{*2}\hbar^2}\sum_{ij}\int d\vec{r}\,\psi_+(\vec{r})\,(i\hbar)\partial_i\psi_-^*(\vec{r})\int d\vec{r}'\,\psi_+^*(\vec{r}')\,(-i\hbar)\partial_j\psi_-(\vec{r}')\;S_{ij}\left(\vec{r},\vec{r}',\omega\right) \quad - \\
&\frac{e^2}{m^{*2}\hbar^2}\sum_{ij}\int d\vec{r}\,\psi_+(\vec{r})\,(i\hbar)\partial_i\psi_-^*(\vec{r})\int d\vec{r}'\,\psi_+^*(\vec{r}')\psi_-(\vec{r}')\,(-i\hbar)\partial_j S_{ij}\left(\vec{r},\vec{r}',\omega\right) \quad - \\
&\frac{e^2\hbar^2}{4m^{*2}\hbar^2}\sum_{ij}\int d\vec{r}\,\psi_+(\vec{r})\,\psi_-^*(\vec{r})\int d\vec{r}'\,\psi_+^*(\vec{r}')\,\psi_-(\vec{r}')\;\partial_i\partial_j S_{ij}\left(\vec{r},\vec{r}',\omega\right)\,. \qquad \text{(C.3)}
\end{aligned}$$

The above expression can also be written compactly as

$$\Gamma_{-\to+} = \frac{1}{\hbar^2}\sum_{ij}\int d\vec{r}\int d\vec{r'}\, M_r^{*i}(\vec{r})\, M_r^j(\vec{r'}) S_{ij}(\vec{r},\vec{r'},\omega)\,, \text{where } \vec{M}_r(\vec{r}) \text{ is defined as}$$

$$\vec{M}_r(\vec{r}) \equiv \frac{e}{m^*}\psi_+^*(\vec{r})\,\vec{p}\,\psi_-(\vec{r}) - \frac{ie\hbar}{2m^*}\psi_+^*(\vec{r})\,\psi_-(\vec{r})\,\nabla\,.$$

C.2 Derivation of Green's tensor for a thin film

Here we present the calculation for the retarded photon Green's tensor outside of a thin conducting sheet of permittivity ϵ. Green's function will satisfy Eq. B.1. Here $\vec{r}\,'$ is simply a parameter for the purposes of solving this set of equations, and we take it to lie in the vacuum outside the conducting sheet. We will suppress the dependence of $D_{ik}(\vec{r},\vec{r}\,',\omega)$ on $\vec{r}\,'$ and ω to simplify the notation. The geometry of the problem is contained entirely in the permittivity function $\varepsilon\,(\vec{r},\omega)$. We take the boundaries of the conducting sheet to be located at $z=-a$ and $z=0$, with vacuum outside. Because the geometry is still translationally invariant in the x and y directions, we employ the same Fourier expansion of Eq. 7.13 as in Section 7.2. Solving Eq. B.1 for a problem with planar symmetry is greatly simplified by separately considering the Fourier components of Eq. 7.13 that are polarized in the x and y directions. $\tilde{D}_{yy}(\vec{r})$ may then be reconstructed as

$$D_{yy}(\vec{r}) = \int \frac{d^2\vec{k}}{(2\pi)^2} e^{i\vec{k}\cdot\vec{z}_\parallel}\left(\tilde{D}_{yy,k_x}(k,z)\cos^2\theta + \tilde{D}_{yy,k_y}(k,z)\sin^2\theta\right)\,, \tag{C.4}$$

where $\tilde{D}_{yy,k_x} = \tilde{D}_{yy}$ when $k_y = 0$, and $\tilde{D}_{yy,k_y} = \tilde{D}_{yy}$ when $k_x = 0$. The boundary value problem for $\tilde{D}_{yy,k_x}(k,z)$ then becomes

$$\tilde{D}_{yy,k_x}(k,z) = \begin{cases} Ae^{-iqz} & , \quad z < -a \\ B_1 e^{-iq_1 z} + B_2 e^{iq_1 z} & , \quad -a \le z < 0 \\ Ce^{iqz} + \frac{1}{2\,iq}e^{iq|z-z'|} & , \quad z \ge 0 \end{cases} \tag{C.5}$$

Our interest lies in the behavior of the fields for $z > 0$, so we need only to calculate C. Enforcing that D_{yy,k_x} and $\partial D_{yy,k_x}/\partial z$ are continuous across the boundaries results in

$$C = \frac{i}{2q} r_s(k,\omega,a) e^{iqz'}\,, \tag{C.6}$$

where

$$r_s(k,\omega,a) \equiv \frac{\left(q^2-q_1^2\right)\sin(q_1 a)}{\left(q_1^2+q^2\right)\sin(q_1 a)+2iqq_1\cos(q_1 a)} = 2i\sin q_1 a\left(e^{iq_1 a}\frac{q-q_1}{q+q_1}-e^{-iq_1 a}\frac{q+q_1}{q-q_1}\right)^{-1} \tag{C.7}$$

so that

$$\tilde{D}_{yy,k_x}(k,z) = \frac{i}{2q}\left(r_s(k,\omega,a)e^{iq(z+z')}+e^{iq|z-z'|}\right). \tag{C.8}$$

The term proportional to $\exp(iq|z-z'|)$ is the free photon contribution to the power spectrum. It will have an imaginary component and thus contribute to relaxation only in the radiative regime, $k \leq \omega/c$. Within a skin depth of separation from the metal, evanescent waves are orders of magnitude larger in field strength than these free photons. They may be safely ignored in this context. A similar calculation yields the result for $\tilde{D}_{yy,k_y}$:

$$\tilde{D}_{yy,k_y}(k,z) = -\frac{ic^2 q}{2\omega^2}\left(r_p(k,\omega,a)e^{iq(z+z')}-e^{iq|z-z'|}\right), \tag{C.9}$$

where

$$r_p(k,\omega,a) \equiv \frac{\left(\epsilon^2 q^2-q_1^2\right)\sin(q_1 a)}{\left(q_1^2+\epsilon^2 q^2\right)\sin(q_1 a)+2iqq_1\epsilon\cos(q_1 a)} = 2i\sin q_1 a\left(e^{iq_1 a}\frac{\epsilon q-q_1}{\epsilon q+q_1}-e^{-iq_1 a}\frac{\epsilon q+q_1}{\epsilon q-q_1}\right)^{-1}. \tag{C.10}$$

A Taylor expansion of Eqs. C.7 and C.10 for large a in the evanescent range of wavevectors, i.e., a Taylor expansion in powers of $\exp(-2|q_1|a)$, gives a monotonically increasing function of film thickness, a. However, a more careful treatment reveals that this is an error. The naive expansions of C.7 and C.10 for large a neglect an enhancement of the field spectrum that occurs for small k. In fact, EWJN is enhanced as the thickness is decreased for any good conductor. Specifically, the enhancement is preserved for a particular spatial Fourier component of the Green's function as long as $|\frac{2q_1}{\epsilon k}| < 1$. EWJN will eventually vanish as $a \to 0$, but this does not occur until an unphysically small thickness is reached, on the order of 10^{-14} m for copper at $T = 0K$ which is well below the applicability of the local permittivity model.

Bibliography

[1] R. P. Feynman, "Simulating physics with computers," *Int. J. Theor. Phys.*, vol. 21, no. 6/7, p. 467, 1982.

[2] D. Deutsch, "Quantum theory, the church-turing principle and the universal quantum computer," *Proc. R. Soc. Lond. A*, vol. 400, pp. 97–117, 1985.

[3] P. W. Shor, "Polynomial-time algorithms for prime factorization and discrete logarithms on a quantum computer," *SIAM J. Comput.*, vol. 26, p. 1484, 1997.

[4] L. K. Grover, "Quantum mechanics helps in searching for a needle in a haystack," *Phys. Rev. Lett.*, vol. 79, p. 325, 1997.

[5] M. A. Nielsen and I. L. Chuang, *Quantum Computation and Quantum Information*. Cambridge University Press, 2000.

[6] J. I. Cirac and P. Zoller, "Quantum computations with cold trapped ions," *Phys. Rev. Lett.*, vol. 74, p. 4091, 1995.

[7] C. Monroe, D. M. Meekhof, B. E. King, W. M. Itano, and D. J. Wineland, "Demonstration of a fundamental quantum logic gate," *Phys. Rev. Lett.*, vol. 75, p. 4714, 1995.

[8] H.-J. Briegel, T. Calarco, D. Jaksch, J. I. Cirac, and P. Zoller, "Quantum computing with neutral atoms," *Journal of Modern Optics*, vol. 47, p. 415, 2000.

[9] G. K. Brennen, C. M. Caves, P. S. Jessen, and I. H. Deutsch, "Quantum logic gates in optical lattices," *Phys. Rev. Lett.*, vol. 82, p. 1060, 1999.

[10] E. Knill, R. Laflamme, and G. J. Milburn, "A scheme for efficient quantum computation with linear optics," *Nature*, vol. 409, p. 46, 2001.

[11] B. E. Kane, "A silicon-based nuclear spin quantum computer," *Nature*, vol. 393, p. 133, 2001.

[12] A. P. Nizovtsev, S. Y. Kilin, F. Jelezko, T. Gaebal, I. Popa, A. Gruber, and J. Wrachtrup, "A quantum computer based on nv centers in diamond: Optically detected nutations of single electron and nuclear spins," *Opt. Spectrosc.*, vol. 99, p. 233, 2005.

[13] D. Loss and P. D. DiVincenzo, "Quantum computation with quantum dots," *Phys. Rev. A*, vol. 57, p. 120, 1998.

[14] J. Clarke and F. K. Wilhelm, "Superconducting quantum bits," *Nature*, vol. 453, p. 1031, 2008.

[15] L. Chirolli and G. Burkard, "Decoherence in solid-state qubits," *Advances in Physics*, vol. 57, p. 225, 2008.

[16] J. M. Martinis, K. B. Cooper, R. McDermott, M. Steffen, M. Ansmann, K. D. Osborn, K. Cicak, S. Oh, D. P. Pappas, R. W. Simmonds, and C. C. Yu, "Decoherence in josephson qubits from dielectric loss," *Phys. Rev. Lett.*, vol. 95, p. 210503, 2005.

[17] D. A. Lidar, I. L. Chuang, and K. B. Whaley, "Decoherence-free subspaces for quantum computation," *Phys. Rev. Lett.*, vol. 81, p. 2594, 1998.

[18] S. D. Sarma, M. Freedman, and C. Nayak, "Topologically-protected qubits from a possible non-abelian fractional quantum hall state," *Phys. Rev. Lett.*, vol. 94, no. 166802, 2005.

[19] A. Stern and N. H. Lindner, "Topological quantum computation—from basic concepts to first experiments," *Science*, vol. 339, p. 1179, 2013.

[20] E. Knill and R. Laflamme, "Theory of quantum error-correcting codes," *Phys. Rev. A*, vol. 55, p. 900, 1997.

[21] L. Viola, E. Knill, and S. Lloyd, "Dynamical decoupling of open quantum systems," *Phys. Rev. Lett.*, vol. 82, no. 2417, 1999.

[22] D. Gottesman, "Theory of fault-tolerant quantum computation," *Phys. Rev. A*, vol. 57, p. 127, 1998.

[23] H. K. Lo, S. Popescu, and T. P. Spiller, eds., *Introduction to Quantum Computation and Information*. World Scientific Publishing Co. Pte. Ltd, 1998.

[24] Y. Liu, L. F. Wei, and F. Nori, "Generation of nonclassical photon states using a superconducting qubit in a microcavity," *Europhys. Lett.*, vol. 67, p. 941, 2004.

[25] M. Hofheinz, E. Weig, M. Ansmann, R. C. Bialczak, E. Lucero, M. Neeley, A. D. O'Connell, H. Wang, J. M. Martinis, and A. N. Cleland, "Generation of fock states in a superconducting quantum circuit," *Nature*, vol. 454, p. 310, 2008.

[26] J. Majer, J. M. Chow, J. M. Gambetta, J. Koch, B. R. Johnson, J. A. Schreier, L. Frunzio, D. I. Schuster, A. A. Houck, A. Wallraff, A. Blais, M. H. Devoret, S. M. Girvin, and R. J. Schoelkopf, "Coupling superconducting qubits via a cavity bus," *Nature*, vol. 449, p. 443, 2007.

[27] M. D. Eisaman, J. Fan, A. Migdall, and S. V. Polyakov, "Single-photon sources and detectors," *Rev. Sci. Instrum.*, vol. 82, p. 071101, 2011.

[28] A. Ekert, M. Ericsson, P. Hayden, H. Inamori, J. A. Jones, D. K. L. Oi, and V. Vedral, "Geometric quantum computation," *J. Mod. Opt.*, vol. 47, p. 2501, 2000.

[29] P. J. Leek, J. M. Fink, A. Blais, R. Bianchetti, M. Goppl, J. M. Gambetta, D. I. Schuster, L. Frunzio, R. J. Schoelkopf, and A. Wallraff, "Observation of berry's phase in a solid-state qubit," *Science*, vol. 318, p. 1889, 2007.

[30] V. Gritsev and A. Polkovnikov, "Dynamical quantum hall effect in the parameter space," *PNAS*, vol. 109, p. 6457, 2012.

[31] A. Poudel and M. G. Vavilov, "Effect of an ohmic environment on an optimally controlled flux-biased phase qubit," *Phys. Rev. B*, vol. 82, p. 144528, 2010.

[32] A. Poudel, R. McDermott, and M. G. Vavilov, "Quantum efficiency of a microwave photon detector based on a current-biased josephson junction," *Phys. Rev. B*, vol. 86, p. 174506, 2012.

[33] L. S. Langsjoen, A. Poudel, M. G. Vavilov, and R. Joynt, "Qubit relaxation from evanescent-wave johnson noise," *Phys. Rev. A*, vol. 86, p. 010301(R), 2012.

[34] A. Poudel, L. S. Langsjoen, M. G. Vavilov, and R. Joynt, "Relaxation in quantum dot due to evanescent-wave johnson noise from a metallic backgate," *Phys. Rev. B*, vol. 87, p. 045301, 2013.

[35] M. H. Devoret and J. M. Martinis, "Implementing qubits with superconducting integrated circuits," *Quantum Inf. Process.*, vol. 3, p. 163, 2004.

[36] M. Constantin and C. C. Yu, "Microscopic model of critical current noise in josephson junctions," *Phys. Rev. Lett.*, vol. 99, p. 207001, 2007.

[37] R. Sousa, K. B. Whaley, T. Hecht, J. Delft, and F. K. Wilhelm, "Microscopic model of critical current noise in josephson-junction qubits: Subgap resonances and andreev bound states," *Phys. Rev. B*, vol. 80, p. 094515, 2009.

[38] E. Paladino, L. Faoro, G. Falci, and R. Fazio, "Decoherence and $1/f$ noise in josephson qubits," *Phys. Rev. Lett.*, vol. 88, p. 228304, 2002.

[39] L. Faoro, J. Bergli, B. L. Altshuler, and Y. M. Galperin, "Models of environment and t1 relaxation in josephson charge qubits," *Phys. Rev. Lett.*, vol. 95, p. 046805, 2005.

[40] R. W. Simmonds, K. M. Lang, D. A. Hite, S. Nam, D. P. Pappas, and J. M. Martinis, "Decoherence in josephson phase qubits from junction resonators," *Phys. Rev. Lett.*, vol. 93, p. 077003, 2004.

[41] S. Sendelbach, D. Hover, A. Kittel, M. Muck, J. M. Martinis, and R. McDermott, "Magnetism in squids at millikelvin temperatures," *Phys. Rev. Lett.*, vol. 100, p. 227006, 2008.

[42] L. Faoro and L. B. Ioffe, "Microscopic origin of low-frequency flux noise in josephson circuits," *Phys. Rev. Lett.*, vol. 100, p. 227005, 2008.

[43] T. Fujisawa, T. Hayashi, and S. Sasaki, "Time-dependent single-electron transport through quantum dots," *Rep. Prog. Phys.*, vol. 69, p. 759, 2006.

[44] T. Fujisawa, T. Hayashi, H. D. Cheong, Y. H. Jeong, and Y. Hirayama, "Rotation and phase-shift operations for a charge qubit in a double quantum dot," *Physica E*, vol. 21, p. 1046, 2004.

[45] X. Hu, B. Koiller, and S. D. Sarma, "Charge qubits in semiconductor quantum computer architecture: Tunnel coupling and decoherence," *Phys. Rev. B*, vol. 71, p. 235332, 2005.

[46] S. W. Jung, T. Fujisawa, Y. Hirayama, and Y. H. Jeong, "Background charge fluctuation in a gaas quantum dot device," *Appl. Phys. Lett.*, vol. 85, p. 768, 2004.

[47] Y. A. Pashkin, O. Astafiev, T. Yamamoto, Y. Nakamura, and J. S. Tsai, "Josephson charge qubits: a brief review," *Quantum Inf. Process.*, vol. 8, p. 55, 2009.

[48] Z. Shi, C. B. Simmons, D. R. Ward, J. R. Prance, R. T. Mohr, T. S. Koh, J. K. Gamble, X. Wu, D. E. Savage, M. G. Lagally, M. Friesen, S. N. Coppersmith, and M. A. Eriksson, "Coherent quantum oscillations in a silicon charge qubit," *arXiv:1208.0519*, 2012.

[49] I. V. Yurkevich, J. Baldwin, I. V. Lerner, and B. L. Altshuler, "Decoherence of charge qubit coupled to interacting background charges," *Phys. Rev. B*, vol. 81, p. 121305, 2010.

[50] S. Vorojtsov, E. R. Mucciolo, and H. U. Baranger, "Phonon decoherence of a double quantum dot charge qubit," *Phys. Rev. B*, vol. 71, p. 205322, 2005.

[51] D. C. B. Valente, E. R. Mucciolo, and F. K. Wilhelm, "Decoherence by electromagnetic fluctuations in double-quantum-dot charge qubits," *Phys. Rev. B*, vol. 82, p. 125302, 2010.

[52] D. P. DiVincenzo, D. Bacon, J. Kempe, G. Burkard, and K. B. Whaley, "Universal quantum computation with the exchange interaction," *Nature*, vol. 408, p. 339, 2000.

[53] M. Friesen, C. Tahan, R. Joynt, and M. A. Eriksson, "Spin readout and initialization in a semiconductor quantum dot," *Phys. Rev. Lett.*, vol. 92, p. 037901, 2004.

[54] C. Tahan, M. Friesen, and R. Joynt, "Decoherence of electron spin qubits in si-based quantum computers," *Phys. Rev. B*, vol. 66, p. 035314, 2002.

[55] R. Hanson, L. P. Kouwenhoven, J. R. Petta, S. Tarucha, and L. M. K. Vandersypen, "Spins in few-electron quantum dots," *Rev. Mod. Phys.*, vol. 79, p. 1217, 2007.

[56] A. V. Khaetskii, L. Loss, and L. Glazman, "Electron spin decoherence in quantum dots due to interaction with nuclei," *Phys. Rev. Lett.*, vol. 88, p. 186802, 2002.

[57] A. V. Khaetskii and Y. V. Nazarov, "Spin relaxation in semiconductor quantum dots," *Phys. Rev. B*, vol. 61, p. 12639, 2000.

[58] S. Erlingsson, Y. V. Nazarov, and V. I. Fal'ko, "Nucleus-mediated spin-flip transitions in gaas quantum dots," *Phys. Rev. B*, vol. 64, p. 195306, 2001.

[59] S. I. Erlingsson and Y. V. Nazarov, "Hyperfine-mediated transitions between a zeeman split doublet in gaas quantum dots: The role of the internal field," *Phys. Rev. B*, vol. 66, p. 155327, 2002.

[60] H.-P. Breuer and F. Petruccione, *The theory of open quantum systems*. Oxford University Press, 2002.

[61] A. O. Caldeira and A. J. Leggett, "Quantum tunnelling in a dissipative system," *Ann. Phys.*, vol. 149, p. 374, 1983.

[62] J. P. Paz and W. H. Zurek, "Course 8: Environment-induced decoherence and the transition from quantum to classical," in *Coherent Atomic Matter Waves* (R. Kaiser, C. Westbrook, and F. David, eds.), 2001.

[63] U. Weiss, *Quantum Dissipative Systems*. World Scientific Publishing Co. Pte. Ltd, second ed., 1999.

[64] D. Vion, A. Aassime, A. Cottet, P. Joyez, H. Pothier, C. Urbina, D. Esteve, and M. H. Devoret, "Manipulating the quantum state of an electrical circuit," *Science*, vol. 296, p. 886, 2002.

[65] J. M. Martinis, S. Nam, J. Aumentado, and C. Urbina, "Rabi oscillations in a large josephson-junction qubit," *Phys. Rev. Lett.*, vol. 89, p. 117901, 2002.

[66] I. Chiorescu, Y. Nakamura, C. J. P. M. Harmans, and J. E. Mooij, "Coherent quantum dynamics of a superconducting flux qubit," *Science*, vol. 299, p. 1869, 2003.

[67] F. Motzoi, J. M. Gambetta, P. Rebentrost, and F. K. Wilhelm, "Simple pulses for elimination of leakage in weakly nonlinear qubits," *Phys. Rev. Lett.*, vol. 103, p. 110501, 2009.

[68] E. Knill, "Quantum computing with realistically noisy device," *Nature*, vol. 434, p. 44, 2005.

[69] M. Steffen, J. M. Martinis, and I. L. Chuang, "Accurate control of josephson phase qubits," *Phys. Rev. B*, vol. 68, p. 224518, 2003.

[70] P. Rebentrost, I. Serban, T. Schulte-Herbrüggen, and F. K. Wilhelm, "Optimal control of a qubit coupled to a non-markovian environment," *Phys. Rev. Lett.*, vol. 102, p. 090401, 2009.

[71] P. Rebentrost and F. K. Wilhelm, "Optimal control of a leaking qubit," *Phys. Rev. B*, vol. 79, p. 060507, 2009.

[72] G. Lindblad, "On the generators of quantum dynamical semigroups," *Comm. Math. Phys.*, vol. 48, p. 119, 1976.

[73] D. J. Van Harlingen, T. L. Robertson, B. L. T. Plourde, P. A. Reichardt, T. A. Crane, and J. Clarke, "Decoherence in josephson-junction qubits due to critical-current fluctuations," *Phys. Rev. B*, vol. 70, p. 064517, 2004.

[74] J. Claudon, A. Fay, L. P. Lévy, and O. Buisson, "Decoherence processes in a current biased dc squid," *Phys. Rev. B*, vol. 73, p. 180502, 2006.

[75] R. C. Bialczak, R. McDermott, M. Ansmann, M. Hofheinz, N. Katz, E. Lucero, M. Neeley, A. D. O'Connell, H. Wang, A. N. Cleland, and J. M. Martinis, "$1/f$ flux noise in josephson phase qubits," *Phys. Rev. Lett.*, vol. 99, p. 187006, 2007.

[76] J. M. Martinis, "Superconducting phase qubits," *Quantum Inf. Process.*, vol. 8, p. 81, 2009.

[77] J. Lisenfeld, A. Lukashenko, M. Ansmann, J. M. Martinis, and A. V. Ustinov, "Temperature dependence of coherent oscillations in josephson phase qubits," *Phys. Rev. Lett.*, vol. 99, p. 170504, 2007.

[78] M. D. Bowdrey, D. K. L. Oi, A. J. Short, K. Banaszek, and J. A. Jones, "Fidelity of single qubit maps," *Phys. Lett. A*, vol. 294, p. 258, 2002.

[79] J. M. Chow, L. DiCarlo, J. M. Gambetta, F. Motzoi, L. Frunzio, S. M. Girvin, and R. J. Schoelkopf, "Implementing optimal control pulse shaping for improved single-qubit gates," *Phys. Rev. A*, vol. 82, p. 040305, 2010.

[80] D. Walls and G. Milburn, *Quantum Optics*. Springer-Verlang, Berlin, 1994.

[81] P. Kok, W. J. Munro, K. Nemoto, T. C. Ralph, J. P. Dowling, and G. J. Milburn, "Linear optical quantum computing with photonic qubits," *Rev. Mod. Phys.*, vol. 79, p. 135, 2007.

[82] R. H. Hadfield, "Single-photon detectors for optical quantum information applications," *Nature Photonics*, vol. 3, p. 696, 2009.

[83] A. Blais, R.-S. Huang, A. Wallraff, S. M. Girvin, and R. J. Schoelkopf, "Cavity quantum electrodynamics for superconducting electrical circuits: An architecture for quantum computation"," *Phys. Rev. A*, vol. 69, p. 062320, 2004.

[84] A. Wallraff, D. I. Schuster, A. Blais, L. Frunzio, R. S. Huang, J. Majer, S. Kumar, S. M. Girvin, and R. J. Schoelkopf, "Strong coupling of a single photon to a superconducting qubit using circuit quantum electrodynamics," *Nature*, vol. 431, p. 162, 2004.

[85] J. Q. You and F. Nori, "Atomic physics and quantum optics using superconducting circuits," *Nature*, vol. 474, p. 589, 2011.

[86] J. Q. You and F. Nori, "Quantum information processing with superconducting qubits in a microwave field," *Phys. Rev. B*, vol. 68, p. 064509, 2003.

[87] I. Buluta, S. Ashhab, and F. Nori, "Natural and artifical atoms for quantum computation," *Rep. Prog. Phys.*, vol. 74, p. 104401, 2011.

[88] A. A. Houck, D. I. Schuster, J. M. Gambetta, J. A. Schreier, B. R. Johnson, J. M. Chow, L. Frunzio, J. Majer, M. H. Devoret, S. M. Girvin, and R. J. Schoelkopf, "Generating single microwave photons in a circuit," *Nature*, vol. 449, p. 328, 2007.

[89] I. Chiorescu, P. Bertet, K. Semba, Y. Nakamura, C. J. P. M. Harmans, and J. E. Mooij, "Coherent dynamics of a flux qubit coupled to a harmonic oscillator," *Nature*, vol. 431, p. 159, 2004.

[90] G. Romero, J. J. Garcia-Ripoll, and E. Solano, "Microwave photon detector in circuit qed," *Phys. Rev. Lett.*, vol. 102, p. 173602, 2009.

[91] Y.-F. Chen, D. Hover, S. Sendelbach, L. Maurer, S. T. Merkel, E. J. Pritchett, F. K. Wilhelm, and R. McDermott, "Microwave photon counter based on josephson junctions," *Phys. Rev. Lett.*, vol. 107, p. 217401, 2011.

[92] N. Gisin, G. Ribordy, W. Tittel, and H. Zbinden, "Quantum cryptography," *Rev. Mod. Phys.*, vol. 74, p. 145, 2002.

[93] B. Osberg, "Quantum microwave photodetection using superconducting josephson circuits," *University of Waterloo (Msc. Thesis), http://hdl.handle.net/10012/4689,*, 2009.

[94] B. Peropadre, G. Romero, G. Johansson, C. Wilson, E. Solano, and J. J. Garcia-Ripoll, "Approaching perfect microwave photodetection in circuit qed," *Phys. Rev. A*, vol. 84, no. 6, p. 063834, 2011.

[95] J. Q. You, Y.-X. Liu, C. P. Sun, and F. Nori, "Persistent single-photon production by tunable on-chip micromaser with a superconducting quantum circuit," *Phys. Rev. B*, vol. 75, p. 104516, 2007.

[96] M. H. Devoret, J. M. Martinis, D. Esteve, and J. Clarke, "Resonant activation from the zero-voltage state of a current-biased josephson junction," *Phys. Rev. Lett.*, vol. 53, p. 1260, 1984.

[97] E. Jaynes and F. Cummings, "Comparison of quantum and semiclassical radiation theories with application to the beam maser," *Proceedings of the IEEE*, vol. 51, p. 89, 1963.

[98] R. R. Puri and G. S. Agarwal, "Collapse and revival phenomena in the jaynes-cummings model with cavity damping," *Phys. Rev. A*, vol. 33, p. 3610, 1986.

[99] S. Gurvitz and Y. S. Prager, "Microscopic derivation of rate equations for quantum transport," *Phys. Rev. B*, vol. 53, p. 15932, 1996.

[100] S. Gurvitz, "Rate equations for quantum transport in multidot systems," *Phys. Rev. B*, vol. 57, p. 6602, 1998.

[101] J. Ping, X.-Q. Li, and S. Gurvitz, "Quantum coherence and entanglement induced by the continuum between distant localized states," *Phys. Rev. A*, vol. 83, p. 042112, 2011.

[102] J. Ping, Y. Ye, X.-Q. Li, Y. Yan, and S. Gurvitz, "Undetectable quantum transfer through a continuum," *arXiv:1106.2901v2*, 06 2011.

[103] A. A. Clerk, M. H. Devoret, S. M. Girvin, F. Marquardt, and R. J. Schoelkopf, "Introduction to quantum noise, measurement, and amplification," *Rev. Mod. Phys.*, vol. 82, p. 1155, 2010.

[104] J. R. Johansson, G. Johansson, C. M. Wilson, and F. Nori, "Dynamical casimir effect in superconducting microwave circuits," *Phys. Rev. A*, vol. 82, p. 052509, 2010.

[105] T. Brandes, "Waiting times and noise in single particle transport," *Ann. Phys.*, vol. 17, p. 477, 2008.

[106] M. V. Berry, "Quantal phase factors accompanying adiabatic changes," *Proc. R. Soc. Lond. A*, vol. 392, no. 1802, p. 45, 1984.

[107] L.-M. Duan, J. I. Cirac, and P. Zoller, "Geometric manipulation of trapped ions for quantum computation," *Science*, vol. 292, p. 1695, 2001.

[108] J. P. Provost and G. Valle, "Riemannian structure on manifolds of quantum states," *Comm. Math. Phys.*, vol. 76, no. 3, p. 289, 1980.

[109] S. Berger, M. Pechal, J. A. A. Abdumalikov, C. Eichler, L. Steffen, A. Fedorov, A. Wallraff, and S. Filipp, "Geometric phases in superconducting qubits beyond the two-level approximation," *Phys. Rev. B*, vol. 85, p. 220502(R), 2012.

[110] S. Berger, M. Pechal, J. A. A. Abdumalikov, C. Eichler, L. Steffen, A. Fedorov, A. Wallraff, and S. Filipp, "Exploring the effect of noise on geometric phases using superconducting qubits," *arXiv:1302.3305*, 2013.

[111] J. E. Avron, M. Fraas, G. M. Graf, and O. Kenneth, "Quantum response of dephasing open systems," *New J. Phys.*, vol. 13, p. 053042, 2011.

[112] R. S. Whitney, Y. Makhlin, A. Shnirman, and Y. Gefen, "Geometric nature of the environment-induced berry phase and geometric dephasing," *Phys. Rev. Lett.*, vol. 94, p. 070407, 2005.

[113] T. Hayashi, T. Fujisawa, H. D. Cheong, Y. H. Jeong, and Y. Hirayama, "Coherent manipulation of electronic states in a double quantum dot," *Phys. Rev. Lett.*, vol. 91, p. 226804, 2003.

[114] J. Petta, A. C. Johnson, C. M. Marcus, M. P. Hanson, and A. C. Gossard, "Manipulation of a single charge in a double quantum dot," *Phys. Rev. Lett.*, vol. 93, p. 186802, 2004.

[115] J. Gorman, D. G. Hasko, and D. A. Williams, "Charge-qubit operation of an isolated double quantum dot," *Phys. Rev. Lett.*, vol. 95, p. 090502, 2005.

[116] Y. Hu, H. O. H. Churchill, D. J. Reilly, J. Xiang, C. M. Lieber, and C. M. Marcus, "A ge/si heterostructure nanowire-based double quantum dot with integrated charge sensor," *Nature Naotechnology*, vol. 2, p. 622, 2007.

[117] N. Mason, M. J. Biercuk, and C. M. Marcus, "Local gate control of a carbon nanotube double quantum dot," *Science*, vol. 303, p. 655, 2004.

[118] J. Taylor, J. Petta, A. C. Johnson, A. Yacoby, C. M. Marcus, and M. D. Lukin, "Relaxation, dephasing, and quantum control of electron spins in double quantum dots," *Phys. Rev. B*, vol. 76, p. 035315, 2007.

[119] V. N. Stavrou and X. Hu, "Charge decoherence in laterally coupled quantum dots due to electron-phonon interactions," *Phys. Rev. B*, vol. 72, p. 075362, 2005.

[120] M. Thowart, J. Eckel, and E. R. Mucciolo, "Non-markovian dynamics of double quantum dot charge qubits due to acoustic phonons," *Phys. Rev. B*, vol. 72, p. 235320, 2005.

[121] E. M. Lifshitz, "The theory of molecular attractive forces between solids," *Sov. Phys. JETP*, vol. 2, p. 73, 1956.

[122] G. Agarwal, "Quantum electrodynamics in the presence of dielectrics and conductors. iii. relations among one-photon transition probabilities in stationary and nonstationary fields, density of states, the field-correlation functions, and surface-dependent response functions," *Phys. Rev. A*, vol. 11, p. 253, 1975.

[123] S. M. Rytov, *Theory of Electrical Fluctuation and Thermal Radiation.* AN SSSR Press, 1953.

[124] J. B. Pendry, "Radiative exchange of heat between nanostructures," *J. Phys.: Condens. Matter*, vol. 11, p. 6621, 1999.

[125] A. I. Volokitin and B. N. J. Persson, "Near-field radiative heat transfer and noncontact friction," *Rev. Mod. Phys.*, vol. 79, p. 1291, 2007.

[126] K. Joulain, J.-P. Mulet, F. Marquier, R. Carminati, and J.-J. Greffet, "Surface electromagnetic waves thermally excited: Radiative heat transfer, coherence properties and casimir forces revisited in the near field," *Surf. Sci. Rep.*, vol. 57, p. 59, 2005.

[127] C. Henkel, S. Potting, and M. Wilkens, "Loss and heating of particles in small and noisy traps," *Appl. Phys. B*, vol. 69, p. 379, 1999.

[128] D. M. Harber, J. M. McGuirk, J. M. Obrecht, and E. A. Cornell, "Thermally induced losses in ultra-cold atoms magnetically trapped near room-temperature surfaces," *J. Low Temp. Phys.*, vol. 133, p. 229, 2003.

[129] F. Marquardt and V. A. Abalmassov, "Spin relaxation in a quantum dot due to nyquist noise," *Phys. Rev. B*, vol. 71, p. 165325, 2005.

[130] G. Ford and W. Weber, "Electromagnetic interactions of molecules with metal surfaces," *Phys. Rep.*, vol. 113, p. 195, 1984.

[131] C. Henkel and K. Joulain, "Electromagnetic field correlations near a surface with a nonlocal optical response," *Appl. Phys. B*, vol. 84, p. 61, 2006.

[132] H. B. Callen and T. A. Welton, "Irreversibility and generalized noise," *Phys. Rev.*, vol. 83, p. 34, 1951.

[133] E. M. Lifshitz and L. P. Pitaevskii, *Statistical Physics, Part 2*, vol. 9 of *Course in Theoretical Physics.* Pergamon, 1980.

[134] M. Xiao, M. G. House, and H. W. Jiang, "Measurement of the spin relaxation time of single electrons in a silicon metal-oxide-semiconductor-based quantum dot," *Phys. Rev. Lett.*, vol. 104, p. 096801, 2010.

[135] J. M. Elzerman, R. Hanson, L. H. Willems van Beveren, B. Witkamp, L. M. K. Vandersypen, and L. P. Kouwenhoven, "Single-shot read-out of an individual electron spin in a quantum dot," *Nature*, vol. 430, p. 431, 2004.

[136] M. G. Borselli, K. Eng, E. T. Croke, B. M. Maune, B. Huang, R. S. Ross, A. A. Kiselev, P. W. Deelman, I. Alvarado-Rodriguez, A. E. Schmitz, M. Sokolich, K. S. Holabird, T. M. Hazard, M. F. Gyure, and A. T. Hunter, "Pauli spin blockade in undoped si/sige two-electron double quantum dots," *Appl. Phys. Lett.*, vol. 99, p. 063109, 2011.

[137] K. D. Petersson, J. R. Petta, H. Lu, and A. C. Gossard, "Quantum coherence in a one-electron semiconductor charge qubit," *Phys. Rev. Lett.*, vol. 105, p. 246804, 2010.

[138] S. Amasha, K. MacLean, I. P. Radu, D. M. Zumbühl, M. A. Kastner, M. P. Hanson, and A. C. Gossard, "Electrical control of spin relaxation in a quantum dot," *Phys. Rev. Lett.*, vol. 100, p. 046803, 2008.

[139] A. V. Khaetskii and Y. V. Nazarov, "Spin-flip transitions between zeeman sublevels in semiconductor quantum dots," *Phys. Rev. B.*, vol. 64, p. 125316, 2001.

[140] B. D. Josephson, "Possible new effects in superconductive tunnelling," *Phys. Lett.*, vol. 1, p. 251, 1962.

[141] M. Tinkham, *Introduction to Superconductivity.* McGraw-Hill, Inc., 1980.